

General Disclaimer

One or more of the Following Statements may affect this Document

- This document has been reproduced from the best copy furnished by the organizational source. It is being released in the interest of making available as much information as possible.
- This document may contain data, which exceeds the sheet parameters. It was furnished in this condition by the organizational source and is the best copy available.
- This document may contain tone-on-tone or color graphs, charts and/or pictures, which have been reproduced in black and white.
- This document is paginated as submitted by the original source.
- Portions of this document are not fully legible due to the historical nature of some of the material. However, it is the best reproduction available from the original submission.



Technical Memorandum 85101

RAPID X-RAY VARIABILITY OF ACTIVE GALAXIES

Allyn Field Tennant, Jr.

(NASA-TM-85101) RAPID X-RAY VARIABILITY OF
ACTIVE GALAXIES Ph.D. Thesis (NASA) 166 p
HC A08/MF A01 CSCL 03B

N84-11082

Unclas
G3/90 42271

SEPTEMBER 1983

National Aeronautics and
Space Administration

Goddard Space Flight Center
Greenbelt, Maryland 20771



RAPID X-RAY VARIABILITY OF ACTIVE GALAXIES

by

Allyn Field Tennant, Jr.

Dissertation submitted to the Faculty of the Graduate School
of the University of Maryland in partial fulfillment
of the requirements for the degree of
Doctor of Philosophy

1983

APPROVAL SHEET

Title of Thesis: Rapid X-Ray Variability of Active Galaxies

Name of Candidate: Allyn Field Tennant, Jr.

Doctor of Philosophy, 1983

Thesis and Abstract Approved:

Ch. L. Boldt

Elihu A. Boldt

Adjunct Professor

Department of Physics and Astronomy

Date Approved:

August 26 1983

CURRICULUM VITAE

Name: Allyn Field Tennant, Jr.

Permanent address: 15624 Morgan Street, Clearwater, Florida 33520.

Degree and date to be conferred: Ph.D., 1983.

Date of birth: [REDACTED]

Secondary education: Largo High School, Largo, Florida, June 1974.

Collegiate institutions attended	Dates	Degree	Date of Degree
Rollins College	1973-1974		
University of Texas, Austin	1975-1977	B.S.	1977
University of Maryland	1977-1983	Ph.D.	1983

Major: Physics

Professional publications:

"Plankton Analysis and Flow Studies", Allyn Tennant, The Lake Virginia Report: 1974-75, Rollins College, 1976.

"Centaurus A (NGC 5128) at 2 keV-2.3 MeV: HEAO-1 Observations and Implications", W.A. Baity, R.E. Rothschild, R.E. Lingenfelter, W.A. Stein, P.L. Nolan, D.E. Gruber, F.K. Knight, J.L. Matteson, L.E. Peterson, F.A. Primini, A.N. Levine, W.H.G. Lewin, R.F. Mushotzky, and A.F. Tennant, *Ap. J.*, 244, 929, 1981.

"Rapid X-Ray Variability in the Seyfert Galaxy NGC 6814", A.F. Tennant, R.F. Mushotzky, E.A. Boldt, and J.H. Swank, *Ap. J.*, 251, 15, 1981.

"The Absence of Rapid X-Ray Variability in Active Galaxies", A.F. Tennant and R.F. Mushotzky, *Ap. J.*, 264, 92, 1983.

"Synthetic Programming on the HP-15C", Allyn F. Tennant, *PPC Calculator Journal*, 10, 49, 1983.

"Observations of NGC 4151 at 2 keV-2 MeV from HEAO-1", W.A. Baity, R.F. Mushotzky, D.M. Worrall, R.E. Rothschild, A.F. Tennant, and F.A. Primini, submitted to *Ap. J.*

Professional positions held:

1977-1978 Teaching Assistant, University of Maryland, College Park, MD 20742.

1978-1983 Research Assistant, Code 661, NASA/Goddard Space Flight Center, Greenbelt, MD 20771.

1983 Research Associate, Institute of Astronomy, Madingley Road, Cambridge CB3 0HA ENGLAND.

ABSTRACT

Title of Dissertation: Rapid X-Ray Variability of Active Galaxies

Allyn F. Tennant, Doctor of Philosophy, 1983

Dissertation directed by: Elihu A. Boldt

Adjunct Professor

Department of Physics

Active galactic nuclei are luminous sources of X-rays. It has generally been assumed that the X-rays are generated within 10 gravitational radii from the central object. Research in this thesis tests this idea by making a very sensitive search for rapid (< 1 day) X-ray variability from active galaxies.

To perform this search one has to develop statistical techniques to separate true source variability from noise. Methods, tested with Monte Carlo simulations of the data, are presented which allow this separation when the data bins have unequal length and which determine the time scale of source variability given an observed source variance.

The in orbit performance of the detector is quite good. A small signal caused by particle contamination is greatly reduced if one only uses data taken at low values of McIlwain L. A study of about 50 observations of 'blank sky' shows another signal at a level of 1% of the total background. This signal is due to different parts of the X-ray background

being sampled due to spacecraft jitter and so measures the spatial variance of the sky. A 'serendipitous' burst, discovered during a blank sky observation, appears to be a flare from a nearby galactic source.

Observations of 38 different active galaxies show no evidence for rapid variability for the vast majority of the objects. Three objects which do vary show a time scale consistent with one day. Only the observation of NGC 6814 shows a time scale shorter than one day, and this object shows factor-of-two changes for periods as short as 2 minutes.

The non-variability of most objects indicates that the X-ray producing plasma is either stable or large. A nonthermal relativistic electron population would explain the X-ray spectra. Since these electrons cannot be gravitationally bound, the X-ray plasma will fill a large volume relative to the size of central object. Occasional flares are produced when a new burst of particles is injected into the surrounding cloud. In this picture NGC 6814 would be dominated by the variable emission from the injection mechanism instead of the more constant emission from the surrounding cloud.

Acknowledgments

First, I would like to thank those people who were graduate students with me. Julie Saba, Rick Shafer, Andy Szymkowiak, Meg Urry and more recently Alanna Connors all helped to make the graduate student life interesting and entertaining. I especially enjoyed many useful discussions with Andy concerning cars, computers and astrophysics.

The CSC office starring Deborah Derrick and Marilyn Newhouse often provided moral support.

My advisors Elihu Boldt, Richard Mushotzky, and Jean Swank all contributed greatly to my knowledge of astrophysics. All three read my dissertation and offered suggestions for (often needed) improvements.

Thanks to Sandy Shrader who had the job of translating my handwriting into typed pages.

Many of the above mentioned people were offered an opportunity to proofread a chapter and accepted. Gail Reichert proofread several chapters and often suggested improvements in wording.

Finally, it has been my pleasure to interact with numerous people from Goddard and the University of Maryland, and with visiting scientists from the world over.

TABLE OF CONTENTS

Chapter	Page
Acknowledgments.	<i>ii</i>
List of Tables	<i>vi</i>
List of Figures.	<i>vii</i>
1. INTRODUCTION	1
1.1 Chapter Overview	1
1.2 Properties of Active Galaxies.	1
1.3 The Standard Model	4
1.4 Timing	5
1.5 Other Observations of Rapid X-Ray Variability.	6
1.6 Variability At Other Wavelengths	8
1.7 Outline of Research Presented.	9
2. SEPARATING THE SIGNAL FROM THE NOISE	10
2.1 Chapter Overview	11
2.2 Comment on Weighted Quantities	11
2.3 Separating Source Variance From Photon Noise	12
2.4 Calculation Of Upper Limits.	15
2.5 Sensitivity.	16
2.6 Autoregressive Process	18
2.7 Moments.	20
2.8 Numerical Results.	25

- 3. DETERMINATION OF TIME SCALES 28
 - 3.1 Chapter Overview 28
 - 3.2 Short Observations 28
 - 3.3 Medium Length Observations 29
 - 3.4 Long Observations: The auto-correlation Function. 29
 - 3.5 Long Observations: Variance vs. Bin Size. 32
 - 3.6 Examples of Variance vs. Bin Size. 35

- 4. IN FLIGHT PERFORMANCE. 40
 - 4.1 Chapter Overview 40
 - 4.2 The Instrument 40
 - 4.3 Particle Discrimination. 42
 - 4.4 Detector Offsets 46
 - 4.5 Pointed Aspect Errors. 47
 - 4.6 Blank Sky Analysis 47

- 5. OBSERVATIONS OF ACTIVE GALAXIES. 62
 - 5.1 Chapter Overview 62
 - 5.2 Variance 62
 - 5.3 Light Curves 66
 - 5.4 Implications of Rapid Non-Variability. 70

- 6. RAPID VARIABILITY OF NGC 6814. 81
 - 6.1 Chapter Overview 81
 - 6.2 Variability on Long Time Scales. 81
 - 6.3 Short Time Scales. 82
 - 6.4 Limits On Spectral Variability 83

6.4.1	Orbit-by-Orbit Variability.	83
6.4.2	Limits on Spectral-Intensity Correlation.	86
6.4.3	Spectral Cross-Correlations	86
6.5	Implications of Rapid Variability.	87
6.5.1	General Considerations.	87
6.5.2	Synchrotron Radiation and Synchrotron Self-Compton Emission.	89
6.5.3	Thermal Bremsstrahlung and Blackbody Radiation.	90
6.5.4	Thermal-Compton Models.	90
6.6	Source Lifetime.	95
7.	RECONCILIATION	105
7.1	Chapter Overview	105
7.2	Comparison With Other Observations of Variability.	105
7.3	Observations At Other Wavelengths.	106
7.3.1	Stability Related to the Eddington Limit.	110
7.3.2	Increased Number of Shots	110
7.3.3	Growth Of New Source Of Soft Photons.	111
7.4.1	Large Source Size	113
7.4.2	Two Components.	114
Appendix A	117
Appendix B	120
Appendix C	127
Appendix D	136
Appendix E	145
Appendix F	148
REFERENCES	150

LIST OF TABLES

2.1	Magnitude of Change for 50% Detection	18
2.2	Moments of Various Distributions.	24
2.3	Moments of Various Distributions (Experimental)	27
3.1	Autocorrelation Function of First Order Autoregressive Process. .	32
4.1	Slope of Best Fit Line.	43
4.2	χ^2 /DOF for Various Models	44
4.3	Total Detector Background Counting Rate	51
5.1	Observations of Active Galaxies	63
6.1	NGC 6814 Orbital Rates.	82
6.2	Auto-correlation Function Results	83
6.3	NGC 6814 Spectral Fits.	84
6.4	NGC 6814 Spectral Fits with Fixed Absorption.	85

LIST OF FIGURES

3.1	Sigma vs. Bin Size (Theory)	38
3.2	Sigma vs. Bin Size (Experimental)	39
4.1	Cross Sectional View of Detector.	54
4.2	Detector Grid Connections	55
4.3	HED3 Total Rate vs. Anticoincidence	56
4.4	Anticoincidence vs. McIlwain L.	57
4.5	HED3 Total Rate vs. McIlwain L.	58
4.6	Histogram of Number of Major Frames with a Given Value of L	59
4.7	Single Scan Over Crab	60
4.8	Sigma During Blank sky Observations	61
5.1	Standard Deviation of Source Intensity vs. Flux for 328 Sec Bin Size	75
5.2	Standard Deviation of Source Intensity vs. Flux for 86 Minute Bin Size	76
5.3	Histograms of Variability	77
5.4	X-Ray Light Curves of Nine Active Galactic Nuclei Observed by HEAO-1	78
5.5	Fits to NGC 4151 Light Curve.	79
5.6	X-Ray Map of Region Around H1649-595.	80
6.1	NGC 6814 Light Curve.	90
6.2	Segment of NGC 6814 Light Curve	100
6.3	Segment of NGC 6814 Light Curve	101

6.4	Auto-correlation Function for NGC 6814.	102
6.5	Power Law Index vs. Flux (Orbital Averages)	103
6.6	Average "Hard" Flux for a Specified "Soft" Flux	104
B.1	The Mapping of (R, λ) onto the (L, B) Plane	124
B.2	Particle flux on the (L, B) Plane.	125
B.3	HEAO-1's Location on the (L, B) Plane.	126
C.1	Rate vs. Time for Small Solar Flare	131
C.2	Rate vs. Time for Large Solar Flare	132
C.3	Rate vs. Time for X-Ray Flare	133
C.4	Rate vs. Time for Electron Contamination on Day 526	134
C.5	Rate vs. Time for Electron Contamination on Day 550	135
D.1	Soft Flux and Hard Flux During Observation of ESO 141-G55	141
D.2	Rate in the Second Layer of the MED	142
D.3	Background Rate during Observation of ESO 141-G55	143
D.4	Rate Includes Data for all Values of McIlwain L	144

1. INTRODUCTION

1.1 Chapter Overview

In this chapter I provide a general introduction to the properties of active galactic nuclei. I begin with a general description of the important observed properties for the non-expert. Optical observations indicate a strong source of ionizing photons ($h\nu \gtrsim 13.6$ eV). It is quite likely that the observed X-rays are related to this ionizing source. The X-rays are generally assumed to be produced very near to the "central black hole". This idea is based more on belief than on fact and so needs to be tested. The research presented in this thesis makes such a test by performing a very sensitive search for rapid (< 1 day) variability. Observations of rapid variability could indicate a compact source of X-rays whereas the lack of variability could indicate extended emission. The chapter ends with a discussion of other observations of rapid variability both in the X-ray band and at other wavelengths.

1.2 Properties of Active Galaxies

Seyfert (1943) pointed out that although many galactic nuclei contain emission lines, there is a small class of objects which show strong Balmer lines in addition to lines from highly excited states. Over the years galaxies showing such lines have come to be called Seyfert galaxies. The strongest optical lines are from the Balmer series, twice ionized oxygen [OIII] at 5007 Å and once ionized nitrogen [NII] at 6583 Å. A wide range of ionization is observed ranging from [OI], [NI] and [SII] to [Ne V], [Fe VII] and [Fe X] (Osterbrock 1981). These forbidden lines typically have widths (FWHM) ranging from 500 km/sec to 1000 km/sec (Khachikian and Weedman 1974). These lines are called the narrow lines

since they are often quite narrow when compared to the hydrogen recombination lines.

The Balmer lines are very strong and can have widths ranging up to 5000 km/sec. In 1971 Khachikian and Weedman proposed dividing Seyfert galaxies into two classes based on the widths of the permitted lines. In Seyfert 2 galaxies the permitted lines have roughly the same width as the forbidden lines. In Seyfert 1's the permitted lines have widths ranging from 1000 km/sec to 5000 km/sec.

Seyfert galaxies also have very bright nuclei. As Weedman pointed out in his 1977 review of Seyfert galaxies, galaxies with strong broad emission lines always have bright nuclei. Some galaxies with bright nuclei do not show Seyfert characteristics. However, Weedman points out that if the nucleus is bright relative to the disk, then it is very likely to be a Seyfert. There is a wide range of nuclear luminosities. Yee (1980) published the non-thermal luminosities of a large number of active galaxies. Although a large part of his non-thermal emission could be due to lines, it does represent a good estimate for the luminosity of the nucleus. These luminosities ranged from 3×10^{41} ergs/sec up to 3×10^{43} ergs/sec for the Seyfert 2's. For Seyfert 1 galaxies the range was 3×10^{41} to 3×10^{44} erg/sec. The sun emits 2×10^{33} ergs/sec (integrated) and the luminosity of a bright galaxy equals 10^{11} suns. Therefore, a large fraction of the total light emitted by an active galaxy can come from the nucleus.

Radio astronomers discovered that some galaxies can be strong sources of radio emission. Radio emission from galaxies generally comes from three components, with two components forming large lobes on opposite sides of the galaxy. These lobes can be quite large and are bright at low

frequencies (MHz). For Cen A, a bright nearby radio galaxy, the radio lobes are about 1 Mpc in length and the radio spectrum is a power law with an index that ranges from 0.9 to 0.6 over a frequency range of 19.3 Mz to 500 Mz (Cooper, Price and Cole, 1965). The nucleus of a radio galaxy is also observed to emit radio waves at high frequencies. For this work we will only be concerned with the nucleus. However, observations made at the Very Large Array (VLA) have shown that in a radio galaxy the nucleus is often connected with the external lobes via jet-like structures. This provides clear evidence that the nucleus also powers the lobes.

Optical spectra of the nuclei of radio galaxies show that they come in two types: those with broad lines and those with narrow lines. Thus the spectra of radio galaxies greatly resemble the spectra of Seyfert galaxies, although in a statistical sense it is possible to distinguish between the two classes (Osterbrock, 1978). The properties of the associated galaxies are quite different. Radio galaxies almost always occur in elliptical galaxies whereas Seyfert galaxies tend to be spirals. Wilson et al. (1980) and Wilson and Willis (1980) observed that some Seyfert galaxies do contain very small radio lobes. Wilson and Willis argued that the galaxies containing lots of gas and dust (i.e. spirals) do not produce giant radio lobes since the gas and dust blocks the energetic particles from reaching intergalactic space.

By the early 1960's radio astronomers had discovered a large number of radio galaxies. Some radio sources did not appear to be associated with galaxies but rather with star-like objects having rather unusual optical spectra. In 1963 Schmidt identified the lines in the spectra of 3C 273 as being typical lines from an active nucleus but at a redshift $z = \Delta\lambda/\lambda \approx .16$. Shortly thereafter Greenstein and Matthews (1963) identified

the redshift of 3C 48 to be at a $z \approx .37$. In an expanding universe redshifts correspond to distance and so quasars are generally assumed to be very distant active galaxies. Over the years many quasars have been discovered and a couple have been found with $z > 3.5$. In the 1960's it was discovered that quasars can be either radio loud or radio quiet. The recombination lines observed in quasar spectra can be either broad or narrow in the same way that Seyfert spectra can have either broad or narrow lines.

1.3 The Standard Model

It is useful to have in mind the general picture or model of an active nucleus, as this allows greater understanding as to where various observations fit into the total picture. It is typical to divide the nuclear region into three parts:

1. There is a "point source" at the center which is the power source for the nucleus. This source, sometimes called the central engine, radiates large quantities of ionizing radiation. It is generally assumed that the ultimate source of power is gravitational energy release.

2. Surrounding the central engine and extending out to several light days for the low luminosity objects and several light years for the high luminosity objects, is the broad line region. This region consists of dense ($10^9 - 10^{10} \text{ cm}^{-3}$) fast moving clouds at a temperature of $\sim 10^4 \text{ K}$. Photoionization of these clouds produces the broad lines and collisional deexcitation suppresses emission from the forbidden lines.

3. External to the broad line region is the narrow line region which can extend to a radius of several thousand light years. The clouds in this region are less dense ($10^2 - 10^6 \text{ cm}^{-3}$) and so can reradiate forbidden lines when photoionized.

Thus in the standard picture all active nuclei are very similar. Narrow line objects are merely active galaxies without broad line clouds. Quasars are distant and hence luminous forms of active galaxies. Radio galaxies are active galaxies that allow the relativistic particles to escape. And finally, BL Lacs may be radio galaxies in which the escaping particles are coming roughly directly towards the Earth.

1.4 Timing

In the standard model the lines are produced as a secondary source of radiation. Although emission lines provide a very good diagnostic of the environment in which they are produced, this environment turns out to be the broad and narrow line regions. Hence, the lines tell us relatively little about the central engine. In order to study the source of the power one needs to consider the continuum.

In the standard picture it is popular to assume that X-rays are produced deep in the potential well near a supermassive object (see Rees, Begelman and Blandford 1981 for a recent discussion). If the X-ray flux from this dense, gravitationally confined plasma is observed to vary, then the shortest time scale will be on the order of the light travel time across the innermost stable orbit in a Schwarzschild geometry. This is given by

$$\Delta\tau \sim R/c \sim 6 GM/c^3 \sim 50 M_6 \text{ sec}$$

where M_6 is the mass of the central object in terms of 10^6 solar masses ($M_0 = 1$ solar mass = 2×10^{33} gm). Since these objects are not expected to exceed the Eddington limit, we expect M_6 to lie in the range of .1 to 1000 for luminosities ranging from 10^{43} to 10^{47} erg/sec. Thus the relevant time

scales range from ~ 10 sec to $\sim 1/2$ day. Lack of variability on these time scales could be an indication that the X-ray emitting plasma is not gravitationally contained.

Fabian and Rees (1979) (see also Cavallo and Rees 1978) have proposed a general constraint on the shortest time scale for a given change in luminosity. They assumed that a spherically symmetric, homogeneous cloud of stationary matter is converted into radiation with an efficiency of η . The shortest observed time for the change to take place is given when the optical depth of the cloud is unity. This gives the minimum time $\Delta\tau_{\min} \sim 5 L_{43}/\eta$ sec where L_{43} is the luminosity in units of 10^{43} ergs/sec.

1.5 Other Observations of Rapid X-Ray Variability

An early report of variability on a short time scale was made by Winkler and White (1975). They reported that the X-ray flux of Cen A increased by a factor 1.6 over a 6 day observation, which is considered to be a mild change by "modern" standards.

Delvaillle, Epstein and Schnopper (1978) found evidence for a 25% step increase in flux from Cen A. They reported a 2 sigma uncertainty in the length of the step of 0 to 5 hours. Their observed count rate was quite low and so the error for a single time bin was about 25%. This result could have been affected by systematics such as nearby sources (see Marshall and Clark 1981). However, Lawrence, Pye and Elvis (1977) have shown that Cen A is continuously variable over extended periods of time with a time scale of about 1 day.

The second brightest active galaxy, NGC 4151, also has a long history of X-ray variability. Elvis (1976) reported that NGC 4151 flared by a factor of 1.7 in less than 3 days. Tananbaum et al. (1978) reported a

factor of 10 change on a time scale as short as 730 sec. I discuss this observation in Appendix F and point out that the 700 sec result is probably in error. Mushotzky, Holt and Serlemitsos (1978) reported a flare with a factor of two change observed over 1.5 days. Lawrence (1980) finds such flare-like events are rather common in Ariel 5 data extending over several years. Although some of the observed flux variations on longer time scales are caused by variations in the absorption column (Barr et al. 1977), there are no indications of changes in the absorption or spectral index during the more rapid changes (Mushotzky, Holt and Serlemitsos 1978; Baity et al. 1983).

There have been a few observations of rapid variability made with the Einstein Observatory. Tananbaum (1980) reported strong evidence for variability from NGC 6814 on a time scale of 6 hours with an indication of activity at shorter time scales. In the same article, Tananbaum reported a flux increase from 3C 273. The flux of 3C 273 increased by 10% between two observations separated by ~ 12 hours. Tananbaum (1980) suggests that the change could have taken place in ~ 6000 sec on the basis of a single unpublished data point.

Tananbaum et al. (1979) reported that the luminosity of the quasar OX 169 varied by 1.5×10^{44} erg/sec. The reported time scale of 6000 sec is based on the difference between two data bins with rather large uncertainties. If one includes this statistical error then one finds that the observed change in $\Delta L/\Delta t$ could be smaller by a factor of two.

Matilsky, Schrader and Tananbaum (1982) have reported evidence for 200 sec variability from the quasar 1525+227. Their published light curve consists of 8 data bins (200 sec each) of which 2 bins, near the end of the observation, are high. Also published were the arrival times of all 107

photons collected.

1.6 Variability At Other Wavelengths

The most spectacular observation of rapid variability has been reported by Wolstencroft et al. (1982). They observed the BL Lac OJ 287 at a wavelength of $1.25 \mu\text{m}$. Their published light curve shows that the flux can vary by a factor 2.0 on a time scale as short as a minute. At a z of .306, and assuming $H_0 = 100 \text{ km/sec/Mpc}$, the change in the luminosity (in the observed band only!) is 10^{44} ergs/sec . As Wolstencroft et al. point out, such a rapid change in ΔL implies relativistic beaming. Beaming helps in several ways; photons (in the Earth's frame) have higher energies, timescales appear shorter, and the flux is not radiated uniformly over 4π steradians. The combination of these effects could bring the value of $\Delta L/\Delta t$ down to the theoretical maximum (Fabian and Rees 1979). Wolstencroft et al. saw rapid variability in only one observation (out of 12) of OJ 287. In addition, they have observed other QSO's and BL lacs for many tens of hours, without seeing such changes. Thus rapid variability is very rare.

In the radio part of the spectrum, Kikuchi et al. (1973) reported a 20% decrease in the 7.2 cm radio flux during an observation of OJ 287 which lasted 100 min. There was only a very small increase in the flux of 3C 147, which was observed before and after OJ 287 and served as a calibration source. Efanov et al. (1977) reported a 20% change over 4 hours in the 22 GHz flux from 3C 273. The change over 24 hours amounted to 33%. Coe et al. (1983) searched nine active galaxies for 10.7 GHz variability. They considered time scales ranging from 25 min to a few days. They reported no strong evidence for variability on a time scale of less than 1 day but did see weak evidence for day-to-day changes in the

flux from 3C 273 and QSO 0241+62.

Lawrence et al. (1981) observed NGC 4151 at optical wavelengths for several hours per night for a week. They reported that the nightly means were constant to 0.2 mag (2%) over the entire week. Lyutyi (1977) reported that NGC 4151 continuously shows flares with a rise time of 2-10 days and a decay time of 20-50 days. Thus Lawrence et al. seem to have observed NGC 4151 during a quiet period. On shorter time scales Lawrence et al. reported a single .15 mag (15%) dip lasting ~ 2 hours. Since the colors did not change during this time, they conclude that a high thin cloud could have caused the dip. With this exception they conclude that they did not observe any significant variability on time scales ranging from 10 sec to several days.

1.7 Outline of Research Presented

The main research presented in this thesis is a very sensitive search for rapid X-ray variability. In order to make this search, one must be able to extract source variability from X-ray data. Chapter 2 describes a method that works when the data bins have unequal lengths. Given an observation of variability one then attempts to measure some sort of time scale. Methods to do so are presented in Chapter 3. These methods have been tested with numerical simulations. The final preliminary step is to evaluate the performance of the detector. This is done in Chapter 4 where the amount of residual noise from various sources is estimated.

Chapters 5, 6 and 7 form the bulk of the astrophysical results presented. In Chapter 5 it is shown that the majority of active galactic nuclei studied do not vary on time scales of less than 1 day. The test was sensitive enough so that in an observation lasting < 12 hours, variability with a time scale of a day or more could be detected. The exception to the

above was NGC 6814 which showed factor of two changes on time scales as short as 100 sec, but with no detectable spectral changes. Chapter 7 attempts to reconcile the rapid variability of NGC 6814 with the general lack of variability observed from other objects.

2. SEPARATING THE SIGNAL FROM THE NOISE

2.1 Chapter Overview

In this chapter I will describe a general method to separate true source variability from photon counting noise. The method works for the case where the data bins have unequal lengths. It is also possible to derive an upper limit for variability if the count rate is consistent with a constant. Next, I consider some simple models for variability and show the sensitivity of the method. It is always possible to obtain a more sensitive upper limit if one has some a priori knowledge of the shape of the light curve. Various distributions and their moments are described. In the final section the method was tested with numerical simulations.

2.2 Comment on Weighted Quantities

For X-ray astronomy a dominant source of noise is due to Poisson counting statistics. If the true mean counting rate is R and one integrates over a time interval of $\Delta\tau$, then counting statistics will introduce an uncertainty $\sigma_p = (R\Delta\tau)^{1/2}$ in the total number of photons collected. Since the total number of photons $C = R\Delta\tau$ increases linearly with time the percentage uncertainty in the rate decreases as $\Delta\tau$ increases. One does not know the true rate R and so is forced to estimate this number from the data.

If the rate is a slowly varying function of time then one can estimate the true rate at a given time by summing over a large number of bins N . Thus

$$\langle R \rangle = \frac{1}{N\Delta\tau} \sum_{i=1}^N C_i = \frac{C_{\text{tot}}}{N\Delta\tau}$$

where C_i is the observed number of counts in bin i and $C_{\text{tot}} = \sum_i C_i$, is the total number of counts observed. Since $\Delta\tau = 1/N$ we find that the average is independent of the number of bins into which the data was divided.

When one considers weighting the data more care is needed. If, for every observation of C_i , there exists an instrumental error σ_i , then a maximum likelihood analysis (see Bevington 1979, p. 69) shows that the best estimate for the mean is given by

$$\langle R \rangle_w = \sum_i W_i C_i / \sum_i W_i$$

where $\langle \rangle_w$ will denote a weighted average and $W_i = 1/\sigma_i^2$. One is tempted to base the weight for an individual bin on the observed number of counts in that bin. In Appendix A, I show that for small constant mean rate this will generate an incorrect result for the average (no matter how many bins are considered). This is due to the fact that for small C_i , the square root of C_i is a relatively poor estimator for the true uncertainty. Therefore when one weights data it is better to base the weights on the expected number of counts rather than the observed number. If C_i is large then percentage difference between the expected and observed count rates is small. However, in section 4.6, I give an example where the difference is noticeable for $C_i \approx 100$.

2.3 Separating Source Variance From Photon Noise

The simplest way to detect source variability is to calculate χ^2 assuming that the source flux is constant. The size of χ^2 itself provides a useful measure of the source variance (see, for example, Boldt et al. 1975). Also, χ^2 tables provide an estimate of how likely the variance in the observed signal is due to chance alone. The

disadvantage of χ^2 is that it measures the amplitude of source variance relative to photon noise. Thus different experiments with different effective areas will give different values of χ^2 for the same signal. In this section I show how one can separate the source variance from photon noise.

If we assume that the source flux F is constant but that the exposure E_i (effective area integrated over time) can vary from bin to bin then χ^2 is given by

$$\begin{aligned}\chi^2 &= \sum_i \frac{(C_i - \langle C \rangle_i)^2}{\langle C \rangle_i} \\ &= \sum_i \frac{E_i}{\langle F \rangle} (F_i - \langle F \rangle)^2\end{aligned}\quad (2.3.1)$$

where $\langle C \rangle_i = \langle F \rangle E_i$ is the expected number of counts for bin i and C_i is the observed number. Since χ^2 is effectively the weighted variance, it is correct to divide by the expected number of counts for that bin as was argued in the last section. Since $E_i/\langle F \rangle$ is effectively the weight, we find that longer exposures get more weight.

Since χ^2 is related to the weighted variance with

$$\chi_v^2 = \langle W \rangle \langle \sigma^2 \rangle_w \quad (2.3.2)$$

where χ_v^2 is reduced χ^2 , $\langle W \rangle = \frac{1}{N-1} \sum W_i$ and W_i is the weight given to bin i . The total variance is the sum of photon noise σ_p^2 and any excess variance σ_e^2 . If we solve for the excess variance we find

$$\begin{aligned} \langle \sigma_e^2 \rangle_H &= X_V^2 / \langle W \rangle - \langle \sigma_p^2 \rangle_W \\ &= \langle \sigma_p^2 \rangle_W [X_V^2 / (\langle W \rangle \langle \sigma_p^2 \rangle_W) - 1] \end{aligned} \quad (2.3.3)$$

If there is no excess variance, we know $\langle X_V^2 \rangle = 1$. Thus for consistency we require

$$\langle \sigma_p^2 \rangle = \frac{1}{\langle W \rangle} \quad (2.3.4)$$

Since neither $\langle W \rangle$ nor $\langle \sigma_p^2 \rangle$ is a function of σ_e^2 we find that in general,

$$\langle \sigma_e^2 \rangle_W = \frac{X_V^2 - 1}{\langle W \rangle} \quad (2.3.5)$$

The final result will be the error in the background subtracted source flux (F_S). Let E be the total exposure (effective area integrated over time) then

$$F_S = \frac{C - C_B}{E} \quad (2.3.6)$$

where C is the total count rate and C_B the background rate. The statistical uncertainty in F_S is given by

$$\text{var}(F_S) = \frac{C}{E^2} \quad (2.3.7)$$

where I have assumed that C_B is a known quantity. Now $E = \epsilon A_{\text{tot}} \Delta \tau$ where A_{tot} is the total area and ϵ is the efficiency ($\epsilon = 1$ if source is on axis). Thus

$$\begin{aligned} \text{var}(F_S) &= \frac{E F_S + A_{\text{tot}} \Delta \tau F_B}{E^2} = \frac{E F_S + E F_B / \epsilon}{E^2} \\ &= \frac{F_S + F_B / \epsilon}{E} \end{aligned} \quad (2.3.8)$$

where the background flux F_B is not a function of ϵ .

For the observations reported in this thesis the count rate is dominated by a background which will be shown to be quite constant. For the smallest bin size used, 5.12 sec, the minimum number of counts per bin is ~ 56 . For this large number of counts we expect that the error made by setting $\sigma_i^2 = C_i$ (instead of $\langle C \rangle$) to be small. However, for the blank sky analysis (section 4.6) where I added together ~ 50000 , 5.12 sec rates I find that using C_i introduces an unacceptable error if $\langle C \rangle \lesssim 120$. If $\langle C \rangle$ exceeds 120 then it makes little difference which expression one uses for σ_i^2 even for the large number of bins considered.

2.4 Calculation Of Upper Limits

If reduced χ^2 is less than or close to 1.0 then statistical fluctuations will dominate any true source variability. For this case equation (2.3.5) breaks down, and it is better to consider an upper limit. I will base my upper limits at 90% confidence level. Thus, a 90% limit means that, if there were no source variability, then χ^2 would exceed the given value 10% of the time due to chance alone.

For a large number of degrees of freedom ν we find that the probability of exceeding a given value of χ^2 is approximately $P(X)$ where

$$X = \frac{\chi^2 - \nu}{\sqrt{2\nu}}$$

(Equation 26.4.11 of Abramowitz and Stegun, 1970) and $P(X)$ is given by

Table 26.1 of Abramowitz and Stegun. For large ν , a value of $X = 1.3$ gives a 90% confidence level. What is surprising is that this value provides a good estimate of the 90% confidence level for all ν . In fact $X=1.3$ corresponds to 9.2% for $\nu=1$, 10.0 for $\nu=2$, 10.5% for $\nu=10$ and then drops back down to 10.0% by $\nu=200$.

Since the equation for X is so easy and accurate I have used it all the time, even in computer programs where one could easily consider higher order corrections. Therefore, a 90% confidence upper limit is obtained by setting $X = 1.3$, solving for χ^2 and then using this value of χ^2 to obtain the excess variance. Thus the observed value of χ^2 is not used to calculate upper limits.

2.5 Sensitivity

It is important that one understand what the upper limits actually mean. Therefore, in this section I consider several possible models for variability and work out what minimum amplitude signal would, on the average, be detectable at the 90% confidence level. I point out that, if a source population did vary with this minimum signal, then the observed variability would exceed the upper limit 50% of the time and for the remaining observations only upper limits would be reported. This is because, on the average, the observed excess variance will be above the true excess roughly half the time.

Consider an observation which lasted for N bins. Further assume that $N-n$ bins were at one level y_L and the remaining n bins were higher by an additional amount 2Δ . Thus the variance due to this step function type change is given by

$$\sigma_e^2 = \frac{1}{N-1} \{n(y_L - \mu)^2 + (N-n)(y_L + 2\Delta - \mu)^2\} \quad (2.5.1)$$

It is easy to show that $\mu = y_L + \frac{2n\Delta}{N}$. Using this expression gives

$$\sigma_e^2 = \frac{4\Delta^2}{N-1} \frac{(N-n)n}{N} \quad (2.5.2)$$

Now we use $\sigma_e^2 = 1.3 \sigma_p^2 \sqrt{2/\sqrt{N-1}}$ and solve for

$$2\Delta/\sigma_p = 1.34 \left[\frac{N}{n(N-n)} \right]^{1/2} (N-1)^{1/4} \quad (2.5.3)$$

where $2\Delta/\sigma_p$ represents the total change measured in terms of the uncertainty for a single bin.

For $n = 1$ we have the case of a single flare in the observation.

For this case (2.5.3) reduces to

$$2\Delta/\sigma_p \cong 1.36 N^{1/4} \quad (2.5.4)$$

which shows that as one considers more bins, the minimum detectable flare size, $2\Delta/\sigma_p$, increases. This makes sense since the probability of seeing a given σ fluctuation is much higher as one considers more data. In Table 2.1, I evaluated (2.5.4) for certain values of N . For 1000 bins a 7.6σ fluctuation is needed to give an unacceptable χ^2 for the entire data stream. A 7.6σ bin contributes 58 to χ^2 and so our reasoning says that 50% of the time one can hide a $\Delta\chi^2$ of 58 in the remaining 999 bins. It is unlikely that a 7.6σ fluctuation is due to chance alone if one has only 1000 bins. It is important to realize that this method will not provide the smallest upper limits, if one is interested in single bin flares.

Table 2.1
Magnitude of Change for 50% Detection

<u>One Bin High</u>			<u>Half The Bins High</u>		
N	n	$2\Delta/\sigma_p$	N	n	$2\Delta/\sigma_p$
10	1	2.4	10	5	1.52
100	1	4.3	100	50	.86
1000	1	7.6	1000	500	.48

Also in Table 2.1 I have listed the sensitivity for the case where half the data is at $\mu-\Delta$ and the other half at $\mu+\Delta$. We can see that as one considers more bins, one is more sensitive to such a change. Although there is no reason to do so one can assume that the first half is at one value and the second half at the other. For the 1000 bin case, a $.47 \sigma_p$ fluctuation would be detected $\sim 50\%$ of the time. However a step function model would be expected to drop χ^2 by 58 which would be very significant. In general, if one considers a specific model, then one can obtain limits more sensitive than the value obtained in Section 2.4.

2.6 Autoregressive Process

The autoregressive process is a simple method used to generate data with properties similar to observed data streams. Since it is simple, one can quickly determine the parameters and then proceed to generate a lot of phantom data which looks similar to observed data. This allows one to estimate the uncertainties in the derived parameters.

The n^{th} order autoregressive process (see Jenkins and Watts 1968) is

defined for a discrete set of points Y_j by

$$Y_j = \sum_{j=1}^N \alpha_j Y_{j-j} + Z_j \quad (2.6.1)$$

where α_j are the parameters and Z_j is a random variable. Scargle (1981) has written an excellent introduction to time series analysis. He shows the relationships between an autoregressive process and others, such as a moving average model and a shot noise model.

Consider the first order process

$$Y_j = \alpha Y_{j-1} + Z_j \quad (2.6.2)$$

To determine the average value for Y consider

$$\langle Y_j \rangle = \alpha \langle Y_{j-1} \rangle + \langle Z_j \rangle \quad (2.6.3)$$

Now if we assume the process is stationary, then $\langle Y_j \rangle = \langle Y_{j-1} \rangle \equiv \langle Y \rangle$. If we define $\langle Z \rangle = \langle Z_j \rangle$, we then find

$$\langle Y \rangle = \frac{\langle Z \rangle}{1-\alpha} \quad (2.6.4)$$

To determine the variance of Y one has to consider

$$\begin{aligned} \langle Y_j Y_j \rangle &= \langle (\alpha Y_{j-1} + Z_j)(\alpha Y_{j-1} + Z_j) \rangle \\ \langle Y^2 \rangle &= \alpha^2 \langle Y^2 \rangle + 2\alpha \langle YZ \rangle + \langle Z^2 \rangle \end{aligned} \quad (2.6.5)$$

Since Z_i and Y_{i-1} are uncorrelated, $\langle YZ \rangle = \langle Y \rangle \langle Z \rangle$. It is possible to substitute (2.6.4) into (2.6.5). When one solves for the variance $\langle (Y - \langle Y \rangle)^2 \rangle$ one obtains

$$\text{var}(Y) = \frac{\text{var}(Z)}{1 - \alpha^2} \quad (2.6.6)$$

Finally, it is possible to show that the skewness or $\langle (Y - \langle Y \rangle)^3 \rangle$ is given by

$$\text{skew}(Y) = \frac{\text{skew}(Z)}{1 - \alpha^3} \quad (2.6.7)$$

Equations (2.6.6) and (2.6.7) indicate that the shape of the distribution of Y is given by the shape of the Z distribution but the scaling from Z to Y is controlled by the value of α .

2.7 Moments

In this section the moments of various distributions are tabulated for easy reference.

First consider a distribution in which the numbers are confined to a range $\mu \pm \Delta$. A one parameter model for such a distribution could be

$$P_n(x) = \frac{n+1}{2n\Delta} \left(1 - \frac{|x|}{\Delta} \right)^n$$

where $|x| < \Delta$. Notice that as n increases the $\lim P_n(x) = \frac{1}{2\Delta}$ which corresponds to a uniform flat distribution. The variance of P_n is given by

$$\text{var}(P_n) = \int_{-\Delta}^{\Delta} P_n(x) x^2 dx$$

$$= \frac{\Delta^2}{3} \frac{n+1}{n+3}$$

As n ranges from 1 (triangular distribution) to ∞ (uniform distribution), the variance changes by a factor of 2. Although the variance is a continuous function of n , the dependence on n is quite weak. Finally the skewness of P_n is always zero since skewness measures the asymmetry of the distribution.

A Gaussian distribution is given by

$$P_G(x) = \frac{1}{\sigma\sqrt{2\pi}} e^{-\frac{x^2}{2\sigma^2}}$$

The first three moments are $\mu, \sigma^2, 0$. Again we have a symmetric distribution and hence the skewness is zero.

The Poisson distribution,

$$P_p(x, \mu) = \frac{\mu^x}{x!} e^{-\mu},$$

is interesting in that the discrete case is easier to manipulate than the continuous case. For example consider computing the mean

$$\langle x \rangle = \sum_{x=0}^{\infty} x \frac{\mu^x}{x!} e^{-\mu} = \sum_{x=1}^{\infty} \frac{\mu^x}{(x-1)!} e^{-\mu}$$

It is now possible to set $y=x-1$ and to do the summation to obtain $\langle x \rangle = \mu$. In general it is possible to express the n^{th} moment in terms of $(n-1)^{\text{th}}$ moments. Thus one can slowly proceed to higher moments finding that $\text{var}(P_p) = \mu$ and $\text{skew}(P_p) = \mu$. Before the reader jumps to a hasty generalization let me point out that the 4th moment is $3\mu^2 + \mu$.

Astrophysicists often use distributions which are generated by shot noise models. In such models one assumes that the observed light curve is composed of a large number of superimposed flares. In the standard shot noise model one assumes that all the flares are identical. Let $H(\tau)$ be the intensity of a single flare after time τ from the beginning. Then the observed flux is

$$I(\tau_0) = \int Z(\tau) H(\tau_0 - \tau) d\tau$$

where $Z(\tau) = 1$ when a flare begins and 0 otherwise. If $**$ denotes convolution then the above can be written as

$$I = Z**H.$$

where one thinks of H as being the impulse response function and Z as a series of impulses.

To compute the mean we assume that the process is stationary (the mean is not a function of time). Since it makes no difference when the mean is computed we will do it at time $\tau = 0$. Thus

$$\langle I \rangle = \langle I(0) \rangle = \langle \int Z(\tau) H(-\tau) d\tau \rangle$$

Since the expectation is calculated for a given time we can interchange the order of integration and expectation to obtain

$$\langle I \rangle = \int \langle Z(\tau) H(-\tau) \rangle d\tau$$

$$= \int \langle Z(\tau) \rangle H(-\tau) d\tau$$

since $H(\tau)$ is a constant for any given τ . Since the process is stationary the $\langle Z(\tau) \rangle$ is constant and is generally associated with the symbol λ . We note that λ is the mean shot rate and has units of inverse time. So at last

$$\langle I \rangle = \lambda \int H(\tau) d\tau.$$

The variance is slightly more tricky. We have

$$\text{var}(I) = \text{var}(I(0))$$

$$\begin{aligned} &= \langle \int Z(\tau) H(\tau) d\tau \int Z(\tau') H(\tau') d\tau' \rangle \\ &= \iint \langle Z(\tau) Z(\tau') \rangle H(\tau) H(\tau') d\tau d\tau' \end{aligned}$$

Now we must make use of the assumption that the Z 's are uncorrelated.

Therefore

$$\langle Z(\tau) Z(\tau') \rangle = 0 \text{ if } \tau \neq \tau'$$

If $\tau = \tau'$ we have $\langle Z^2(\tau) \rangle$ but, since by assumption Z is either 0 or 1 we have $\langle Z^2(\tau) \rangle = \langle Z(\tau) \rangle = \lambda$. Thus

$$\text{var}(I) = \lambda \int H^2(\tau) d\tau.$$

The same reasoning can be applied to the skewness to obtain

$$\text{skew}(I) = \lambda \int H^3(\tau) d\tau$$

Table 2.2

Moments of Various Distributions

DISTRIBUTION	MEAN	VAR	SKEW
$\frac{n+1}{2n\Delta} (1 - \frac{ x ^n}{n\Delta})$	μ	$\frac{\Delta^2(n+1)}{3(n+3)}$	0
Gaussian	μ	σ^2	0
Poisson	μ	μ	μ
shot noise $H(t) = h e^{-t/\tau}$	$\lambda\tau h$	$\lambda\tau \frac{h^2}{2}$	$\lambda\tau \frac{h^3}{3}$
shot noise $H(t) = h, t < \tau$	$\lambda h\tau$	$\lambda\tau h^2$	$\lambda\tau h^3$
AR	$\frac{\langle Z \rangle}{1-\alpha}$	$\frac{\text{var}(Z)}{1-\alpha^2}$	$\frac{\text{skew}(Z)}{1-\alpha^3}$
AR (uniform Z)	$\langle Y \rangle$	$\frac{\langle Y \rangle^2}{3} \frac{1-\alpha}{1+\alpha}$	0

2.8 Numerical Results

Analytical results should be complemented with numerical work, since using both methods often allows one to reach greater understanding. In this section I briefly discuss my program (called PHANTOM) which generates "phantom" data. This program has been used to test other programs as well as simple (analytic) models.

PHANTOM produces a data file in exactly the same format as typical X-ray rates files. Thus programs can use phantom data without modification. It is currently possible to generate two types of time series: an autoregressive process (first or second order) and shot noise (either square or exponential shots). To the basic time series one can add a constant term, sine waves, or noise. The program first generates a series of "true" rates μ_i . If the user requests it the program then constructs a series x_i such that x_i has a Poisson distribution about μ_i . The method used allows the user to generate the same series of μ_i (for the same starting seed) whether or not noise is added. The noise term is Poisson distributed if there are fewer than 50 counts per bin. For larger rates the FORTRAN code which generates Poisson noise fails and so a Gaussian approximation is used with $\sigma^2 = \mu$. Although the difference between Poisson and Gaussian noise is small for large rates, I find that the difference is easily detected (see Table 2.3).

As a demonstration of what one can discover consider Table 2.3. On the first line, I consider the mean, variance and skewness of a pure autoregressive (AR) process. The expected values are 100.0, 175.4, and 0.0 respectively. The plus or minus values are the single sample uncertainty, as determined by running the program 10 times. Notice that as one goes to higher moments the uncertainty increases drastically.

On the second line of Table 2.3 I give the observed mean, variance and skewness for constant rate but with added noise. The expected values are 100, 100 and 0.0. If the noise had a Poisson distribution then the skewness would be 100 but as I mentioned I am using a Gaussian approximation and so skewness = 0.0. Again the uncertainty increases with the higher moments.

Finally, in the third line of Table 2.3 I consider adding noise to the autoregressive process generated in the first line. Notice that the variance of the sum is equal to the sum of the variances due to the AR process and due to the noise. However the skewness does not add. To see this let $P(\mu)$ be the probability that the signal is at a level of μ (without noise). Further let $P(x; \mu)$ be the probability of seeing x photons if the expected number is μ . The probability of seeing x photons during the entire observation is

$$P(x) = \int P(x; \mu) P(\mu) d\mu$$

The expectation of x^n is given by

$$\langle x^n \rangle = \iint x^n P(x; \mu) dx P(\mu) d\mu.$$

If it is possible to do the inner integral, then one can express $\langle x^n \rangle$ in terms of the various moments of $p(\mu)$. For Gaussian noise we find that $\text{skew}(\text{AR}+\text{noise}) = \text{skew}(\text{AR}) + 3\text{var}(\text{AR})$. For Poisson noise (see Appendix B of Sutherland, Weisskopf and Kahn 1978), we find $\text{skew}(\text{AR}+\text{noise}) = \text{skew}(\text{AR}) + 3\text{var}(\text{AR}) + \text{mean}(\text{AR})$.

TABLE 2.3

MOMENTS OF VARIOUS DISTRIBUTIONS (EXPERIMENTAL)

	MEAN	VAR	SKEW
pure AR	100.0±1.3	171.7±16.3	71.1±307.8
pure noise	99.6± .2	100.9± 2.1	-5.3± 72.3
AR+noise	99.6±1.4	275.1±18.7	594.1±444.8

3. DETERMINATION OF TIME SCALES

3.1 Chapter Overview

In the last chapter we saw how to use χ^2 first to detect variability and second to determine the source variance. Given an excess variance one next proceeds to measure the time scale for variability. There is no standard method that works for all cases, so some human judgement is often used. If the observation length is short, relative to any apparent time scale, then one can measure the time for the source to double its flux, the source doubling time. For a longer observation the peak-to-peak time, or the time interval between peaks in the flux, is perhaps the physically most useful time scale. For a long observation one can apply powerful statistical methods to extract the time scale. These methods include computing the auto-correlation function (related to the power spectrum) and computing variance as a function of the bin size.

3.2 Short Observations

If the apparent time scale is much longer than the observation length then one will only see slow trends in the data. In order to characterize the data one generally fits a polynomial to the observed rate. If a straight line provides an acceptable fit to the data then the "doubling time" τ_d is a useful quantity. I define the doubling time to be the mean intensity divided by the slope. Thus the doubling time measures how long it would take the source to double its flux if the observed trends were to continue.

The doubling time is useful for several reasons. First, flickering sources rarely vary by as much as a factor of 10, and so the time for the flux to double will provide an order of magnitude estimate of the true time

scale. Secondly, the doubling time provides an estimate for how long to observe the source when requesting additional observations.

If a slow trend fits the observation then the slope of the trend is interesting since Fabian and Rees (1979) (see Section 1.4) have proposed a theoretical upper limit to $\Delta L/\Delta t$. For variability near this limit, one can strongly constrain various physical models (see Chapter 6).

3.3 Medium Length Observations

When one has observed a source over only a few variations it is difficult to define the observed time scale in a formal manner. In this case one can examine the light curve by eye. The time scale that one looks for is the time from one extreme to another for individual events. Due to noise it is not generally possible to locate extrema precisely. However this peak-to-peak time scale is physically very important since it provides an upper limit to the source size. Thus in the absence of relativistic bulk motion

$$\Delta\tau_{pp} \lesssim R/c$$

This is due to the fact that some parts of the source are closer to the observer than others, and can be separated by at most a distance R along the observer's line of sight.

3.4 Long Observations: The Auto-correlation Function

When the observation length is long relative to the time scale of variability then one can compute the auto-correlation function. Given a set of observations Y_j with statistical errors σ_j we compute the auto-correlation function with

$$\rho(u) = r(u)/r(0) \quad (3.4.1)$$

$$r(u) = \frac{1}{N} \sum_{i=1}^{N-u} \frac{(Y_i - \langle Y \rangle_w)(Y_{i+u} - \langle Y \rangle_w)}{\sigma_i \sigma_{i+u}} \quad (3.4.2)$$

The variable u is the lag time. Jenkins and Watts (1968 p. 772f) showed that using $1/N$ instead of $1/(N-u)$ in the definition of $r(u)$ introduces a bias, however the biased function has a smaller mean square error.

The definition of $\rho(u)$ shows that it is directly related to reduced χ^2 . Thus in order to compute a meaningful auto-correlation function, χ_v^2 should be significantly different than 1.0. Some people feel that the auto-correlation function can magically pull a signal out of quiet data. Although this may be possible, it has never happened in any of my tests. The auto-correlation function is useful only if a χ^2 test shows that a constant is an unacceptable fit to the data.

Weisskopf, Kahn and Sutherland (1975) pointed out that photon noise, being uncorrelated, contributes to $\rho(0)$ but not to $\rho(u)$ if u is non-zero. They recommend correcting for noise by multiplying $\rho(u)$ by a correction factor F for all non-zero lags. An expression for F is

$$F = \frac{\chi^2}{\chi^2 - N} \quad (3.4.3)$$

where N data points have been used. This expression makes it clear that if $\chi_v^2 \sim 1.0$ then the correction factor will be quite large, i.e. the ratio of signal to noise will be very small.

The auto-correlation function of shot noise is given by

$$r(u) = \lambda \int H(t) H(t+u) dt \quad (3.4.4)$$

We see that the auto-correlation function is no more than the convolution of the impulse response function with itself. If $H(t) = he^{-t/\tau}$ then

$$r(u) = \frac{\lambda \tau h}{2} e^{-u/\tau} \quad (3.4.5)$$

and of course

$$\rho(u) = e^{-u/\tau} \quad (3.4.6)$$

For a first order autoregressive process the autocorrelation function is

$$\rho(u) = \alpha^u = e^{-u/\tau} \quad (3.4.7)$$

where $\tau = -1.0/\ln(\alpha)$ (see Jenkins and Watts 1968). This clearly shows the relationship between α and τ in addition to the similarity between shot noise and an autoregressive process.

The maximum likelihood estimate for α is $\rho(1)$ (see Jenkins and Watts 1968). Although one feels that it should be possible to obtain a better result using more than one point, numerical tests have shown that the best estimate is $\rho(1)$ alone. This is due to the correlations in the data, which cause the deviation of $\rho(2)$ to be in the same direction and slightly greater than the deviation of $\rho(1)$. For no Poisson noise it is possible to estimate the uncertainty in $\rho(1)$ with

$$\sigma^2 \approx [1 - \rho(1)^2]/N \quad (3.4.8)$$

(see Box and Jenkins 1976, p. 34).

The above were demonstrated numerically. A first order autoregressive process was used to generate 2000 points. The random variable Z varied uniformly between 0 and 20. Since $\alpha = .9$ the mean rate was 100 ct/bin. Ten runs were made without adding counting noise and the mean for these runs was .8970 (see Table 3.1). The deviations about the mean were $\pm .0093$, compared to a predicted quantity of .0097 using equation (3.4.8). When photon noise was added the mean value for $\rho(1)$ dropped to .5731. However when one corrects each $\rho(1)$ for noise, the mean rises to .8936 which again is very close to .9, the expected value.

3.5 Long Observations: Variance vs. Bin Size

Another method of estimating the time scale for a long observation is to compute the excess variance (section 2.3) as a function of bin size. This method works because, for long bin lengths (sizes), one is averaging over several fluctuations. This causes the variance to decrease. As the bin size decreases then, at some point, all fine scale structure is "resolved out". Thus for short bin sizes the variance is constant. The overall effect is that, as one increases the bin length, the variance is constant for a while, begins to roll over when the bin length equals the characteristic time scale for variability and for large bin lengths decreases monotonically.

Define B_n to be the binned data where n data points are averaged into a single bin. Thus

$$B_{n_i} = \frac{1}{n} \sum_{j=0}^{n-1} Y_{i+j} \quad (3.5.1)$$

TABLE 3.1

AUTOCORRELATION FUNCTION OF FIRST ORDER AUTOREGRESSIVE PROCESS

Trial	No Photon Noise	With Photon Noise	
	$\rho(1)$	$\rho(1)$	F $\rho(1)$
1	.8868	.5229	.8644
2	.9129	.6495	.9535
3	.8922	.5698	.8980
4	.9008	.5782	.8835
5	.9007	.5588	.8924
6	.8966	.5947	.9301
7	.9053	.5654	.8413
8	.8801	.5339	.8751
9	.8951	.5711	.8863
10	.8991	.5871	.9118
$x =$.8970	.5731	.8936
$\sigma_x =$.0093	.0374	.0322

In the remainder of this section I will suppress the subscript i . For a stationary process we find

$$\langle B_n \rangle = \frac{1}{n} \sum_{j=0}^{n-1} \langle Y_j \rangle = \langle Y \rangle \quad (3.5.2)$$

Now consider the variance of the binned signal,

$$\text{var}(B_n) = \frac{1}{n^2} \langle (\sum_{j=0}^{n-1} Y_j) (\sum_{k=0}^{n-1} Y_k) \rangle - \langle Y \rangle^2 \quad (3.5.3)$$

To evaluate the product of the sums, it is important to realize that the expectation of the product of any two terms is a function of only the difference between the indices. Thus $\langle Y_{i+1} Y_i \rangle = \langle Y_{i+2} Y_{i+1} \rangle$ etc. In the product of the two sums there will be n terms with the same index. If the indices are not the same then there will be $2(n-j)$ terms in which the indices differ by j . Plugging this information into (3.5.3) gives

$$\text{var}(B_n) = \frac{1}{n} \langle Y^2 \rangle - \langle Y \rangle^2 + \frac{2}{n} \sum_{i=1}^{n-1} (n-i) \langle Y Y_i \rangle \quad (3.5.4)$$

where $\langle Y Y_i \rangle$ is the expectation of the product of two terms with indices differing by an amount i . From the definition of the auto-covariance function we have

$$\begin{aligned} r(i) &= \langle (Y - \langle Y \rangle) (Y_i - \langle Y \rangle) \rangle \\ &= \langle Y Y_i \rangle - \langle Y \rangle^2 \end{aligned} \quad (3.5.5)$$

Substituting (3.5.5) into (3.5.4) gives

$$\text{var}(B_n) = \frac{1}{n} \langle Y^2 \rangle - \langle Y \rangle^2 + \frac{2}{n} \sum_{i=1}^{n-1} (n-i) (\rho(i) + \langle Y \rangle^2) \quad (3.5.6)$$

Now

$$\frac{2}{n^2} \sum_{i=1}^{n-1} (n-i) \langle Y \rangle^2 = \left(1 + \frac{1}{n}\right) \langle Y \rangle^2 \quad (3.5.7)$$

so (3.5.6) reduces to

$$\text{var}(B_n)/\text{var}(Y) = \frac{1}{n} + \frac{2}{n^2} \sum_{i=1}^{n-1} (n-i) \rho(i) \quad (3.5.8)$$

where I have used the definition of the auto-correlation function, $\rho(i)$.

3.6 Examples of Variance vs. Bin Size

First assume that there are no correlations in the data (white noise). For this case (3.5.8) reduces to

$$\text{var}(B_n)/\text{var}(Y) = 1/n \quad (3.6.1)$$

which shows that the standard deviation is proportional to $1/\sqrt{n}$ which is what one expects for independent samples of a distribution. In Figure 3.1 the curve $\alpha = .0$ corresponds to the case of no correlations in the data.

For a first order autoregressive process ($\rho(i) = \alpha^i$), it is possible to do the summation to obtain

$$\text{var}(B_n)/\text{var}(Y) = \frac{1 + \alpha}{n(1-\alpha)} - \frac{2\alpha(1-\alpha^n)}{n^2(1-\alpha)^2} \quad (3.6.2)$$

In Figure 3.1, I have plotted the square root of (3.6.2) vs. $\log_2(n)$ for $\alpha = .50, .90$ and $.99$. Since the time scale is $\sim -1/\ln(\alpha)$ we see that the curve remains horizontal out to large binnings if the time scale is rather long.

Finally the program to separate the excess variance from a data stream was tested. The results are shown in Figure 3.2. Since the data stream consisted of only 2000 points, the variance for the largest bin size was computed with only two binned points. Therefore the agreement with the theory is very good.

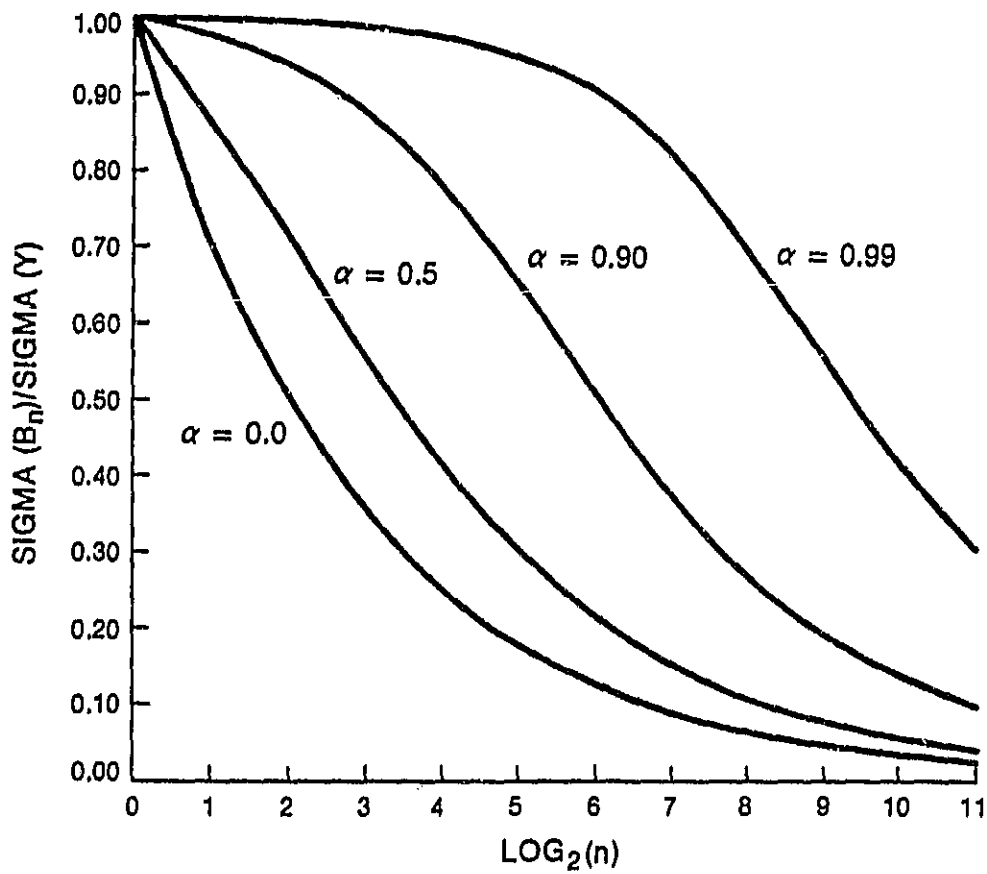
FIGURE CAPTIONS

Figure 3.1 -- The square root of (3.5.8) plotted as a function of n for a first order autoregressive process. For $\alpha = 0$, no correlations exist in the data whereas for $\alpha = .99$ the characteristic time scale is 99.5 bins ($\log_2(99.5) = 6.64$).

Figure 3.2 -- The results of a numerical experiment. Ten data streams were generated with a first order autoregressive model. For each data stream $\alpha = .90$ and 2000 points were generated. The curve represents the average and the error bars represent the single sample uncertainty.

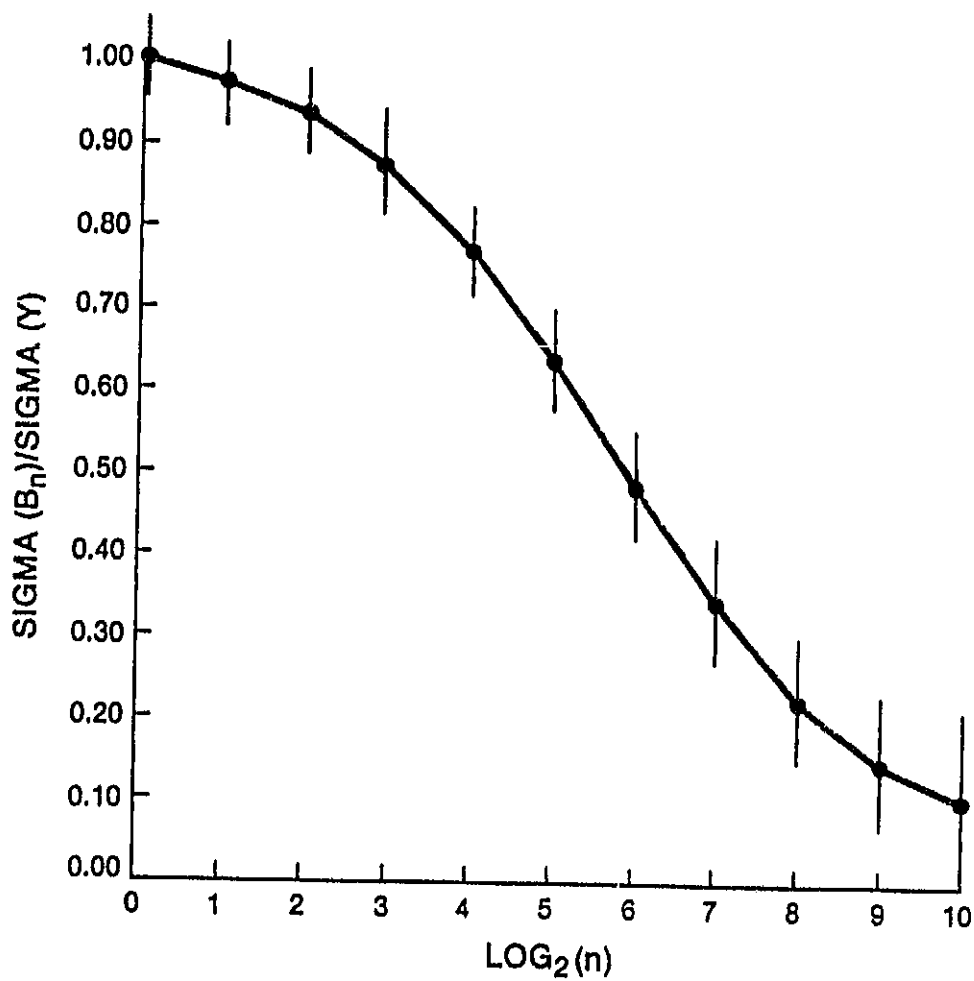
ORIGINAL PAGE IS
OF POOR QUALITY

SIGMA VS. BIN SIZE
FIRST ORDER AUTOREGRESSIVE PROCESS
(THEORY)



ORIGINAL PAGE IS
OF POOR QUALITY

SIGMA VS. BIN SIZE FIRST ORDER AUTOREGRESSIVE PROCESS (EXPERIMENT)



4. IN FLIGHT PERFORMANCE

4.1 Chapter Overview

In this chapter I will discuss the in-flight performance of the Goddard instrument on board HEAO-1 and how this performance affects timing experiments. The Goddard experiment rejects particle events with over 99% efficiency; this small residual background noise can be further reduced by selecting times corresponding to low values of McIlwain L. Detector offsets were refined in flight and any remaining offset uncertainties can be neglected. The uncertainties in the aspect solution are also discussed. Finally, a variance analysis was performed on blank sky points. These observations prove that the systematics are quite small.

4.2 The Instrument

The Goddard experiment on HEAO-1 was a gas filled proportional counter. For a complete discussion of the detector see Rothschild et al. 1979. Here I will only be concerned with some of the general properties of the instrument. X-rays enter the gas volume via collimators on the front of the instrument (see Figure 4.1). These X-rays photoionize the gas (either argon for the medium energy detector MED or xenon for the high energy detectors HED's). These photoelectrons produce a local region of ionization which gives rise to a current pulse. In Figure 4.2 a cross section of the instrument is displayed with the anode and cathode wires coming out of the page. The voltage is controlled such that the current generated is proportional to the initial energy of the X-ray.

Proportional counters are relatively inexpensive and can be built with large collecting areas. In Appendix E, I point out the importance of large area detectors. Proportional counters (like most X-ray detectors)

also respond to the passage of charged particles. In the near Earth environment the count rate due to charge particles can be 100 times greater than the X-ray count rate for extragalactic sources. This background is also a strong function of the spacecraft's location in the Earth's magnetic field. Thus, as the spacecraft moves along its orbit, one expects a time variable background signal.

Charge particles rejection makes use of the fact that X-ray events tend to be localized in the volume whereas particles tend to ionize along tracks (see Mason and Culhane 1983). Methods of rejection fall into two broad classes; pulse shape discrimination and anticoincidence. It should be clear that localized X-ray events should give rise to pulses with a mean shape different than the pulses produced by particle tracks. This method has been successfully used by others (see Gorenstein and Mrowka 1968).

The Goddard instrument did not use pulse shape discrimination but rather relied entirely on anticoincidence. To use an anticoincidence method the gas volume is divided into many small cells (see Figure 4.2). As implied by the figure the cells are long and thin. Thus it is possible for a particle travelling parallel to a wire to stay entirely within one cell and not trigger the anticoincidence logic. Due to the small size of the cells this should be quite rare ($\sim .07\%$). Newer detectors (Bailey, Smith and Turner 1978) have an "end veto" system to detect particles travelling along a wire.

Low energy particles can also escape the anticoincidence logic, by losing most of their energy to a single cell. To provide protection from these events an additional surface layer is provided which is not exposed to X-rays. For MED and HED2 three sides of the gas volume are protected by such a system (the V2 rate counts triggers on the sides and V1 on the

bottom). HED1 and HED3 are protected along the top surface by a veto layer. In order not to attenuate the X-rays, the gas in the veto layer is made of a low Z material (propane). The propane does respond to particles and so provides the veto signal.

Finally it is possible to monitor the internal background of the Goddard detectors. Each detector has two different size collimators, one having roughly twice the field of view of the other. Thus any isotropic emission, such as X-rays from the X-ray background, that comes down the collimator is detected twice as strongly in the large field of view. The count rate from non-collimated events will be the same in both fields.

4.3 Particle Discrimination

For the Goddard instrument the total number of anticoincident events are recorded every 40.96 sec. Each 40.96 sec interval is called a major frame. The anticoincident rate is proportional to the number of charged particles transversing the detector. To test for charged particle contamination I have plotted the total xenon detector (HED3) count rate vs. anticoincidence in Figure 4.3. The data were taken from a blank sky observation (see section 4.6) on day 632 of 1977 (Sept. 24, 1978). Most of the scatter in the plot is due to counting statistics. However, a slight upward trend can be seen. A least squares straight line was fitted to the data and the fit parameters are listed in Table 4.1. The slope of the line illustrated in Figure 4.3 indicates that the variable rate is at a level of only .59% of the anticoincidence (particle) rate. Also listed in Table 4.1 are the fits for various discovery scalars (DS). Discovery scalars 1 and 2 are the rates for the two fields of view for the first layer only of the detector. Discovery scalars 3 and 4 are the second layer rates. Discovery scalars 1 and 3 always corresponds to the rate in the 3^0 field of view.

TABLE 4.1

SLOPE OF BEST FIT LINE

Det	DS	Rate vs. Anti(percent)	Rate vs. McIlwain L ct/(sec-L)
HED2	Total	1.46 ± .18	4.5 ± .8
	1	.62 ± .10	2.4 ± .4
	2	.59 ± .12	1.8 ± .5
	3	.21 ± .04	.3 ± .2
	4	.04 ± .05	.0 ± .2
MED	Total	.78 ± .08	2.8 ± .4
	1	.36 ± .05	1.3 ± .2
	2	.35 ± .04	1.1 ± .2
	3	.04 ± .03	.1 ± .2
	4	.03 ± .02	.2 ± .1
HED3	Total	.59 ± .04	2.8 ± .2
	1	.16 ± .03	.8 ± .1
	2	.21 ± .02	.9 ± .1
	3	.12 ± .01	.5 ± .1
	4	.10 ± .01	.5 ± .1

Table 4.2

 χ^2 /DOF FOR VARIOUS MODELS

DET	DS	CONSTANT	ANTI	MCILWAIN L	CONSTANT (L < 1.2)
HED2	Total	381.6/261	305.4/260	337.7/260	234.6/197
	1	320.5/261	275.9/260	281.6/260	195.4/197
	2	263.6/261	238.8/260	249.8/260	187.5/197
	3	260.2/261	239.1/260	257.1/260	179.5/197
	4	270.1/261	269.6/260	270.1/260	200.3/197
MED	Total	433.8/313	327.4/312	367.8/312	243.5/233
	1	378.7/313	327.1/312	344.9/312	245.1/233
	2	385.9/313	300.2/312	342.1/312	239.5/233
	3	292.7/313	291.4/312	292.0/312	227.6/233
	4	281.1/313	280.1/312	277.9/312	210.9/233
HED3	Total	822.3/484	533.9/483	597.7/483	368.4/299
	1	572.6/484	528.5/483	530.9/483	339.4/299
	2	620.5/484	497.1/483	534.3/483	320.5/299
	3	599.7/484	511.1/483	543.5/483	365.1/299
	4	645.7/484	560.5/483	572.6/483	370.2/299

Several other points can be seen from Table 4.1. First the contamination in both fields of view is always about the same, which indicates that the particles not being vetoed are not coming down the collimators. This also shows that when one considers the "true" X-ray rate by subtracting the small field of view from the large, the residual contamination will effectively be zero. Another effect is the contamination in the first layer of HED3 is only one-third the level for HED2. Except for the propane veto layer on HED3 both detectors are very similar. This shows that the propane layer reduces the background noise by a factor of 3. Finally, the second layer of the MED (which is twice the thickness of the second layer of HED3) has an extremely small contamination.

In Figure 4.4 I have plotted the anticoincident rate vs. the McIlwain L value (see Appendix B). It is clear that the two rates are correlated. In Figure 4.5 I have plotted HED3 total rate vs. L. Again a slight upward trend can be seen in the data. The fit parameters are listed in the last column of Table 4.1. A good approximation to the slope for half the detector is 1 ct/sec per unit change of L. Comparing χ^2 (Table 4.2) for the fits to McIlwain L and the anticoincidence rate shows that anticoincidence is a slightly better model. However, we are not concerned about an exact fit at this point.

It appears from Figure 4.5 that the experiment spends much time at low values of L with low anticoincidence rates. In Figure 4.6 I display a histogram of how often various values of McIlwain L occur for two separate pointed observations. These histograms clearly show that excursions into large values of L are quite rare. It therefore was decided to discard data at large values of McIlwain L. Thus for the remaining of this work I only

consider data with McIlwain L values of less than 1.2. This means that $\sim 1/3$ of the previously good data are discarded. In Table 4.2 I show χ^2 for a constant for the data with $L < 1.2$. As can be seen the amount of data was reduced by a factor of $1/3$ and the excess variance was reduced by a factor of three.

4.4 Detector Offsets

The total number of source counts observed is related both to source flux F (counts per area per time) and also to the effective area A . Thus

$$C_S = FA \Delta\tau$$

For the Goddard detector we have

$$A = A_m \left(1 - \frac{|\theta_o|}{3.0}\right) \left(1 - \frac{|\theta_a|}{\theta_m}\right)$$

Where $A_m \sim 400$ cm, θ_o is distance in degrees from the center of the field of view to the source measured in the off-scan direction. The quantity θ_a is the distance measured in the along scan direction. Thus (θ_a, θ_o) form a coordinate pair in an orthonormal system. The angle θ_m is the opening angle in the along scan direction and can be 1.5 , 3.0° or 6.0° depending on the detector. The opening angle in the off scan direction was always 3° . The above shows that the detector has a simple pyramid response to off axis sources.

It would be nice if one could measure (θ_a, θ_o) directly. However what is measured is the look position of the star trackers. Therefore one must determine a set of rotation angles (small) which will give the look position of the detector and this must be done in flight. Jean Swank and I determined these angles by looking at the area corrected rates as the

spacecraft scanned over the Crab nebula. If the rates are 'U' shaped the opening angle needs to be changed; if the curves are "S" shaped, the offsets need changing. In practice this procedure requires that one guesses new parameters and iterate a few times. In Figure 4.7 I have illustrated the rate for one scan over the Crab showing a flat response.

4.5 Pointed Aspect Errors

For the pointed data used in this thesis an additional aspect error existed. This was caused by the fact that HEAO-1 was designed to be a scanning spacecraft. Therefore, the standard (NASA) software package to determine aspect information from star tracker data, only worked while the spacecraft scanned. During pointed observations the aspect was extrapolated from the last scanning fix using only gyroscope data. The A-3 experimental group did work out improved solutions based on the star tracker data which they were to provide to us.

We obtained ~ 25 aspect solutions from the A-3 experimenters. We found that for most cases the Goddard-supplied aspect was accurate to better than $.05^\circ$. An error of this size would produce an additional noise in σ_1/I of 2% for our $3^\circ \times 3^\circ$ field of view. This signal can only be detected for the brighter sources. Since we used the A-3 solution for most of the brighter sources and for the more variable weaker ones, we believe that the residual variations found for some of these sources are not related to aspect uncertainties.

4.6 Blank Sky Analysis

HEAO-1 had instruments looking out in two opposite directions which is acceptable as long as the spacecraft scans. In general, during a pointed observation, only one side could be targeted for a source. Thus during a minus-y point, when the other side of the spacecraft was pointed

at a source, the Goddard instrument was effectively pointed at a random place on the sky. The rates for all minus-y points were examined. If the field contained a known source then the rates were only quickly examined. This study turned up a solar flare that produced a flux in our detectors (see Appendix C). Also discovered was a flare that appears to be from a new "nearby" galactic source (mentioned in Appendix C and discussed in more detail in Tennant and Swank 1983).

If there were no HEAO-1 sources (flux $> 2 \times 10^{-11}$ erg/cm²-sec) in the field of view then the point was flagged as a "blank sky" observation. There were 49 points which were selected for the blank sky analysis. Basically one determines the excess variance for each observation in a manner similar to the active galaxy study. This analysis will provide an estimate for the residual non-source noise. In the next chapter I present a histogram of σ_B/B for the points separately, where one can compare this histogram to a similar one made for the active galaxies.

Here I will consider the results for all the blank sky observations added together. To do this one adds together the observed χ^2 values for each point separately. Since the background is a function of location on the sky, a separate background was determined for each pointed observation. The background rate was assumed to be constant throughout the point.

In Figure 4.8 I display σ_B/B (in percent) vs. bin size for bin sizes ranging from 5 sec to 90 min. As can be seen from the figure there is excess noise at the 1.2% level for the xenon detector and 1.6% level for the argon detector. Since the background counting rate in the xenon detector is ~ 1.4 times larger than the corresponding rate for the argon detector, we find the same, absolute amount of excess noise in both

detectors. Figure 4.8 also shows that the excess variance drops for the largest bin sizes of roughly 90 min. This indicates that the noise has a time scale of ~ 90 min or one spacecraft orbit.

In searching for the source of the excess variance one has two clues. First, the signal has the same magnitude in both the xenon and argon detectors and second the time scale is roughly 90 min. Although one might think that 90 min indicates residual particle contamination, I point out that this is not the case. All the 90 min time scale indicates is an orbital dependent effect, of which particle contamination is one possibility. I will argue that such contamination is not a problem.

In section 4.3, I showed that the count rate was proportional to McIlwain L . Since we have selected only $L < 1.2$ we can estimate the residual contamination. If we assume a uniform distribution then from section 2.6 we find

$$\sigma^2 = \frac{\Delta^2}{3} = \frac{1}{3} (2 \times .1 \text{ ct/sec})^2$$

$$\sigma = .06 \text{ ct/sec}$$

The factor of 2 appears since I am considering the entire detector and L ranging over $\pm .1$ causes a flux change of $\pm .1$ ct/sec in half the detector. Since the McIlwain distribution is not uniform but peaked we expect the actual contamination to be less than this estimate. The residual noise from the blank sky points has a level of 1.2% of 14 ct/sec or .17 ct/sec. Thus the McIlwain L effect can contribute at most a third of the observed excess noise.

Under some conditions we might expect the residual noise to be

proportional to the internal background. In Table 4.3 I have broken the total detector count rate up into an internal background and an external background (mostly X-rays from the sky). As can be seen the internal background for the xenon detector is three times greater than the internal background for the argon detectors. However the external background contributes roughly the same rate in both detectors. Since the residual noise is the same for both detectors, fluctuations in the internal background could not give rise to the observed effect.

To understand how the external background could give rise to such a signal one needs to know two things. First, as the detector is pointed at different areas of the sky the background varies by about 3%. Most of this variation is due to weak unresolved sources. Second, during a pointed observation the detector look position was not held fixed but was allowed to vary within a "dead band" which extends up to 1/2 degree from the target position. For typical observations the spacecraft tended to spend much time near the edge of the dead band and the look position tends to circle the dead band about once every orbit or 90 min. These two points lead me to believe that it is the spatial fluctuations in the X-ray background which give rise to the observed ~ 1% signal with roughly a 90 min time scale.

TABLE 4.3

TOTAL DETECTOR BACKGROUND COUNTING RATE

Argon	Internal	1.9 ct/sec
	External	9.4 ct/sec
Xenon	Internal	5.5 ct/sec
	External	8.7 ct/sec

FIGURE CAPTIONS

Figure 4.1 -- Cross sectional view of the xenon detector HED3 (or HED1).

Figure 4.2 (top) -- Detector grid connections for the argon detector MED (also LED and HED2). X-rays from the $3^{\circ} \times 3^{\circ}$ field of view are counted in the L1 or L2 rates. Rates R1 and R2 will contain X-rays from the other field of view ($3^{\circ} \times 1.5^{\circ}$ for MED). Veto rates V1 and V2 shield the detector from particles entering from the bottom or sides. (bottom) -- Detector grid connection for the xenon detector HED3 (also HED1). The propane layer rate is read out as rate V2.

Figure 4.3 -- Total count rate vs. the total anticoincidence rate for the xenon detector. The slight upward trend indicates that .59% of the particle events are being counted as X-rays. The linear correlation coefficient is r .

Figure 4.4 -- The total anticoincidence rate vs. McIlwain L.

Figure 4.5 -- Total count rate vs. McIlwain L for the xenon detector. An upward trend is visible in the data.

Figure 4.6 -- Histogram shows number of times a given value of McIlwain L occurs. A major frame corresponds to a 40.96 sec readout period. The distribution clearly shows a tail to higher values of L (where particle contamination is also higher).

Figure 4.7 -- The count rate in the second layer of the xenon detector for a single pass over the Crab nebula. Detector offsets were determined from the sum of many passes.

Figure 4.8 -- The excess noise (above Poisson) plotted as a function of bin size for two detectors. The plot is the sum of 46 different blank sky observations. The dashed curve was calculated (incorrectly) with the weights based on the observed number of counts. For the solid curve the calculation was based on the expected number.

ORIGINAL PAGE IS
OF POOR QUALITY

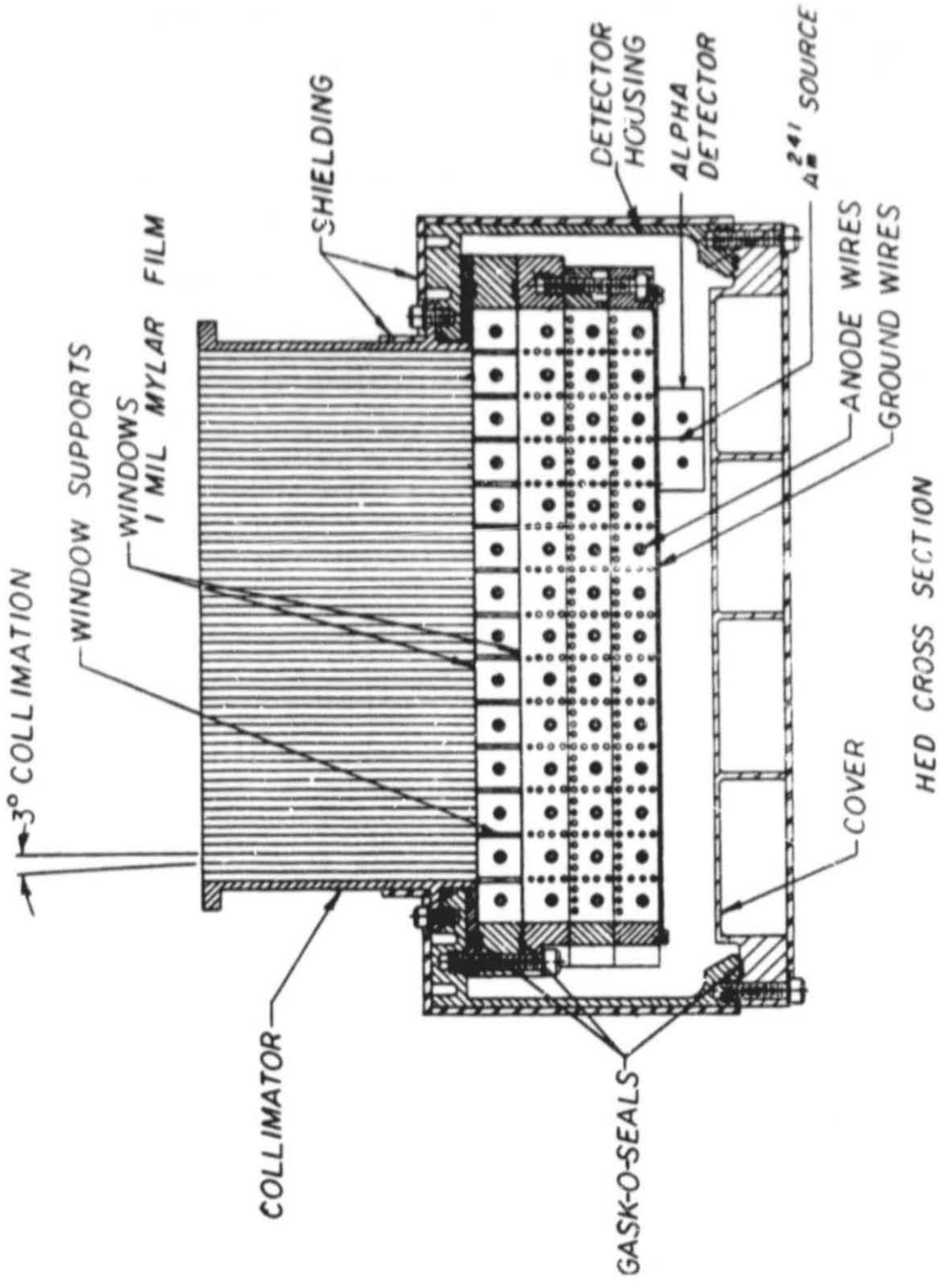
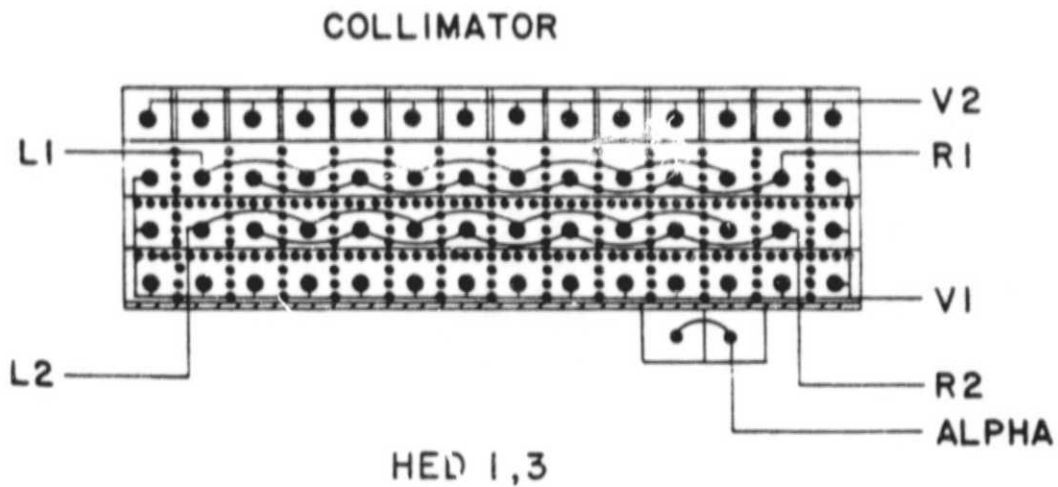
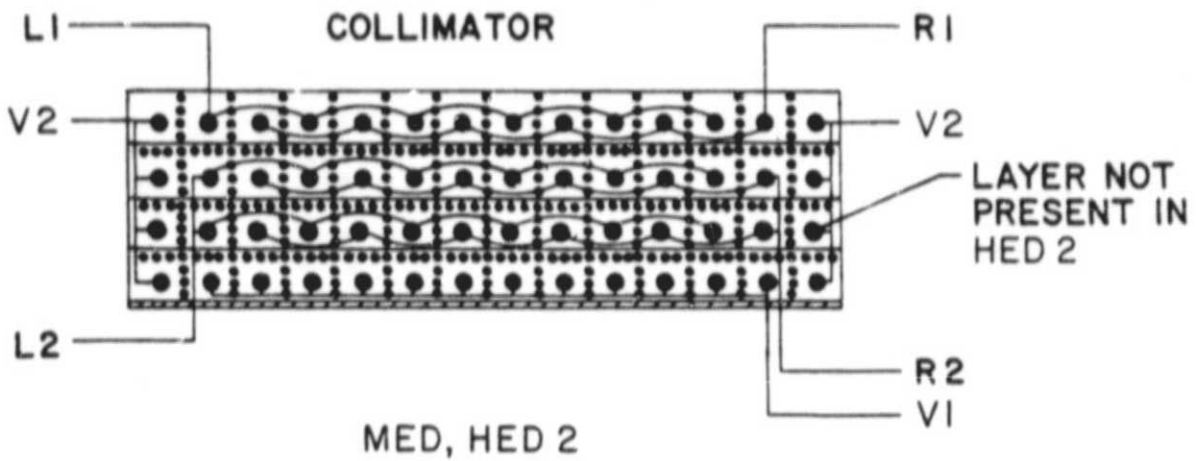


Figure 4.1

ORIGINAL PAGE IS
OF POOR QUALITY.



DETECTOR GRID CONNECTIONS

Figure 4.2

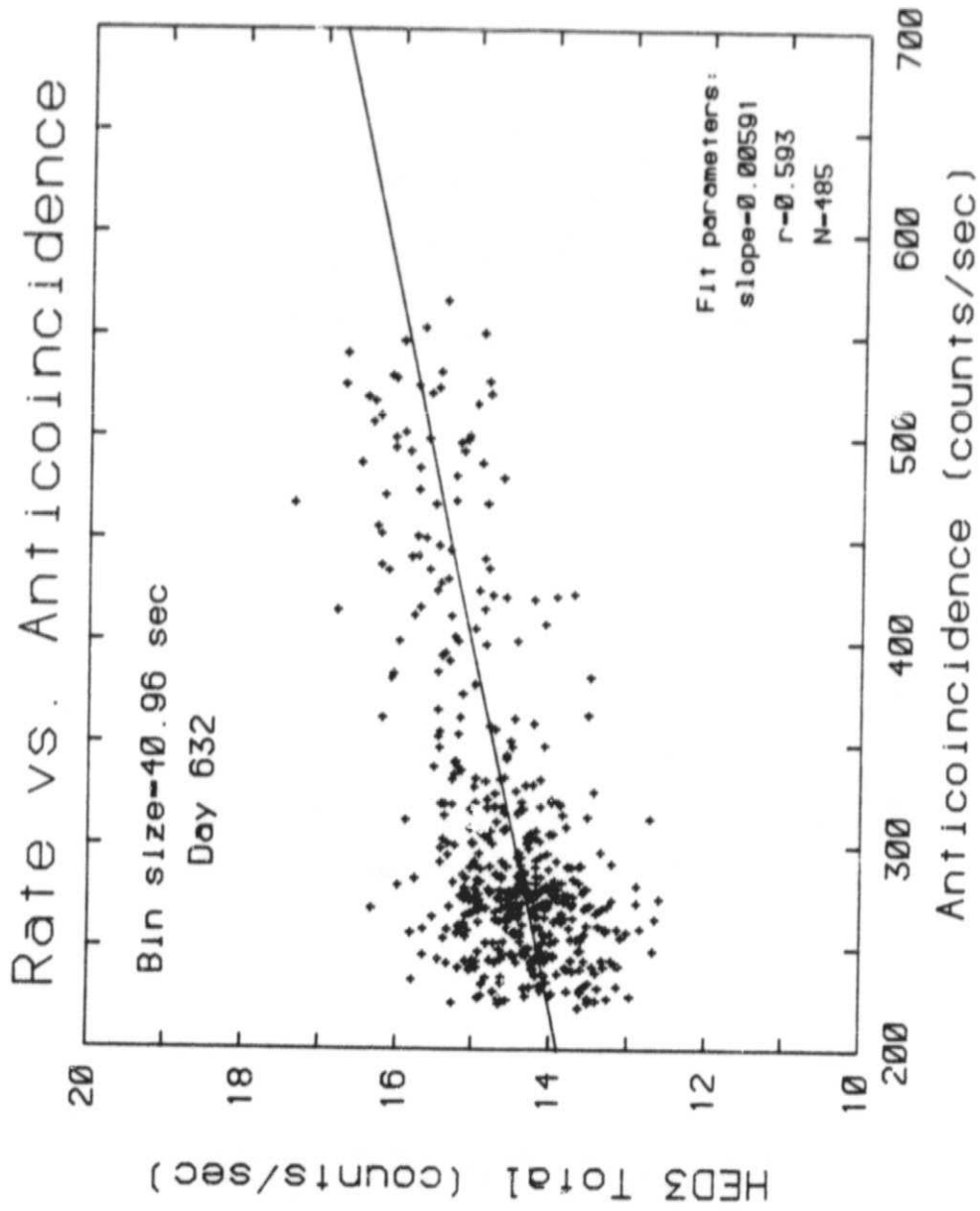


Figure 4.3

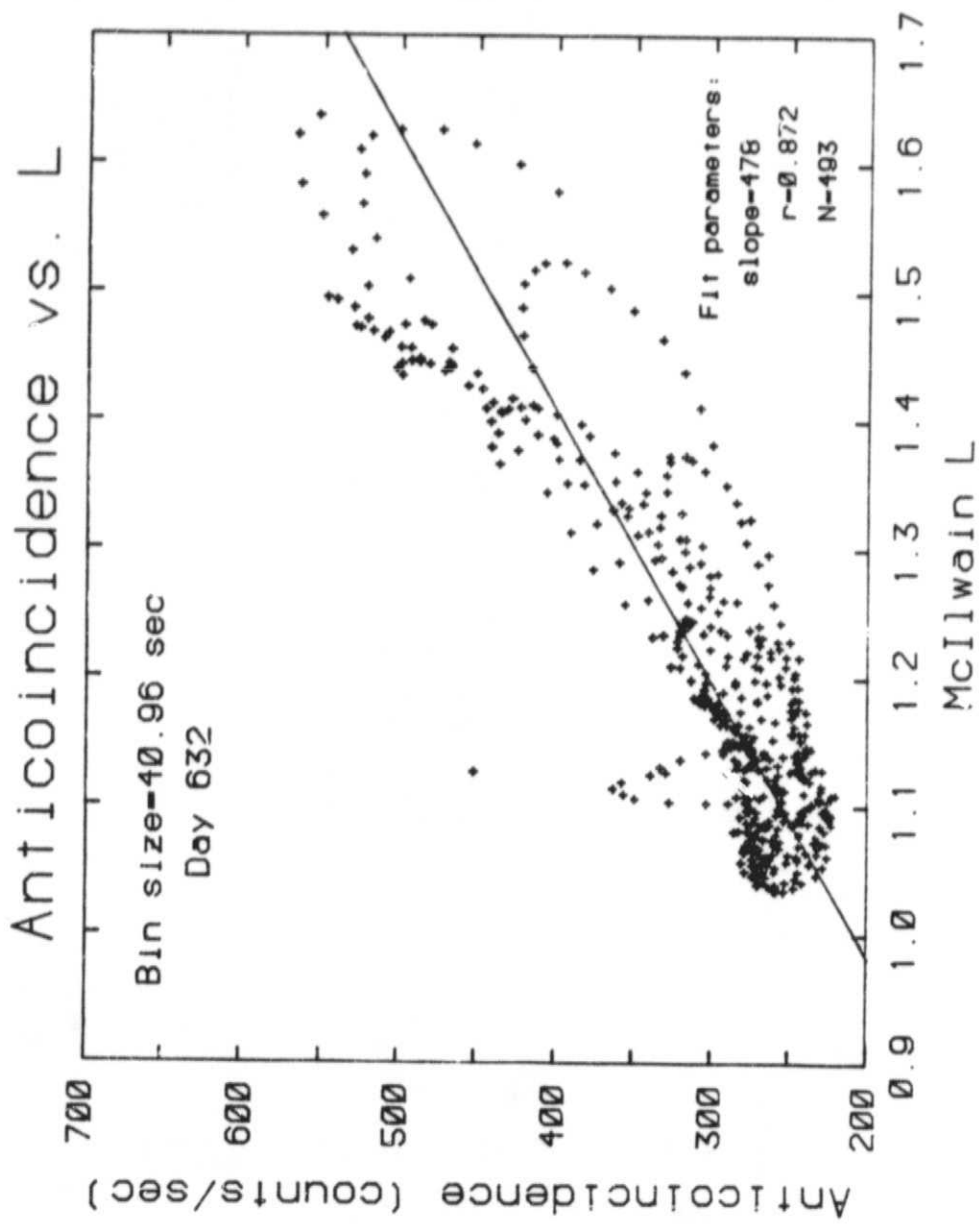


Figure 4.4

ORIGINAL PAGE IS
OF POOR QUALITY

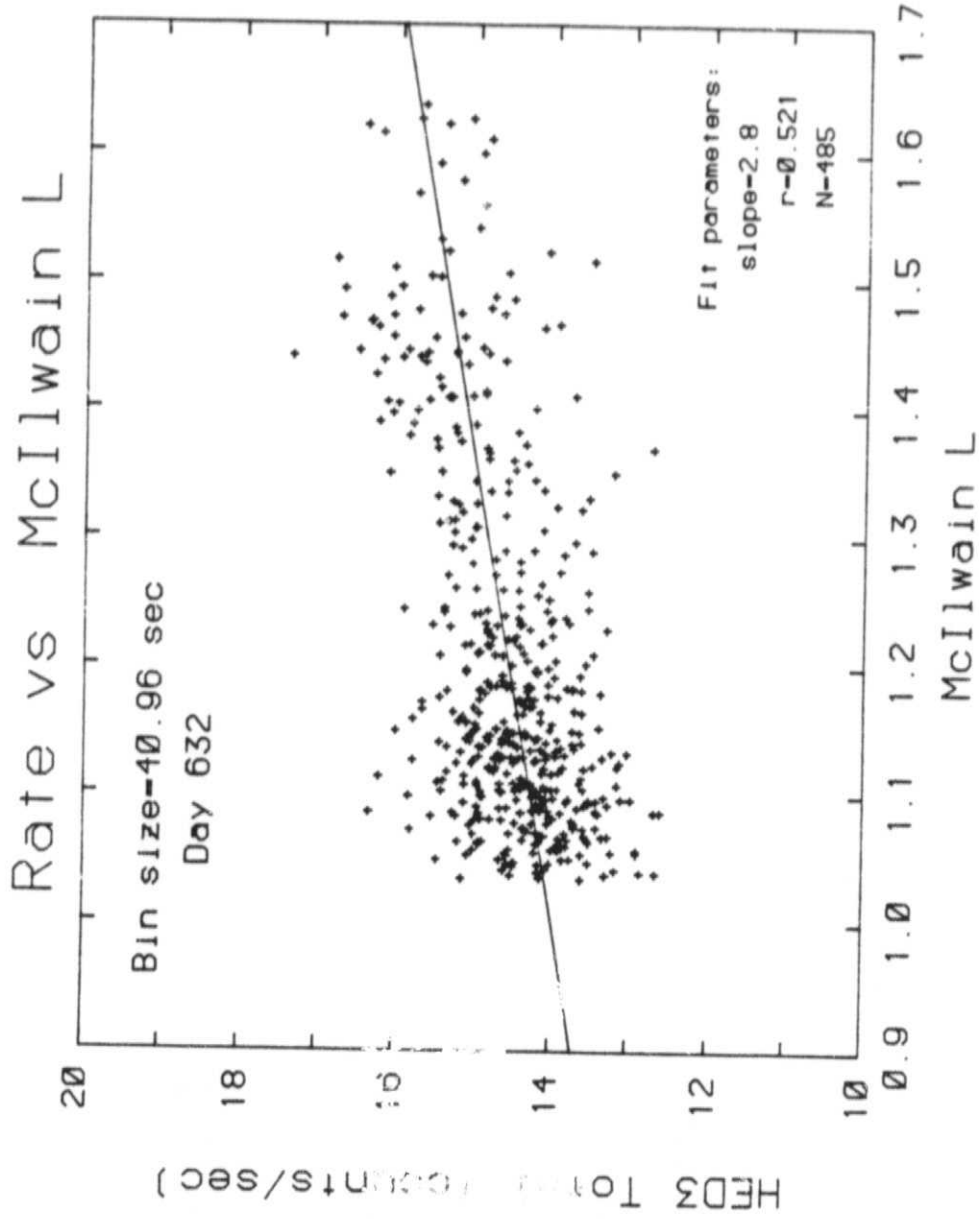


Figure 4.5

ORIGINAL PAGE IS
OF POOR QUALITY.

HISTOGRAMS OF NUMBER OF MAJOR FRAMES WITH A GIVEN VALUE OF L

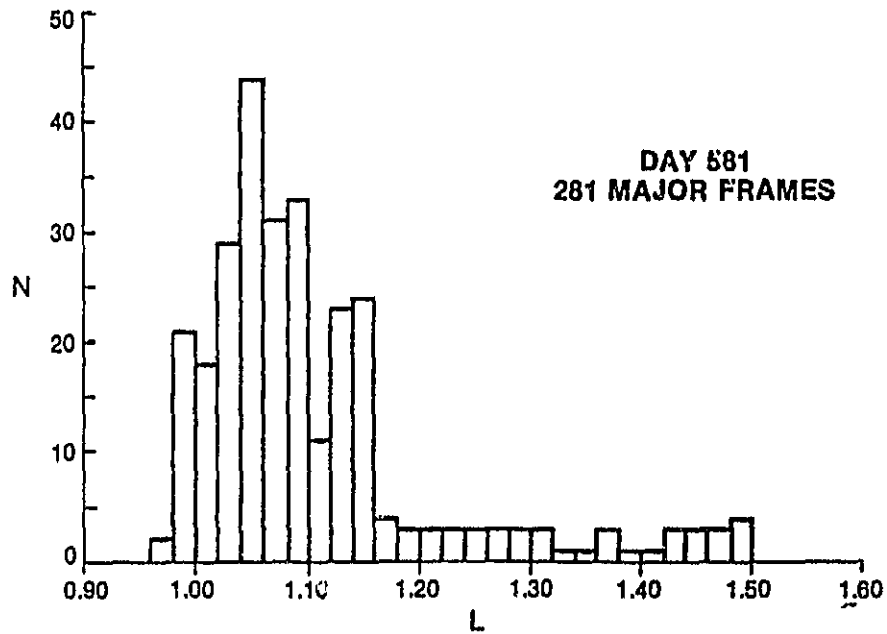
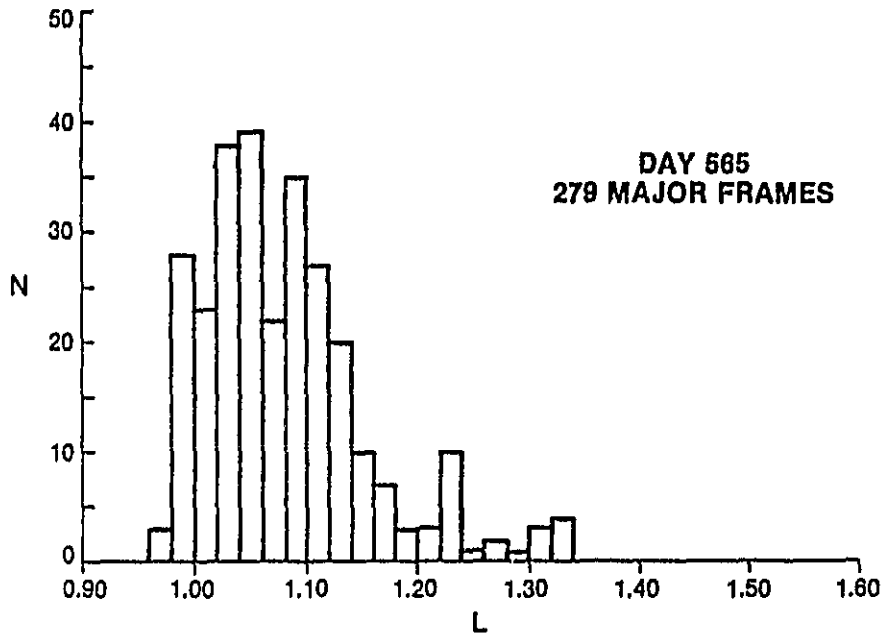


Figure 4.6

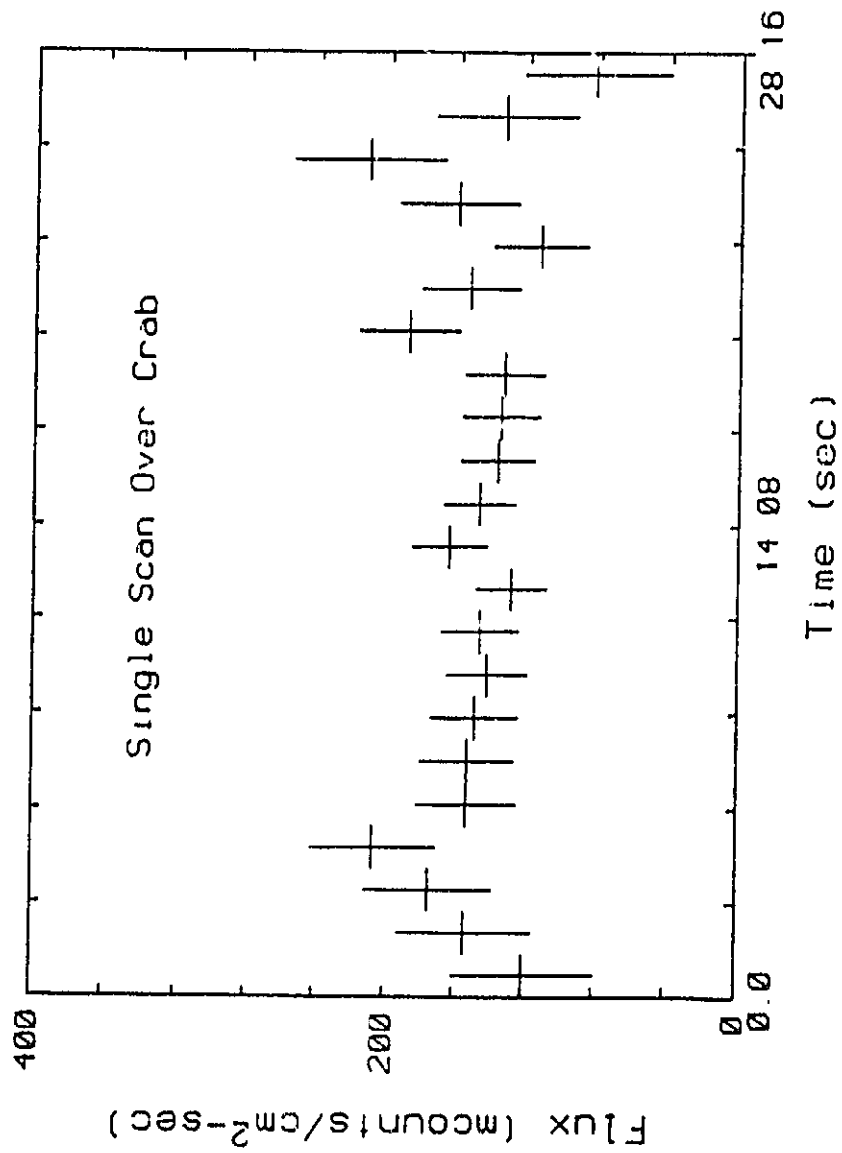


Figure 4.7

ORIGINAL PAGE IS
OF POOR QUALITY

BLANK SKY OBSERVATIONS

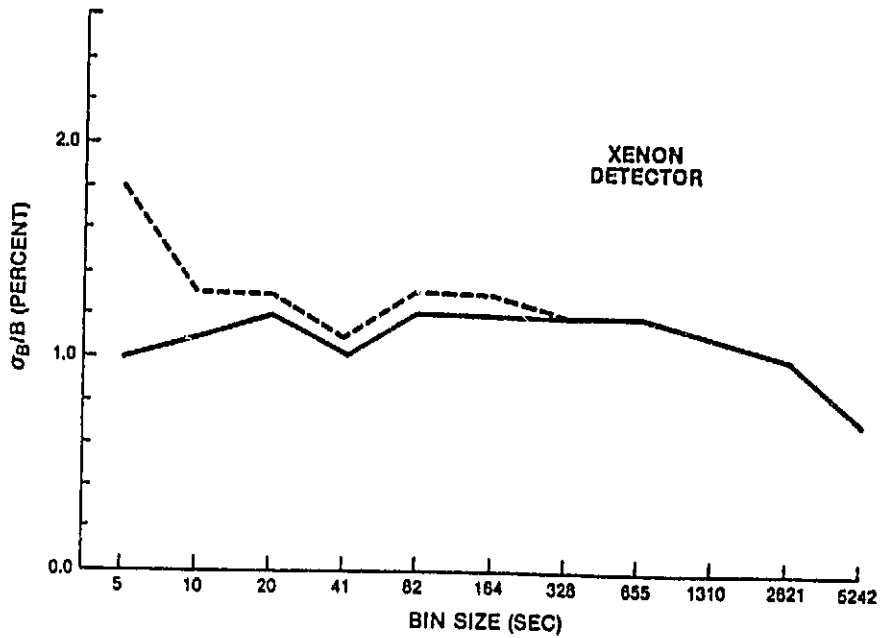
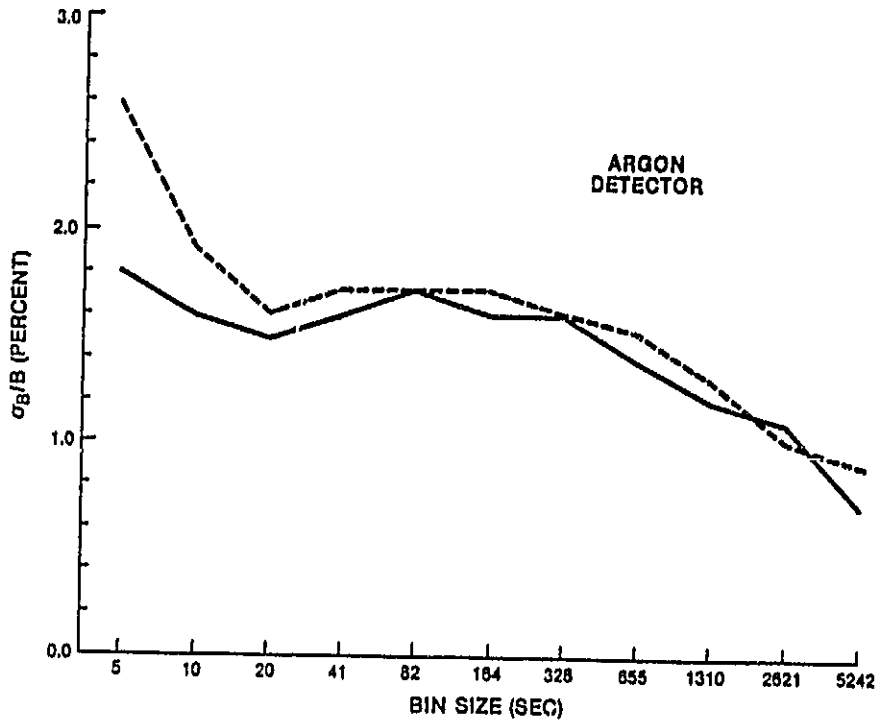


Figure 4.8

5. OBSERVATIONS OF ACTIVE GALAXIES

5.1 Chapter Overview

In this chapter, adapted from Tennant and Mushotzky 1983, the variance analysis of Chapter 2 is applied to the pointed observations of active galaxies. It is argued that most of the excess variance in the active galaxy observations is due to detector motion over fluctuations in the X-ray background. This noise term is seen in the observations of the blank sky. The most interesting source was NGC 6814 and Chapter 6 is devoted to a discussion of the variability of this source. NGC 3227, NGC 4151 and MCG-5-23-16 all showed variability consistent with a one day time scale. The last section of this chapter discusses the implications of the general lack of variability on time scales of less than one day.

5.2 Variance

For all HEAO-1 pointed observations at active galactic nuclei σ_I/I was determined for bin sizes ranging from 5.12 sec to 1024×5.12 sec \approx 87 min. The quantity σ_I/I is the standard deviation of the source divided by the source flux. This quantity measures an intrinsic property of the source and so is independent of distance. The results are summarized in Table 6.1. The first four columns contain information about the observation; column (1) gives the source name in alphabetic order, (2) the position, (3) the date of the observation where day 1 = JD 2,443,144.5 = 1977 January 1, and (4) the length of the observation in hours. Column 5 gives the mean flux for the observation in milli-counts/cm²-sec. Throughout this chapter I report fluxes in these units. A flux of 1 in the xenon detector corresponds to 1.0×10^{-11} erg/cm²-sec in the 2-10 keV band or 1.8×10^{-11} ergs/cm²-sec in the 2-20 keV band assuming a power-law

ORIGINAL PAGE IS
OF POOR QUALITY

TABLE 5.1

(1) OBJECT	(2) RA-DEC	(3) DATE	(4) LENGTH	(5) FLUX	(6) L	(7) α/β	(8) α/β	(9) α/β
CEN A	1322-428	384.5	4	49.5	0.57	1.4	<0.7	<1.0
CEN A	1322-428	507.7	11	36.0	0.43	2.8	1.8	3.0
CYG A	1957+100	488.0	0	8.5	95	5.0	<3.3	<0.8
ESO 141-G55	1017-580	488.4	9	3.4	10	<8.1	<5.7	<0.8
H 1049-595	1048-591	029.7	9	4.2	0.26	11.3	10.0	1.0
IC 1320A	1346-301	573.8	0	5.1	4.1	0.7	4.0	1.1
MCG-2-58-22	2302-000	523.2	0	4.3	34	<6.0	<4.0	<0.8
MCG-5-23-10	0945-307	407.7	0	8.1	1.0	7.0	5.7	2.0
MCG 8-11-11	0551+104	643.7	9	3.5	5.1	0.1	0.8	1.0
MK 142	1022+519	099.4	0	1.0	11	<21.7	<13.0	<0.7
MK 270	1352+000	079.4	13	1.2	3.0	30.5	15.7	0.0
MK 270	1352+000	097.4	7	1.2	3.0	<18.4	<11.2	<0.7
MK 335	0003+100	553.8	13	1.1	2.1	31.2	18.3	0.6
MK 421	1057+385	513.1	9	1.8	0.0	20.0	11.0	0.8
MK 421	1057+385	704.4	7	1.2	4.0	<27.0	<17.4	<0.6
I.K 104	1353+388	555.8	10	1.4	13	<14.4	<8.9	<0.8
MK 501	1052+398	018.8	0	2.7	10	<10.4	<6.0	<0.7
MK 509	2041-109	493.7	0	4.0	20	5.4	3.7	0.8
MK 509	2041-109	653.5	4	5.3	23	<6.8	<5.3	<1.3
MK 509	2041-109	657.4	18	5.4	24	<4.3	5.3	1.3
MK 509	2041-109	680.3	10	4.0	20	7.3	0.4	1.4
MK 509	2041-109	680.4	12	3.0	10	7.0	0.0	1.0
MK 509	0212-010	684.7	0	1.1	2.8	<19.8	<11.5	<0.6
M 02	0951+099	474.1	5	2.5	0.007	<7.4	<3.9	<0.5
NGC 520A	0121-353	520.0	0	2.1	2.4	17.3	<0.2	<0.6
NGC 931	0225+311	585.0	0	1.5	1.4	<18.7	<12.9	<0.7
NGC 2110	0548-075	047.0	5	5.0	0.87	<5.3	<3.3	<0.8
NGC 2902	0943-141	509.4	3	7.9	1.4	7.4	<2.5	<0.9
NGC 3227	1020+201	092.0	0	1.7	0.004	25.5	20.3	1.0
NGC 3783	1136-375	370.0	3	3.5	1.0	<0.4	<5.5	<0.9
NGC 3783	1136-375	554.8	13	3.1	0.89	14.7	0.7	1.2
NGC 4151	1200+397	340.5	3	10.1	0.38	4.7	3.4	1.5
NGC 4151	1200+397	524.1	3	19.3	0.73	5.8	0.5	5.7
NGC 4151	1200+397	532.1	4	22.8	0.80	<4.0	<4.2	<2.3
NGC 4151	1200+397	533.0	3	10.8	0.71	<2.8	<2.1	<1.8
NGC 5500	1410-030	574.0	0	5.0	0.04	0.0	0.1	1.5
NGC 5548	1415+254	500.9	0	5.7	5.4	<4.0	<3.1	<0.8
NGC 5548	1415+254	730.9	0	4.3	4.1	<5.4	<3.8	<0.8
NGC 6814	1940-104	483.0	7	4.1	0.40	13.0	13.3	0.4
NGC 7213	2200-474	511.4	0	4.2	0.49	<0.4	<5.8	<0.8
NGC 7409	2300+000	547.9	12	1.8	1.7	10.4	10.0	1.3
NGC 7582	2315-120	518.3	0	3.1	0.26	0.2	9.9	1.5
PKS 0548-322	0548-323	838.0	0	2.0	43	<10.1	<0.5	0.7
PKS 2151-304	2151-300	077.7	5	8.1	810	<5.2	5.1	1.0
2A 1219+305	1219+305	510.2	0	3.0	180	<0.5	<5.4	<0.8
3C 111	0415+379	011.2	0	3.9	29	<0.3	<0.4	<1.2
3C 120	0430+052	015.0	0	3.1	12	<7.2	<4.7	<0.7
3C 273	1220+023	533.0	0	9.4	800	4.0	3.3	1.5
3C 273	1220+023	546.4	0	0.5	720	<3.3	<2.3	<0.9
3C 273	1220+023	549.3	0	0.0	760	<3.4	<2.4	<1.0
3C 273	1220+023	551.2	10	0.7	740	<3.3	<2.4	<1.0
3C 382	1833+327	061.5	9	3.2	38	12.2	<0.1	<0.9
3C 380.3	1845+707	723.2	10	2.2	25	<14.1	<0.4	<0.8

NOTES:

(1) Alphabetic by source name

(2) RA(hours and mins) Dec(degrees and tenths)

(3) Beginning of observation, day of year 1977

(4) Length of observation in hours

(5) Cts/cm²-ksec

(6) 2-20 Kev luminosity (H=75 km/sec/Mpc) assuming no absorption, units=10¹³ ergs/sec

(7) 320s bin size

(8) 86m bin size

(9) 86m bin size

spectrum with energy index $\alpha = 0.7$. Columns (7) and (8) give the values of σ_I/I , in percent, for bin sizes of ~ 5 min and ~ 90 min. Finally in order to compare with the blank sky observations σ_I/B in percent is listed in column (9).

In Figure 5.2 σ_I/I , obtained using a 328 sec bin size, is plotted versus source intensity, in Figure 5.1. Since σ_I/I is computed using the entire observation, Figure 5.1 is relevant for time scales ranging from 300 sec to ~ 3 hr. The solid line in Figure 5.1 corresponds to a constant standard deviation of 0.4 m counts/cm-sec, which was estimated in the last section to be the upper limit for systematic errors. Thus any positive detections below this line could be due to residual sky plus detector noise. Only three objects, NGC 6814, NGC 4151 (one time), and Cen A (one time), lie significantly above the curve.

We have examined σ_I/I down to a bin size of 5.12 sec (a detector readout time). Because of counting statistics our upper limits at 5.12 sec are ~ 2 times larger than the corresponding values at 328 sec. Since there are fewer positive detections of variability at 5.12 sec than at 328 sec, we conclude that these objects do not show a large source of variance with time scales of less than 328 sec. We conclude that large-amplitude, $\sigma_I/I > 10\%$, short-term variations on time scales $5 < \tau < 10^4$ sec are not a characteristic of the X-ray emission from active galaxies.

As one goes to longer bin sizes, most of the residual non-source-related noise is averaged into a single bin. Since the spacecraft look position generally samples the entire area available to it during one spacecraft orbit, sky noise is greatly reduced for a 90 minute bin size. For a 90 minute bin size one also averages over the particle background for one spacecraft orbit. A plot of σ_I/I versus source flux for

a ~ 90 minute bin size is shown in Figure 5.2.

We have attempted to determine the systematics for the 90 minute bin size by performing the equivalent test for variability during observations of blank sky. Of 49 observations of blank sky, 17 were not constant at the 90% confidence level. Since for all active galaxies, except Cen A, the background gives more counts than the source, we would expect a similar fraction of the active galaxies to show variability. Thus we expect 18 ± 4 positive detections, when in fact the observed value was 21. Thus, to first order, the majority of our positive detections only indicate that there is a small amount of excess variance beyond counting statistics, not included in our χ^2 test for variability.

If the same excess variance accounts for the increased number of positive detections both for the blank sky and the active galaxies, then the magnitude of the variance should help us decide if any detected variability is real or not. In Figure 5.3 (bottom) we have plotted a histogram of the standard deviation σ_B in the background count rate B normalized by dividing by B for a ~ 90 minute bin size. The white areas represent upper limits, and the shaded boxes correspond to observed values. We have computed the excess variance for the entire set of observations by adding together the excess variance from each observation. For the 90 minute bin size this gave σ_B/B of 0.7%, which is what one would expect if most of the excess noise was due to background fluctuations only. Thus the observed distribution is consistent with the expected excess variance being due to "confusion noise."

For observations of active galaxies we expect a slightly different distribution. First, when the detector is pointed at an active galaxy, the count rate is higher (by definition). This means that our sensitivity to

non-source-related variance is smaller during observations of active galaxies. This is shown by the fact that the distribution of upper limits has moved to the right (Fig. 5.3, top). Since the flux from active galaxies was first area corrected for effective exposure, to convert to σ_I/B we multiplied σ_I/I by S/B , where S is the source count rate (source flux times mean area). This means we have effectively ignored corrections due to changing area as the detector passes over the source.

Based on the results of Figure 5.3, we divide the sources into three groups: (1) those with $\sigma_I/B > 2\%$, (2) those with $1.5\% \lesssim \sigma_I/B < 2\%$, and (3) those with $\sigma_I/B \lesssim 1.5\%$. Sky fluctuations cannot account for the variability seen for the three sources in group 2, whereas any variability seen in group 3 can be totally due to sky noise. Sources in group 2 are suspect and need further checks. In the next section we will consider the sources in groups 1 and 2 in greater detail.

5.3 Light Curves

The most variable source was NGC 6814 (Fig. 5.4). This source is highly variable and shows a factor of 2 changes in flux on all time scales down to a few minutes (see Chapter 6). Table 5.1 shows that σ_I/I is near 43% for all the bin sizes considered up to 90 minutes. Using the published light curve from the Einstein Observatory Imaging Proportional Counter (IPC) observation of NGC 6814 (Tananbaum 1980), we find that $\sigma_I/I \sim 21\%$ for a 3 hr bin size. This could indicate either that the dominant source of variance has a time scale of hours or that amplitude of variability decreased, perhaps because of a decrease in flux between the HEAO-1 A2 and the IPC observations.

In Figure 5.5 we illustrate the difficulties in determining the time scale for a poorly sampled observation. The light curve is for our most

variable observation of NGC 4151. In the top panel we fit all six points to a straight line and calculate a χ^2 of 11.12 for 4 degrees of freedom (dof), which is an unacceptable fit to the data. (This compares with $\chi^2 = 39.80$ for 5 dof calculated assuming the source was constant.) In the second panel we have tried a model of a step function. For this case $\chi^2 = 5.39$ for 4 dof, which is acceptable. Although it appears (to the eye at least) that the transition occurred over the three bins nearest our location of the step, we point out that a small systematic deviation lasting 45 minutes could easily be introduced by a spacecraft orbital effect. In the third panel we have again fitted a straight line to the data but in this case have thrown out the first point. For the third case $\chi^2 = 4.76$ for 3 dof. If the source continued to brighten at the rate indicated in the third panel, then it would double its intensity in 12 hr. Thus statistically we cannot distinguish between a 12% flux increase on a time scale of 15 minutes or the start of a 12 hr flare. We prefer the latter interpretation since it is consistent with previous observations of variability from NGC 4151 (Mushotzky, Holt, and Serlemitsos 1978; Lawrence 1980). This ambiguity as to the correct model is not resolved as one goes to shorter bin sizes, for this case at least, since the smaller bin size generates no new information.

The third most variable source is Cen A (Fig. 5.4). We note that HEAO-1 scanning data for Cen A show it to be slightly extended, presumably due to weak nearby sources. Marshall and Clark (1981) have reported a nearby source which will appear in our field of view. This source confusion can explain most of the observed variability. Notice that there is no indication of a linear change over the 12 hr observation.

We will now consider the sources with only weak evidence for

intrinsic changes. First, consider the light curve for H1649-595 in Figure 5.4 (H1649-595 was tentatively identified with NGC 6221 by Marshall et al. 1979). This light curve clearly shows that most of the excess variance is due to short-duration "flares" near the end of the observation. For this source the three high points are due to a bright confusing source. Figure 5.6, a contour plot of the X-ray sky around H1649-595, clearly shows the confusing source. The source "flared" only when the detector was looking at the region of the sky near this source. We have included H1649-595 in our sample as a warning that "statistically real" variability could have many causes.

Although H1649-595 had a true source of excess variance, it was only weakly detected as variable by the $\sigma_1/1$ test. This was due to most of the variability being due to flares and, as was mentioned in chapter 2, looking at the excess variance is not the most sensitive method to search for single bin flares. Since all sources were examined by eye with a 300 sec bin size, I can report that there was no evidence for a single bin flares on that time scale. Let us now consider shorter bin sizes. A typical observation consisted of ~ 1000 , 5.12 sec intervals. Table 2.1 shows that a single bin flare would have had to exceed 7.6σ , where σ is the statistical uncertainty, before it would have been detected more than 50% of the time. If the flare size was less than 7.6σ then there is a good chance we would have missed the event. For a typical source rate of 3 ct/sec and a background of 14 ct/sec, a 7.6σ fluctuation would correspond to a factor of 4.6 increase in the source flux. Simple Gaussian statistics show that 90% of the time all 1000 bins would have statistical fluctuations of 4.0σ or less. For our typical source a 4.0σ increase corresponds to a factor of 2.4 rate increase.

Now consider what happens if the bin size is doubled. A 7.6σ excess in a 5.12 sec bin would only correspond to a 5.4σ excess in a 10.24 sec bin. The corresponding value of X , given by (2.4.1), would drop from 1.3 to 0.92. Since both numbers were calculated for the same observation, we find that the interesting parameter is the change in X (or the excess variance) as shorter bin sizes are considered. Since I have examined the X value for bin sizes down to 5.12 sec I can report that there is no strong evidence for an increase at short bin sizes. Thus rare 7.6σ events may have been missed by the excess variance method; however, the lack of any increase in the excess variance as shorter bin sizes are considered indicate that nothing interesting was missed.

Both NGC 3227 and MCG-5-23-16 showed evidence for a linear increase in flux. If such a rate increase continued, then the source flux would double in 10 hr for NGC 3227 and 28 hr for MCG-5-23-16.

Finally, we come to the MCG 8-11-11 observation shown in the center panel of Figure 5.4. In this figure we see small peaks near 2.1, 3.9, and 5.5 hr. Since these points are ~ 1.5 hr apart, i.e., one spacecraft orbit, we suspect that these are not real events. A σ_1/B of $\sim 1.6\%$ confirms that the variability seen can be due to confusion noise. If one ignores the short-term variability, then a weak linear increase is seen which will double the source flux in a few days. We are unable to judge the reality of such a trend.

It is interesting to note that all the variable objects in our sample, NGC 3227, NGC 4151, NGC 6814, and MCG-5-23-16, are low-luminosity objects with $L_x < 3 \times 10^{43}$ erg/sec. This agrees with the HEAO-1 longer time scale data which show that lower luminosity sources have a greater probability of being variable. In addition, with the exception of

NGC 6814, the observed variability is consistent with a time scale of ~ 1 day. This result agrees with the Ariel 5 observation (Marshall, Warwick, and Pounds 1981) that many sources show a 1 day time scale.

Variability on longer time scales will be reported by Mushotzky (1983). However, we can compare the count rates for different pointed observations of the same source to obtain some information about longer time scales. We find that Cen A and NGC 4151 show large changes over 6 months. Mrk 509, observed four times in 2 weeks, shows a large-amplitude change. This was reported by Dower et al. (1980) using the HEAO-1 A3 data. Our data for days 657-666 show that the time required for $\Delta L = \langle L \rangle$ is 22 days. Thus we confirm the general nature of the variability reported by Dower et al. but indicate a slightly longer time scale.

5.4 Implications of Rapid Non-Variability

The previous results indicate that X-ray emission from active galaxies rarely varies on a time scale of less than one day. In this section I will consider the implications of this non-variability. The next chapter is devoted to a discussion of the rapid variability of NGC 6814 and the implications of that observation. Finally, in Chapter 7, I try to reconcile NGC 6814 with the general lack of variability.

A possible reason for a lack of variability is for the source of the X-ray emission to be very stable. In X-ray astronomy stability appears to be an exception. Galactic X-ray sources (associated with accretion) are known to be highly variable. However, active galaxies are variable on longer time scales and of course NGC 6814 varies on short time scales. Therefore, if the lack of variability is due to a stable accretion flow then one is forced to explain the reason for this stability. The problem is not solved but forced one level deeper.

The alternate explanation is to argue that the shortest time scale observed is directly related to light travel time across the source region. This lack of variability on time scales of less than one day indicates that the X-ray plasma is about 1 lt-day across. In the black hole accretion picture there are two ways to create a large X-ray region. Either the black hole is extremely large or the X-rays are produced far from the Schwarzschild radius.

If the X-rays come from a region only ~ 10 gravitational radii from the central object and if the general lack of variability on time scales of less than 1 day tells us anything about the size of the region, then the central object must have a mass of $10^9 M_{\odot}$ or greater. Pounds (1979) speculated, based on the apparent ubiquity of variability with a 1 day time scale, that all active galaxies contained a $10^9 M_{\odot}$ central object. The Eddington limit for such an object is 10^{47} ergs/sec, which is much greater than the luminosity of any object in our sample. Of course, if most active galaxies contain a $10^9 M_{\odot}$ object, then one is forced to explain why NGC 6814 is so small. It is possible that most active galaxies contain dead quasars (Lynden-Bell 1969), whereas objects like NGC 6814 might never have gone through a "quasar-like" phase.

If the X-ray plasma is not confined to the central object, then it could fill a large volume of space. In this picture electrons are heated via some unknown mechanism, perhaps in a small volume, and then proceed to fill a volume of space about 1 lt-day across. This may occur in a two-temperature disk model (Shapiro, Lightman, and Eardley 1976). Since the virial temperature of the protons is much higher than the corresponding electron temperature, an accretion disk can have two temperatures. If the electrons are not effectively cooled, then interactions with protons can

heat them to temperatures greatly exceeding their virial temperatures. Lightman (1982), considering the possibility of relativistic electron plasmas, listed several nongravitational ways to confine the electrons. Since it is notoriously difficult to confine plasmas via electromagnetic forces, it is entirely possible that the central object is boiling off some matter. Thus the X-ray emission can come from two components, the region near the black hole and the extended volume.

FIGURE CAPTIONS

Figure 5.1 -- The excess noise, σ_I/I , is plotted vs. source flux for ~ 5 minute bin size. The curved line is an estimate of the noise introduced by source confusion (see text). The solid dots are positive detections of source variance and the bars represent upper limits.

Figure 5.2 -- Same as Figure 5.1 except now the bins are about one spacecraft orbit long.

Figure 5.3 (top) -- A histogram of σ_I divided by the background rate for our observations of active galaxies. The shaded regions represent positive detections of variability, whereas the white areas above the shaded regions represent the 90% confidence upper limit for the nonvariable objects. (bottom) -- Same as top except in this case no HEAO-1 sources were in the field of view.

Figure 5.4 -- A sample of nine of our X-ray light curves. The top six represent the more variable objects in our sample, whereas the bottom three represent typical light curves. In all cases a 20 minute bin size was used to construct the light curves. In the upper left of each panel the first number is σ_I/I , and the number in parentheses is σ_I/B . Both σ_I/I and σ_I/B are constructed for the bin size in the plot. The best fitting linear trend is indicated by a solid line for MCG-5-23-16 and NGC 3227.

Figure 5.5 -- The most variable observation of NGC 4151 has been fitted to three models: (top) a straight line through all the points, (middle) a step function, and (bottom) a straight line through the last five points.

Figure 5.6 -- The region of X-ray sky around H1649-595. (top) Contours are every 10 ct/sec with the lowest level at 10 ct/sec. (bottom) Contours are plotted every .5 ct/sec with the highest level at 10 ct/sec. For both figures the data has been smoothed to reduce the statistical noise. H1649-595 only appears in the bottom plot and is at the center of the panel.

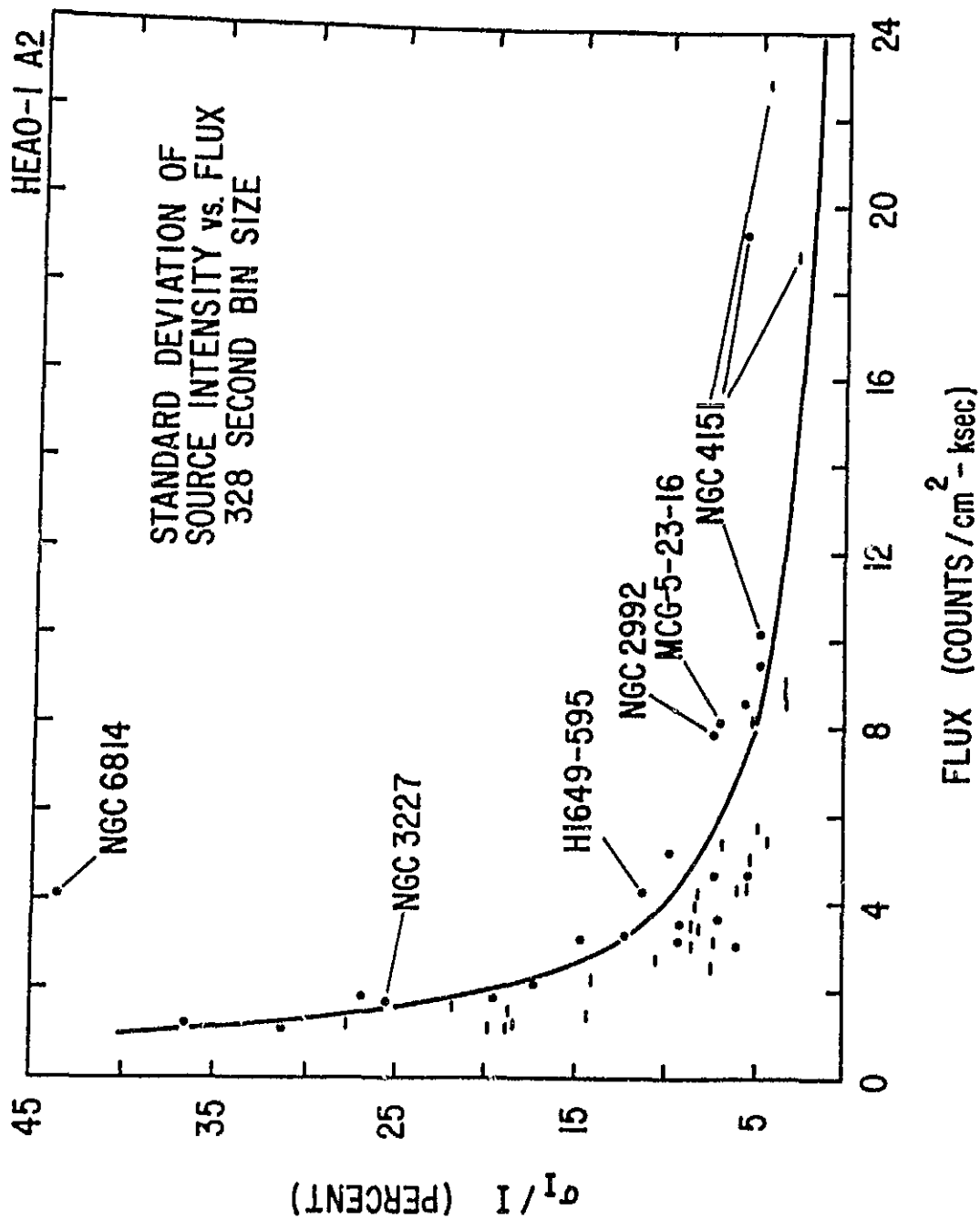


Figure 5.1

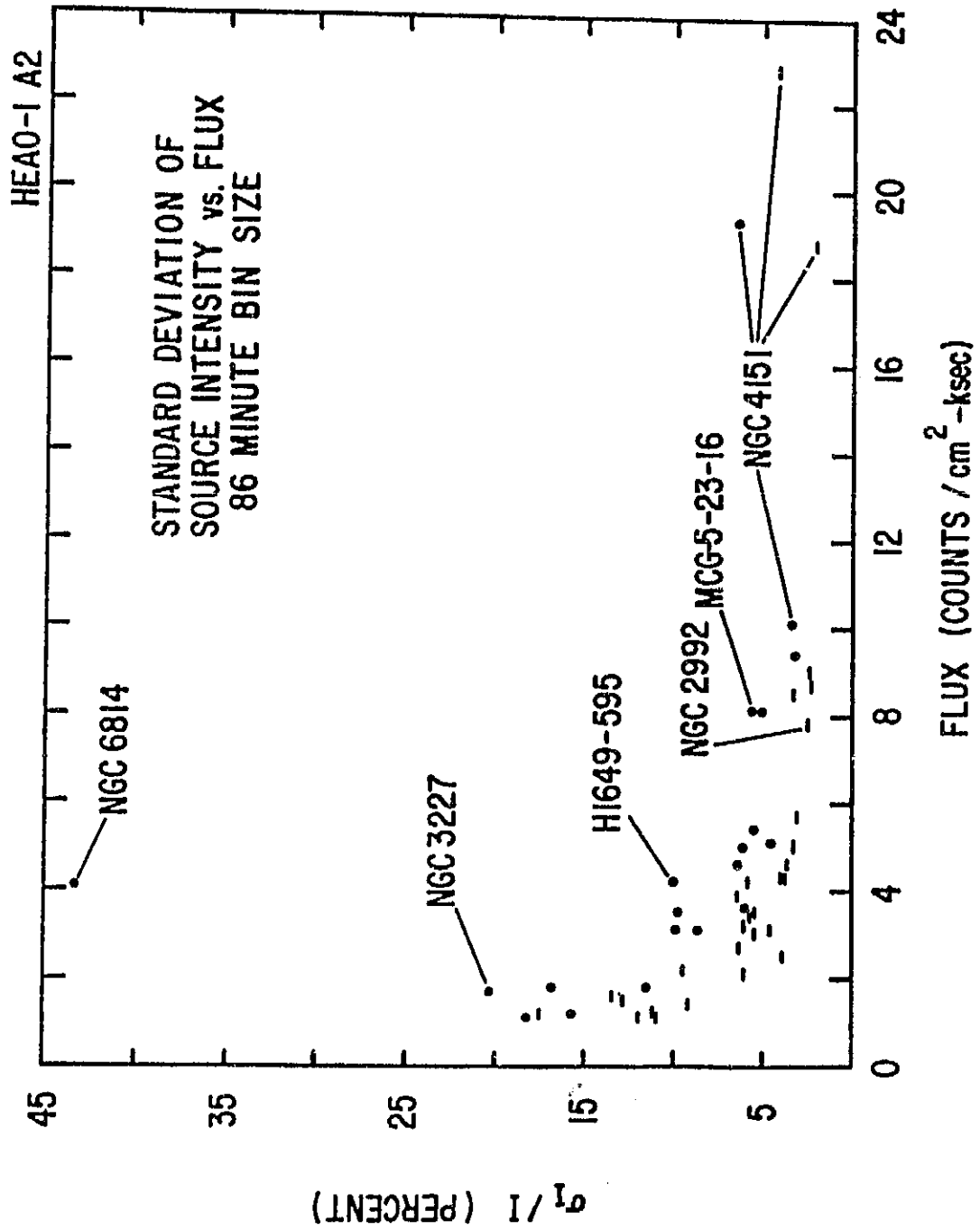


Figure 5.2

ORIGINAL PAGE IS
OF POOR QUALITY

HISTOGRAMS OF VARIABILITY

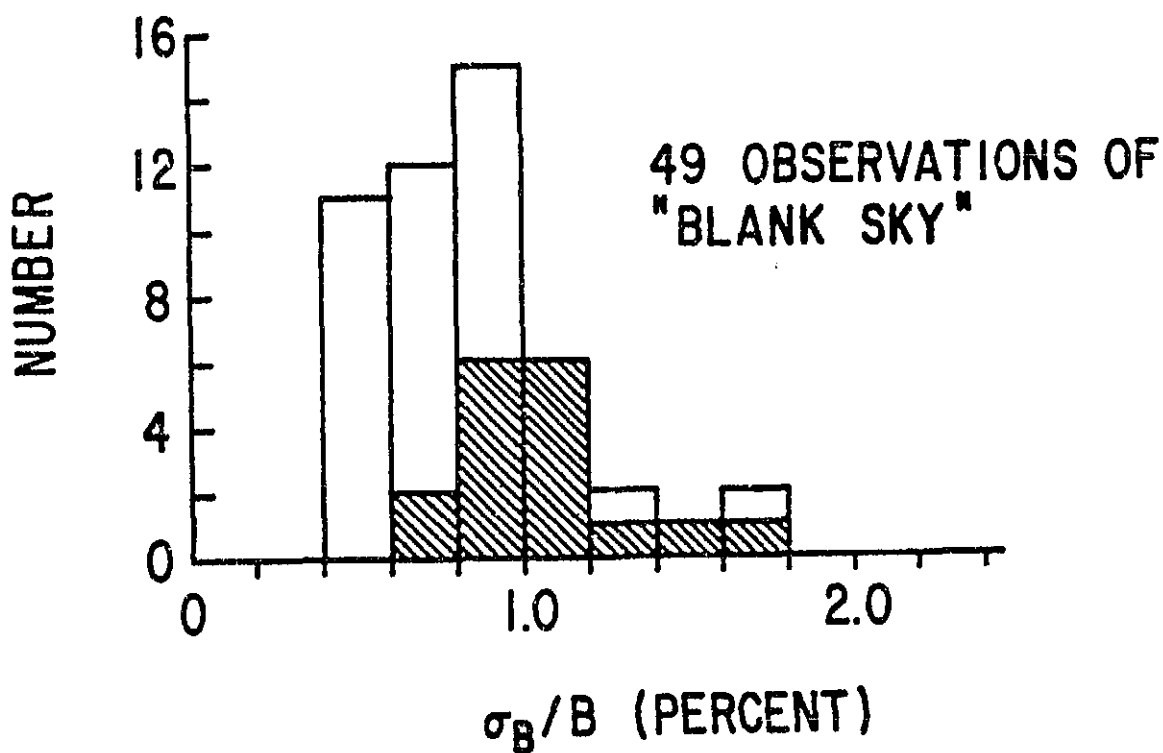
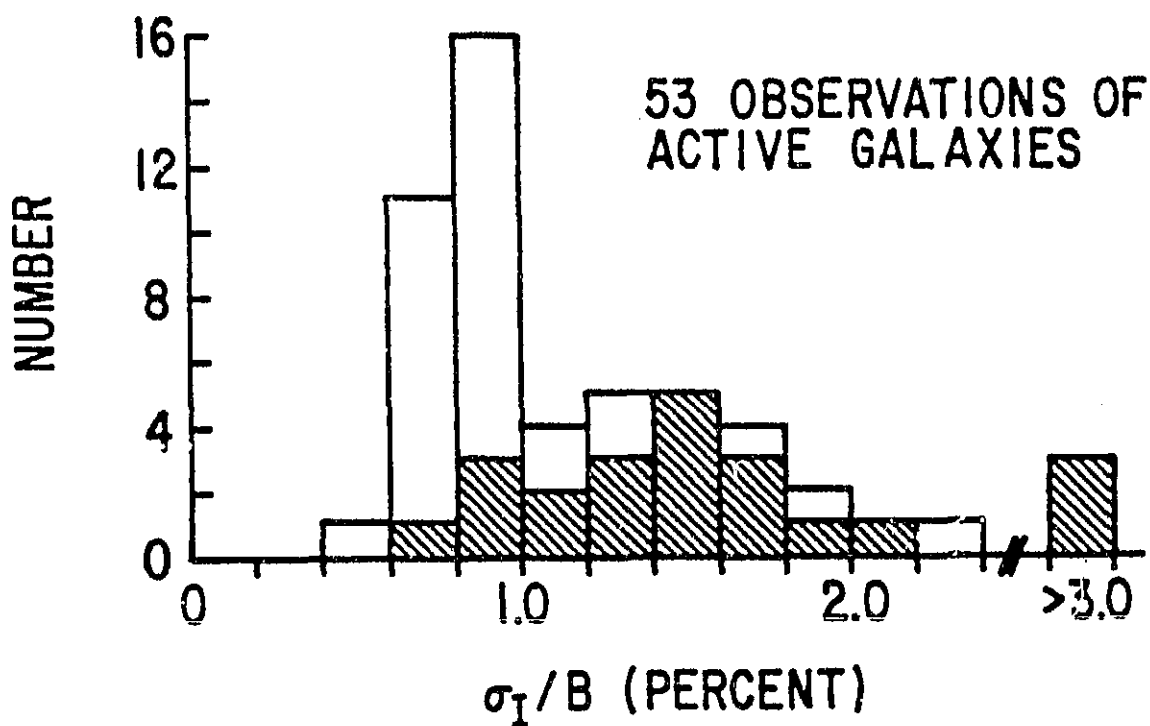


Figure 5.3

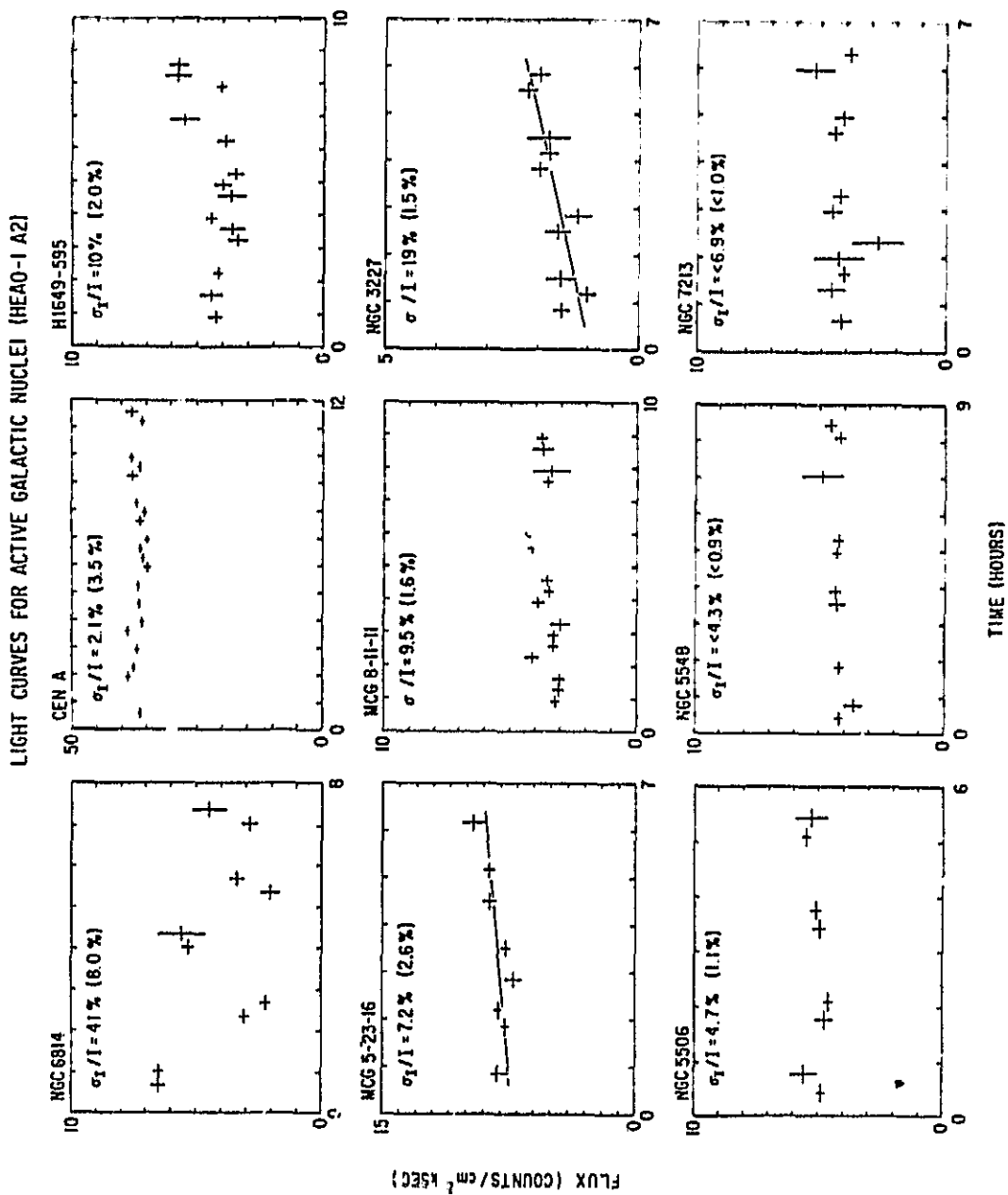


Figure 5.4

ORIGINAL PAGE IS
OF POOR QUALITY.

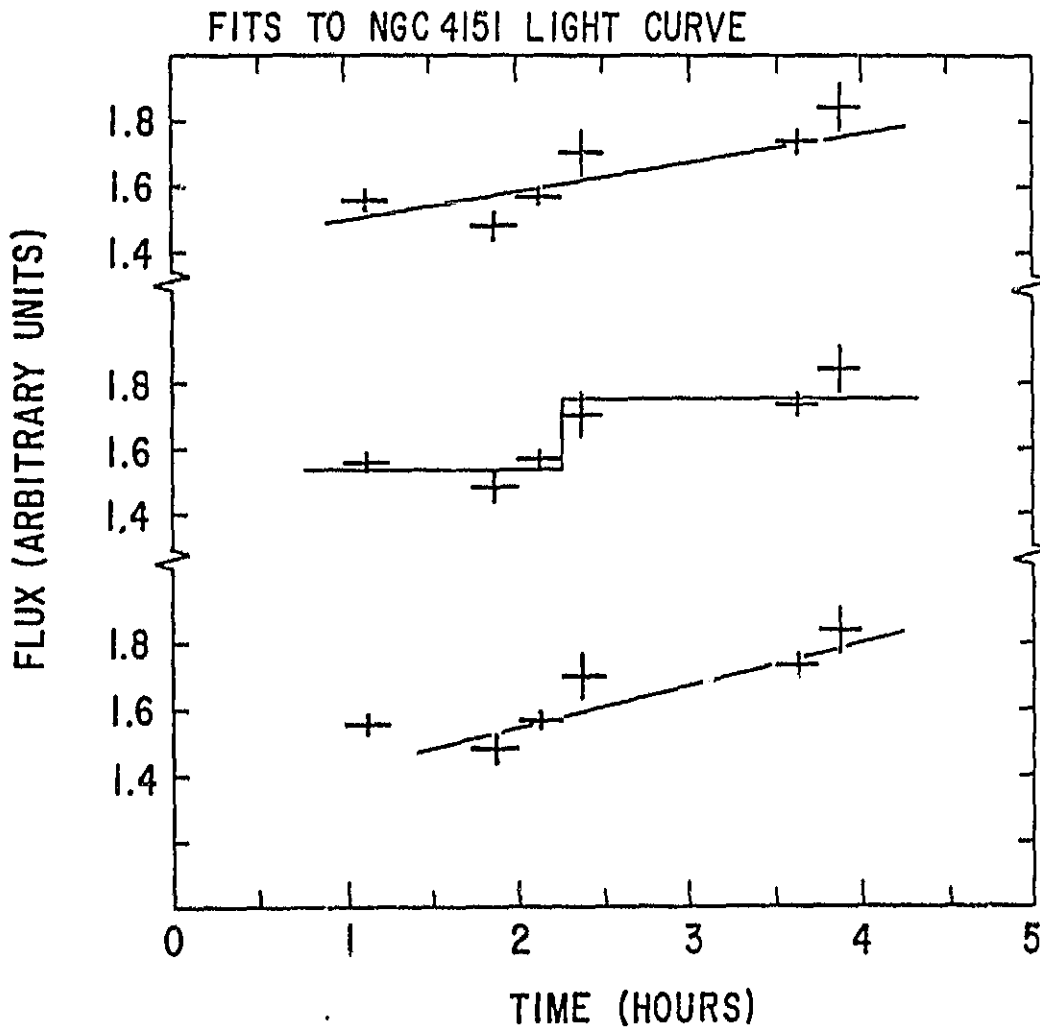
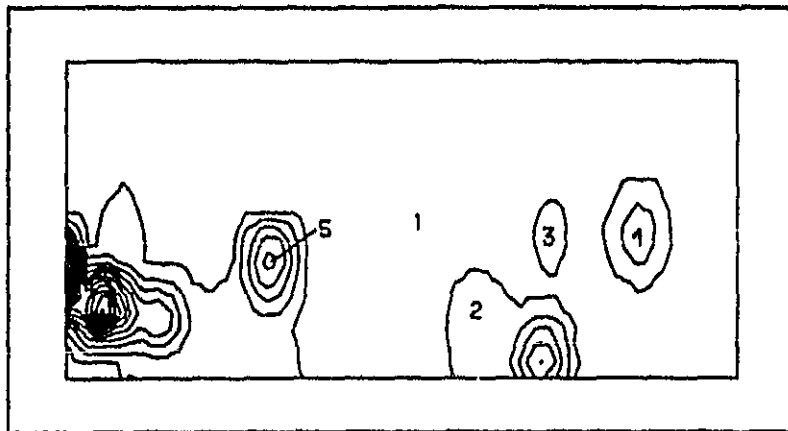


Figure 5.5

ORIGINAL FRAME IN
OF POOR QUALITY



X-ray Sources

- | | | | |
|---|------------|---|------------|
| 1 | 4U1640-595 | 4 | 2S1627-673 |
| 2 | 4U1556-605 | 5 | 4U1630-47 |
| 3 | 4U1631-64 | | |

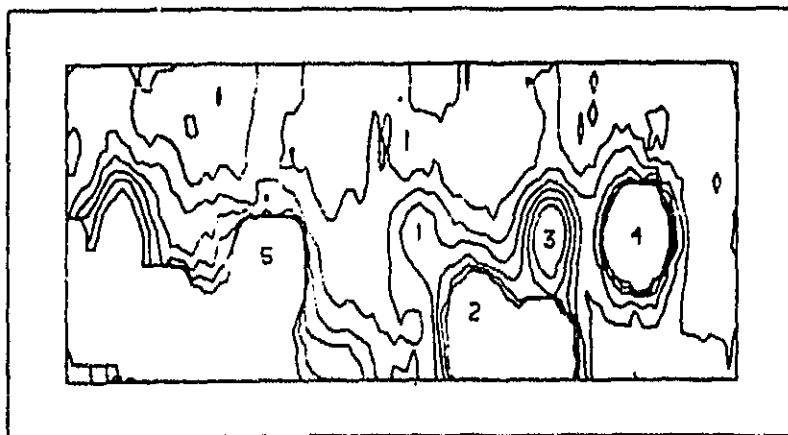


Figure 5.6

6. RAPID VARIABILITY OF NGC 6814

6.1 Chapter Overview

Material in this chapter first appeared in Tennant et al. 1981. First it is established that the X-ray flux from NGC 6814 varies by a factor of 2.5 on a timescale of 90 min. This result by itself is one of the strongest pieces of evidence for short term extragalactic variability reported. The fact that the mean for an entire orbit varied indicates that it is unlikely that near Earth effects could cause the signal. By examining shorter time scales we see evidence for large changes on time scales as short as 100 sec. Extensive tests for spectral changes showed no obvious indications of a change in the shape of the spectrum. Finally, the rapid variability observed from NGC 6814 is used to constrain various models for the X-ray emission from this source.

6.2 Variability on Long Time Scales

Examination of Figure 6.1 shows that the flux from NGC 6814 is strongly variable. On an orbit-by-orbit (1.5 hr) basis, the flux varies by a factor of ~ 2.5 (Table 6.1). In Table 6.1 we also show the χ^2 calculated on the assumption that the source was constant during each individual orbit. For all but one of these orbits, the value of χ^2 allows us to reject the hypothesis of source constancy on time scales less than 1.5 hr at $> 99.99\%$ confidence. This is clearly shown in Figures 6.2 and 6.3 in which a prominent flux changes on a time scales of less than 500 sec are evident.

Having established source variability on time scales less than 1.5 hr, we now attempt to characterize the nature and time scale of this variability.

TABLE 6.1

NGC 6814

Orbit	Mean Flux mcts/cm ² -sec	χ^2 (82sec bins)	Degrees of Freedom
1	5.6	279.6	21
2	2.1	67.9	23
3	4.8	77.2	11
4	2.5	12.3	9
5	2.9	35.9	6

6.3 Short Time Scales

The auto-correlation function (ACF) was computed for the first and second orbits using a 10.24 sec bin size. In Section 3.4 we discuss how the ACF was generated and how errors in the reported time scales were determined. The inferred characteristic time scale of the source intensity and the errors are given in Table 6.2 for these orbits and the entire data stream. All the data are consistent with a characteristic time of ~ 100 sec. There were insufficient data for orbits 3-5 for a meaningful auto-correlation function to be calculated separately. In Figure 6.4a we show the ACF for the complete data set (orbits 1-5 inclusive). The characteristic time for variability is the slope of the natural logarithm of the ACF (Figure 6.4b). We detrend the ACF by subtracting the orbital mean from each orbit's worth of data. The detrended ACF function and its

natural logarithm are shown in Figures 6.4c and 6.4d, respectively. The time scale of 200 sec seen when the data are "detrended" confirms that this is a characteristic time for the entire data set.

TABLE 6.2

AUTO-CORRELATION FUNCTION RESULTS

Orbits Used	Detrend	Time Scale (sec)
1	No	85^{+60}_{-25}
2	No	$230^{+\infty}_{-130}$
1-5	No	$248^{+\infty}_{-110}$
1-5	Yes	101^{+59}_{-26}

6.4 Limits On Spectral Variability

We have searched for spectral variability in four different ways: (1) We have computed the mean spectrum on an orbit-by-orbit basis. (2) We have sorted the data on the value of their flux and have computed a mean "hardness" ratio for each value of the flux. (3) We have computed the cross-correlation function between two energy bands. (4) We have looked for spectral variability during a given event. Each of these methods is most sensitive to different types of spectral change as discussed below.

6.4.1 Orbit-by-Orbit Variability

The best fit spectra on an orbit-by-orbit basis assuming a power law model with energy index α , norm $A \times 10^{-3}$ counts/sec, and equivalent column density of hydrogen in the line of sight N_H are shown in Table 6.3 (all errors are 1σ). These values are to be compared with the flux weighted average for the entire observation $\alpha = 0.73 \pm 0.22$, $N_H = 4.3^{+2.7}_{-2.0} \times 10^{22} \text{ cm}^{-2}$ (Mushotzky et al. 1980) (90% confidence error). The value of χ^2 computed on the assumption that α and N_H for each orbit is the same as the flux weighted mean is 6.8 for ten parameters of interest. This indicates that, despite a factor of 2 change in intensity on a time scale of 1.5 hr, the time averaged spectrum did not vary significantly.

TABLE 6.3
NGC 6814 SPECTRAL FITS

Orbit	A	α	$N_H (\times 10^{22})$	χ^2
1	20.4	$0.67^{+0.23}_{-0.21}$	$5.4^{+3.2}_{-2.2}$	1.5
2	7.2	$0.66^{+0.46}_{-0.35}$	$2.5^{+3.8}_{-2.5}$	4.8
3	7.7	$0.35^{+0.23}_{-0.21}$	$2.5^{+2.5}_{-2.3}$	14.0
4	5.7	$0.55^{+0.51}_{-0.07}$	$0^{+3.6}$	7.7
5	6.0	$0.58^{+0.52}_{-0.10}$	$0^{+3.8}$	5.3

Note--5 degrees of freedom

C - 2

If we assume that N_H did not vary during this observation (consistent with the values in Table 6.3) and fix N_H at the value derived for the entire observation, the formal error in α decreases. In Table 6.4 we show the best fit values of α for each orbit under this assumption. There is a slight indication that the source spectrum is marginally flatter when the flux is higher. In Figure 6.5 we plot α versus the 2-20'keV flux on an orbit-by-orbit basis and find that a linear relation of the form $\alpha = mF + b$ (where F is the flux) gives an acceptable fit with $m = -0.054^{+0.022}_{-0.032}$. This trend is significant at only 2.5σ , however. Alternatively, we place a 3σ upper bound of $\Delta\alpha < 0.37$ on an orbit-by-orbit basis.

TABLE 6.4
NGC 6814 SPECTRAL FITS

Orbit	A	α
1	16.5	$0.59^{+0.07}_{-0.07}$
2	11.2	$0.87^{+0.19}_{-0.16}$
3	11.1	$0.49^{+0.10}_{-0.09}$
4	18.9	$1.06^{+0.24}_{-0.21}$
5	20.4	$1.07^{+0.27}_{-0.22}$

Note - Absorption fixed at 4.3×10^{22}

6.4.2 Limits on Spectral-Intensity Correlation

We have accumulated data at $E > 6$ keV (E_{High}) and $E < 6$ keV (E_{Low}) on an 82 sec basis. We then sorted the data into 10 intensity bins on the basis of E_{Low} . In Figure 6.6 we plot the average of E_{High} whenever E_{Low} was within the prechosen bin limits, along with lines which correspond to power law spectra of slopes $\alpha = 2.0, 1.75,$ and 1.50 with N_{H} fixed at $4.3 \times 10^{22} \text{ cm}^{-2}$. The data are all consistent with the $\alpha = 1.75$ line. We note that each point in Figure 6.6 represents an independent measure of the power law index. We conclude that there is no intensity related spectral variability with an upper limit on a change in spectral index of $\Delta\alpha < 0.30$. (This method of analysis could hide possible variability if the same intensity state has different spectral indices and if these values scatter about a given mean value which is also characteristic of the total time averaged spectrum.)

6.4.3 Spectral Cross-Correlations

A defect of the prior two methods is the relatively large bin sizes (30 minutes and 82 seconds), necessitated by the relatively low flux, compared to the characteristic variability time of ~ 100 sec. The cross-correlation function allows one to test the entire data stream on shorter time scales to see whether the softer photons systematically lead or lag the hard ones. We report here the result of two cross-correlation analyses, one designed to minimize the detectable time scale, and the other to maximize the difference between the selected energy bands.

Cross correlation of the total flux from the argon detector, MED (which is sensitive to photons with a mean energy of $E = 5.46$ keV for the NGC 6814 spectrum) with the total flux from the xenon detector, HED 3, ($E =$

8.67 keV) shows that the MED leads HED 3 by 6.3 ± 3.3 sec for a bin size of 15.3 sec. We also cross-correlated photons of energy < 6 keV ($\bar{E} = 5.17$ keV) with photons of energy > 6 keV ($\bar{E} = 12.50$ keV) in the HED3 detector. For this analysis we used a bin size of 41 sec, since this made the errors due to Poisson noise similar to those in the MED versus HED 3 analysis. We found that the < 6 keV photons lead the harder photons by -4.1 ± 9.6 sec.

6.4.4 Spectral Variability of a Resolved Event

The flux change shown in Figure 6.2 has sufficient statistics to examine spectral variability within a given event. As can be seen in the middle panel, the effective spectral index α did not change ($\Delta\alpha \leq 0.30$) during this event despite the fivefold change in source flux. These data also rule out variation in X-ray column as the origin of the short term variability. Due to the low flux, the hardness ratios are binned in 82 sec bins, and thus we cannot comment on spectral variability on the shorter time scale indicated in the previous section. We conclude that, for this one event, spectral variability does not occur on the characteristic time of intensity variability.

6.5 Implications of Rapid Variability

The rapid variability observed in NGC 6814 can place strong constraints on the physical processes producing the X-ray flux and the environment in which it is produced. With respect to the NGC 6814 data, we shall discuss general constraints and limits we can place on "standard" X-ray emission mechanisms.

6.5.1 General Considerations

The average luminosity of NGC 6814 is $5 \times 10^{42} h^{-2}$ ergs/sec in the 2-20 keV band, here h is Hubble's constant measured in units of 75 km/sec-Mpc. Since the amplitude of the variability is quite large, we will

assume that the change in luminosity is greater than 5×10^{42} ergs/sec. If the X-ray spectrum extends out to ~ 500 keV, as does the X-ray emission from Cen A (Baity et al. 1981), then the average luminosity is $\sim 2.1 \times 10^{43} h^{-2}$ ergs/sec.

If NGC 6814 is powered by accretion onto a single compact object, then we can set a firm upper limit on the mass of this object by requiring that the fluctuation time be longer than the light travel time across the Schwarzschild radius. This gives

$$M \lesssim \frac{c^3 \Delta\tau}{2G} \approx 1 \times 10^7 M_{\odot} \quad (6.5.1)$$

for $\Delta\tau = 100$ sec. On the other hand, we find that

$$M > 9 \times 10^4 M_{\odot}/h^2 \quad (6.5.2)$$

by requiring that the luminosity not exceed the Eddington limit. Without a detailed model, we cannot restrict the mass range any further. As we will see, though, a $10^6 M_{\odot}$ object is consistent with thermal Compton models.

Using the Fabian and Rees (1979) relation given in section 1.4 with $\Delta L > 5 \times 10^{42}$ ergs/sec and $\Delta\tau_{\min} \sim 100$ sec, we find that $\eta > 3\% h^{-2}$. However, if the variations extend out to 500 keV, then $\eta \sim 13\% h^{-2}$. If one requires $\eta < 10\%$, then $h > 1.1$. Conversely, if $h < 1$ then one must consider models that allow high efficiencies (Thorne 1974) or argue that one of the assumptions used in deriving the Fabian and Rees (1979) relation is violated. This could imply directed motion of either the matter or the radiation.

If the assumptions in the Fabian and Rees relation are in effect, we

can deduce two properties of the source. One condition for a minimum time scale is that the optical depth (due to electron scattering) is near unity. This condition tells us that a thermal-Compton model (see section 6.5.4) may work. A second condition is that the electrons rapidly radiate all their energy. Since NGC 6814 can stay at a high level for a long (~ 1000 sec) time, the electron population must be resupplied with energy. When matter falls into a gravitational potential protons gain more energy than the electrons. Thus the electrons can gain energy via collisions with the protons. It is also possible for some of the proton's energy to go into an electromagnetic field (via an accretion disk dynamo for example). In this case the created electric field would accelerate the electrons. No matter how the energy is supplied it is clear that if the supply is sporadic then the X-ray emission will be variable.

6.5.2 Synchrotron Radiation and Synchrotron Self-Compton Emission

If the X-ray flux is produced by relativistic particles in a "steady state" type process via synchrotron emission, or synchrotron self-Compton (SSC) emission, then one requires that the particles "live" long enough to fill the emitting region.

The lifetime of a relativistic electron against Compton losses is $\tau_c \approx 3 \times 10^7 \text{ sec}/\gamma u$, where the energy of the electron is $\gamma m_e c^2$ and u is the energy density of the photon field. For $L \sim 5 \times 10^{42}$ erg/sec and a size $R \sim c\Delta t \sim 100$ lt-sec, $u \sim 2 \times 10^6$ ergs/cm³. This gives $\tau_c \sim (7/\gamma)$ sec which is a factor of 10 shorter than the light travel time across the region for all values of γ . We conclude that synchrotron and SSC models, without continual injection and/or reacceleration and/or relativistic bulk motion, cannot work.

Cavaliere and Morrison (1980) have considered a model in which the

particles are continually reaccelerated and in which the radiation rate is controlled by the acceleration rate. Their model, for the parameters measured in this paper, implies electron densities $n_e \sim 1 \times 10^9$ and B fields ~ 20 gauss for the case in which the X-rays are primarily due to Compton interactions and the optical photons are due to synchrotron radiation, a rather higher value for n_e and a lower value of B than Cavaliere and Morrison found for NGC 4151 or 3C 273.

6.5.3 Thermal Bremsstrahlung and Blackbody Radiation

The luminosity from an optically thin sphere emitting X-rays due to thermal bremsstrahlung at a temperature T , is

$$L \sim 2.4 \times 10^{-27} T^{1/2} n_e^2 V \text{ ergs/sec,} \quad (6.5.3)$$

where V is the volume of the source region and n_e is the electron density. For $T \gtrsim 10^8$ K (as required by the spectral fits [Mushotzky et al. 1980]), one requires $n_e \sim 1 \times 10^{14} \text{ cm}^{-3}$ for $V \sim 1 \times 10^{38} \text{ cm}^3$. This gives an optical depth to Thompson scattering $\tau \sim n_e \sigma \lambda \sim 200$. Therefore our initial assumption of optically thin emission cannot be correct, and the output spectrum must be optically thick in shape if the X-rays originate in a sphere of hot gas. However, the X-ray spectrum does not have this shape; therefore, we conclude that the X-ray emission, without Compton amplification, cannot be purely thermal in character.

6.5.4 Thermal-Compton Models

Although simple accretion with thermal emission can explain the source of power, we need a more exotic emission mechanism to be consistent with both the spectrum and the rapid variability. Another X-ray source that shows rapid time variations in addition to a power law X-ray spectrum

is Cyg X-1. We will now consider models originally constructed to explain Cyg X-1 but scaled up to $L = 10^{43}$ ergs/sec.

The more successful models have involved unsaturated Comptonization. For this mechanism to function the source must consist of a cloud of hot electrons, at a temperature of kT_e , with an optical depth to electron scattering τ_{es} less than a few and a copious source of soft "seed" photons. Under these conditions, soft photons entering the cloud can be up-scattered, in energy, to X-rays but do not spend enough time in the cloud to come into thermal equilibrium with the electrons. Shapiro, Lightman, and Eardley (1976) and Katz (1976) showed that the resultant spectrum is a power law for energies below kT_e with an exponential falloff at higher energies. Pozdynakov, Sobol, and Sunyaev (1979) and Takahara (1980) found qualitatively similar results in Monte Carlo calculations for a wide range of temperatures and optical depths. The location of the rollover is somewhat model dependent with the result from Shapiro, Lightman, and Eardley (1976) occurring at the lowest temperatures. However, all of the calculated spectra rollover significantly by $3 kT_e$. There is no evidence for either a rollover or a Wien peak in the spectrum of NGC 6814 or of any other active galaxy where spectra have been measured to higher energies. This implies that $kT_e > 15$ keV in NGC 6814. Since Cen A, the source with the best determined spectrum, has a power law out to ~ 500 keV (Baity et al. 1981), it is possible that $kT_e \gtrsim 300$ keV.

For unsaturated Compton models, τ_{es} and kT_e are related by

$$\tau_{es} = \left(\frac{650 \text{ keV}}{kT_e} \right)^{1/2} - \frac{2}{3} \quad (6.5.4)$$

(Sunyaev and Titarchuk 1980), for $\alpha = 0.7$ as measured for NGC 6814. Using

the above we compute that $\tau_{es} = 4.0, 1.9,$ and 0.8 for electron temperatures of $30, 100,$ and 300 keV. Notice that although kT_e ranges over a factor of 10 , the product $(\tau_{es} \times kT_e)$ only changes by a factor of 2 . This will be useful below.

In any mechanism involving inverse Compton scattering, the harder photons are on the average scattered more times than the softer photons. Lightman, Giacconi, and Tananbaum (1978) pointed out that since the harder photons are scattered on the average more times, they spend more time in the source and so tend to lag the soft during fluctuations. Lightman, Giacconi, and Tananbaum (1978) suggested that the rise time of a flare t_m , measured at energy E , should be given by

$$t_m = t_R A \ln (E/E_S) \quad (6.5.5)$$

where $t_R = R/c$ (size of source region), A is a constant on the order of unity, and E_S is the energy of the original soft photons. More detailed calculations (Payne 1980; Lightman and Rybicki 1979) have shown that

$$A = \frac{m_e c^2}{\tau k T_e (3 + 2\alpha)}, \quad (6.5.6)$$

where $\tau = N\sigma_T R$ and α is the power law index of the persistent source. Since $\tau \times kT_e$ appears as a product, we can easily estimate A to within a factor of 2 . If we use $kT_e \sim 100$ keV, we find $A \sim 0.6$.

In (6.5.5), t_m is unobservable since it is measured from the (unobserved) injection time of the original soft photons. We set $t_m = (1 + f) t_0$, where t_0 is the observed rise time of the flare and f is model dependent but only a slowly varying function of E_S . Solving for t_R gives

$$t_R = \frac{(1 + f)t_0}{0.6 \ln(E/E_S)} \quad (6.5.7)$$

Before we can go on, we must estimate E_S . Lightman et al. (1978) suggested measuring the rise time of a flare in two energy windows and then determining the ratio of rise times:

$$D = \frac{t_{m1}}{t_{m2}} = \frac{\ln(E_1/E_S)}{\ln(E_2/E_S)} \quad (6.5.8)$$

Solving for E_S one finds that, for $E_S < 0.1$ keV, E_S is proportional to E_1 and E_2 raised to large powers. Thus a small error (1%) in D can result in a factor of 10 uncertainty in E_S . In addition, (6.5.8) is only approximate, since it uses t_m instead of the observable time t_0 . An observational problem is that the statistics usually are not good enough to determine two different rise times in two narrow windows. Thus, we are unable to determine E_S accurately, but estimating this number will not result in too large an error in t_R .

Since Seyfert galaxies are known to be strong IR sources (Rieke 1978), we choose $E_S = 1$ eV. This is consistent with the hypothesis of the soft seed photons originating in a large accretion disk which should be rather cool. We define t_0 as the time for the intensity to go from $0.37 I_{\max}$ to I_{\max} . With $\log(E/E_S) = 3.8$, we find $f \sim 2$ using the function given by Payne (1980). Thus

$$t_R \sim 60 \text{ sec}, \quad (6.5.9)$$

which says that the size of the source region is slightly smaller than the

variation time. If we assume the peak flux comes from ~ 5 Schwarzschild radii, then we estimate the mass of the compact object as

$$m \approx \frac{c^3 60 \text{ sec}}{10G} = 1 \times 10^6 M_{\odot}. \quad (6.5.10)$$

If the geometry is canonical Kerr, then the peak X-ray flux comes from 0.8 Schwarzschild radii (Thorne 1974). For this case $M \sim 8 \times 10^6 M_{\odot}$.

Although it has been impossible to measure D and thus check the consistency of the unsaturated Compton model, another test can be made. Photons at $E_2 (> E_1)$ should always lag photons at E_1 by an amount

$$\Delta t_m = t_{m2} - t_{m1} = A t_R \ln (E_2/E_1). \quad (6.5.11)$$

This equation is independent of the soft photon energy but is a function of the electron temperature. It is possible to measure Δt_m , using the cross-correlation function, for the entire data stream, not just during the rising portion of an event. Using $t_R = 60$ sec and $A = 0.6$, one predicts $\Delta t_m = 30$ and 17 sec for the < 6 keV versus > 6 keV and MED versus HED 3 data respectively. Recall from the observations in §6.4.3 that the measured times were -4 ± 10 sec and 6 ± 3 sec, respectively. Both of these values of the lag time are consistent with the observed lag time being one-third or less of the predicted value. One possibility is that t_R is smaller than our estimate of 60 sec (see below). Another point is that we are using rather broad energy windows which will "smear" the effect. Until we obtain more photons, allowing a smaller energy window, we cannot make any strong statements. However, the fact that the observed MED versus HED 3 delay is in the right direction is encouraging.

Both Payne (1980) and Lightman and Rybicki (1979) predict large (and so far unobserved) spectral changes during an intensity fluctuation. We note a few reasons that we might not see such changes. First, Lightman and Rybicki (1979) suggested that one may identify the observed time for variability with the time scale for a change in the soft photon flux rather than t_R . Equation (27) of Lightman and Rybicki (1979) is then applicable. This equation predicts $n_e > 4 \times 10^{12} \text{ cm}^{-3}$ which would result in $t_R < 13 \text{ sec}$, consistent with our upper limit. However, if we use the determination of $\Delta t_m = 6 \pm 3 \text{ sec}$ and apply (6.5.11), we find $t_R \approx 22 \pm 11 \text{ sec}$. Secondly, it is possible that the output spectrum calculated by Payne (1980) and Lightman and Rybicki (1979) is incorrect because they have not calculated a truly self-consistent model. Therefore, we cannot at present use our observations to critically constrain such models. Finally, it is possible that unsaturated Comptonization is not the correct model.

6.6 Source Lifetime

We can set an upper limit for the object's lifetime at its current luminosity by requiring that it cannot have accreted more material than its present mass at an assumed constant accretion rate. If we assume a 10% conversion efficiency of matter into radiation, consistent with some of the theoretical discussions of accretion onto a black hole (see Rees 1979 for discussion of the energetics of accretion onto black holes and see Thorne 1974 for a discussion of possible values of the efficiency), the accretion rate for NGC 6814 must be $\geq 0.002 M_\odot/\text{yr}$ to account for the observed luminosity. This gives a lifetime

$$\tau_L \lesssim \frac{10^6 M_\odot}{0.002 M_\odot/\text{yr}} \approx 5 \times 10^8 \text{ yr},$$

which is considerably shorter than the Hubble time. We cannot rule out the possibility that $M \gtrsim 5 \times 10^6 M_{\odot}$ and that the efficiency is near 30% (Thorne 1974), in which case the source could have maintained its present luminosity for a Hubble time. If the 10% efficiency assumption is correct, one must consider alternate scenarios. Possibilities are that the object has a duty cycle of $\tau_L/t_{\text{Hubble}} \lesssim 0.03$ or that the high luminosity is a recent phenomenon. We note that ~ 0.02 of all galaxies with $M_V < -19$ are active galaxies (Huchra 1977). The value of the "on" duty cycle is therefore consistent with the hypothesis that all galaxies show a Seyfert-like nature for ~ 0.02 of their lifetimes.

FIGURE CAPTIONS

Figure 6.1 -- The X-ray flux from NGC 6814 as a function of time for the first three orbits. Data from both the argon detector and the xenon detector were added together. The effective bandwidth is 3-20 keV. The bin size is 82 sec.

Figure 6.2 (top) -- Enlarged section of the NGC 6814 X-ray light curve plotted in Figure 6.1. Time zero corresponds to 24 minutes in Figure 6.1. For this figure the bin size was 20.48 sec. The data point at 500 sec occurred during a data drop out. (middle) -- The hardness ratio defined as > 6 keV flux divided by the < 6 keV flux in the xenon detector during the event shown above. The hardness ratio was computed every 82 sec. The straight lines represent the hardness ratios expected for the given values of α . (bottom) -- The counting rate in the offset xenon detector for the above event. The offset is 6° from the other detectors. For the data shown χ^2 for a constant source model was 42.06 for 42 degrees of freedom.

Figure 6.3 -- Enlargement of another section of Figure 6.1. For this case the bin size is 20.48 sec and the data is centered near the time 210 minutes of Figure 6.1. The decline into the major dip took only 80 sec.

Figure 6.4 -- Auto-correlation function for NGC 6814. (a) The function for orbits 1-5. (b) The natural logarithm of the curve in (a). (c) The

"detrended" auto-correlation function for orbits 1-5. (d) The natural logarithm of the data in (c).

Figure 6.5 -- Power law index vs. flux for orbital averages. The energy index computed for each orbit is plotted as a function of the average flux during that orbit. The absorption was fixed at $N_H = 4.3 \times 10^{22}$ atoms in the line of sight. The point near 9×10^{-11} ergs/cm² occurred during orbit three when the spectral fit was unacceptable and therefore the error shown may be underestimated.

Figure 6.6 -- Average "hard" flux for a specified "soft" flux. The line labeled $\alpha = 0.75$ is the best fit line to the data. The fact that the line does not go through the origin indicates that the background subtracted was slightly in error. If the spectral shape does not change during an intensity change then the data should lie along a straight line.

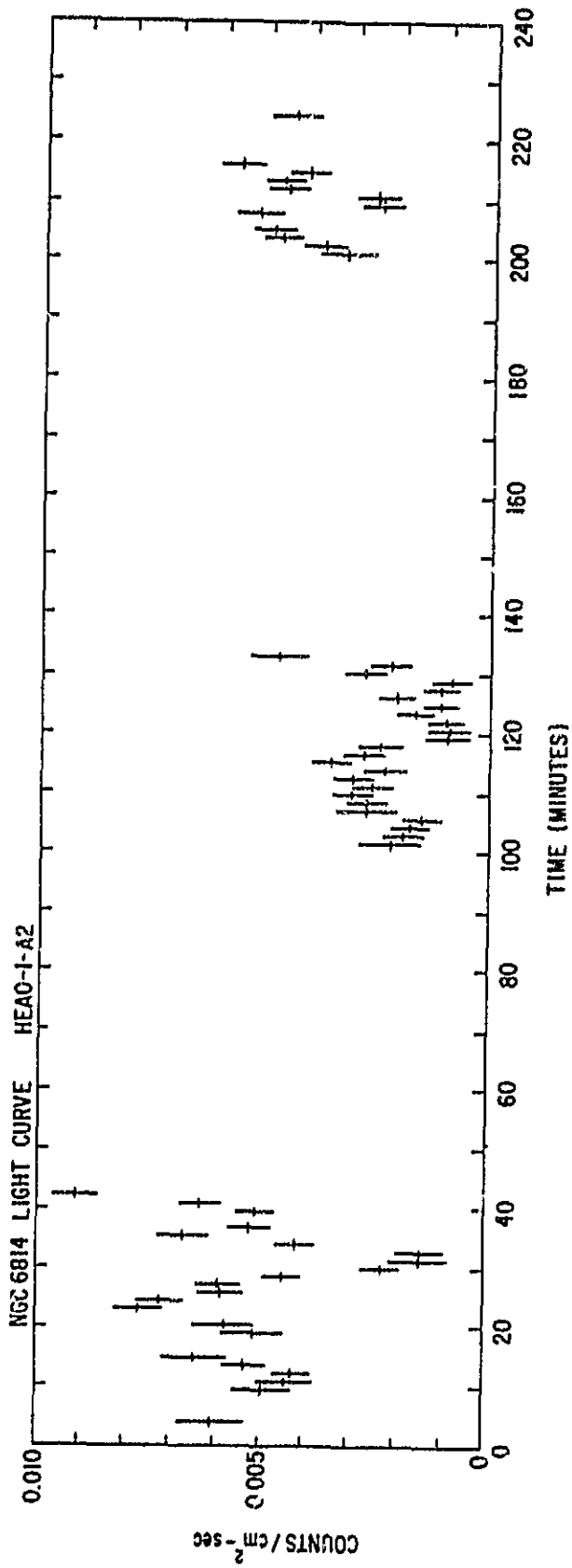


Figure 6.1

ORIGINAL PAGE IS
OF POOR QUALITY

SEGMENT of NGC 6814 X-RAY LIGHT CURVE

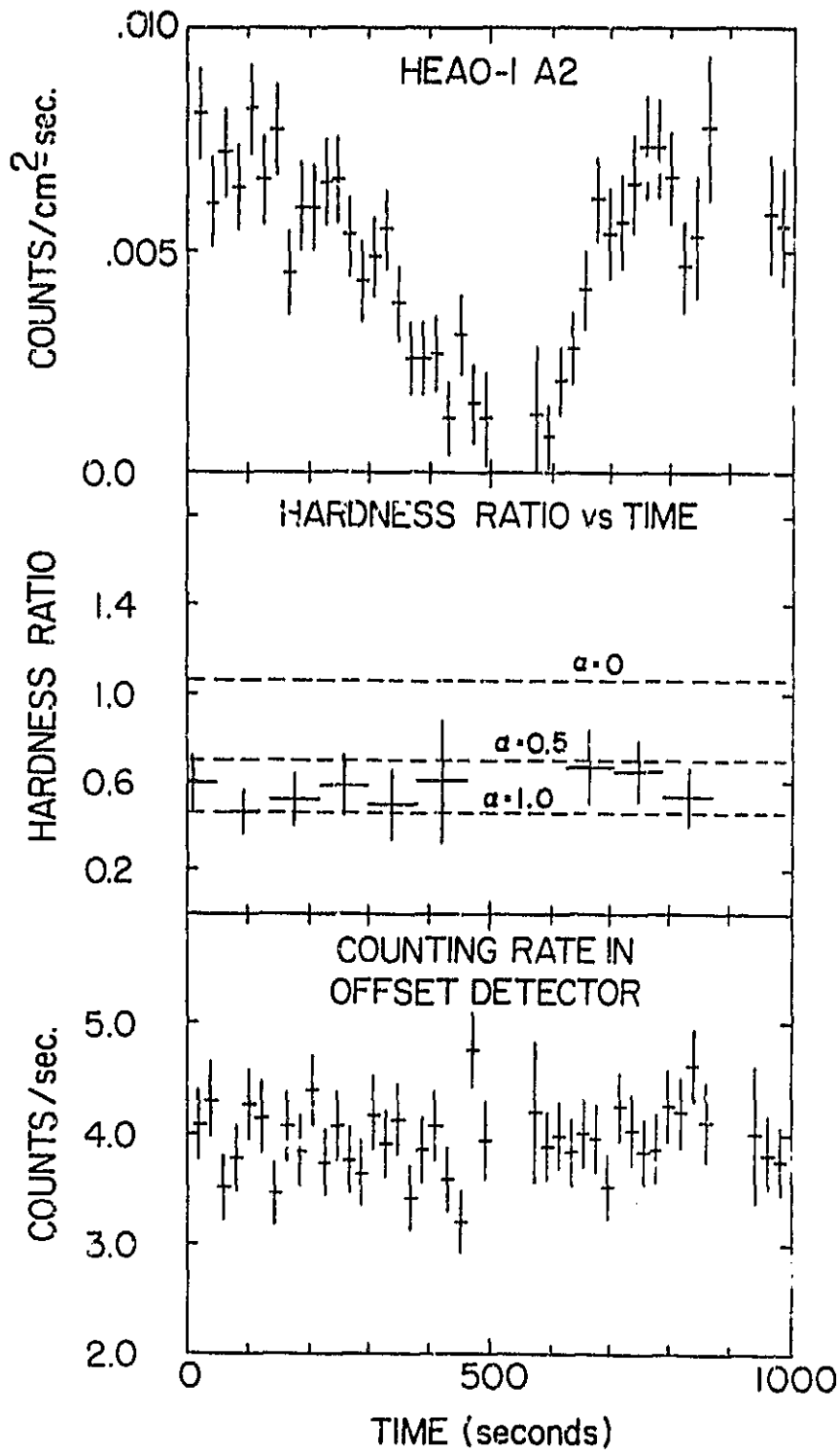


Figure 6.2

ORIGINAL PAGE IS
OF POOR QUALITY

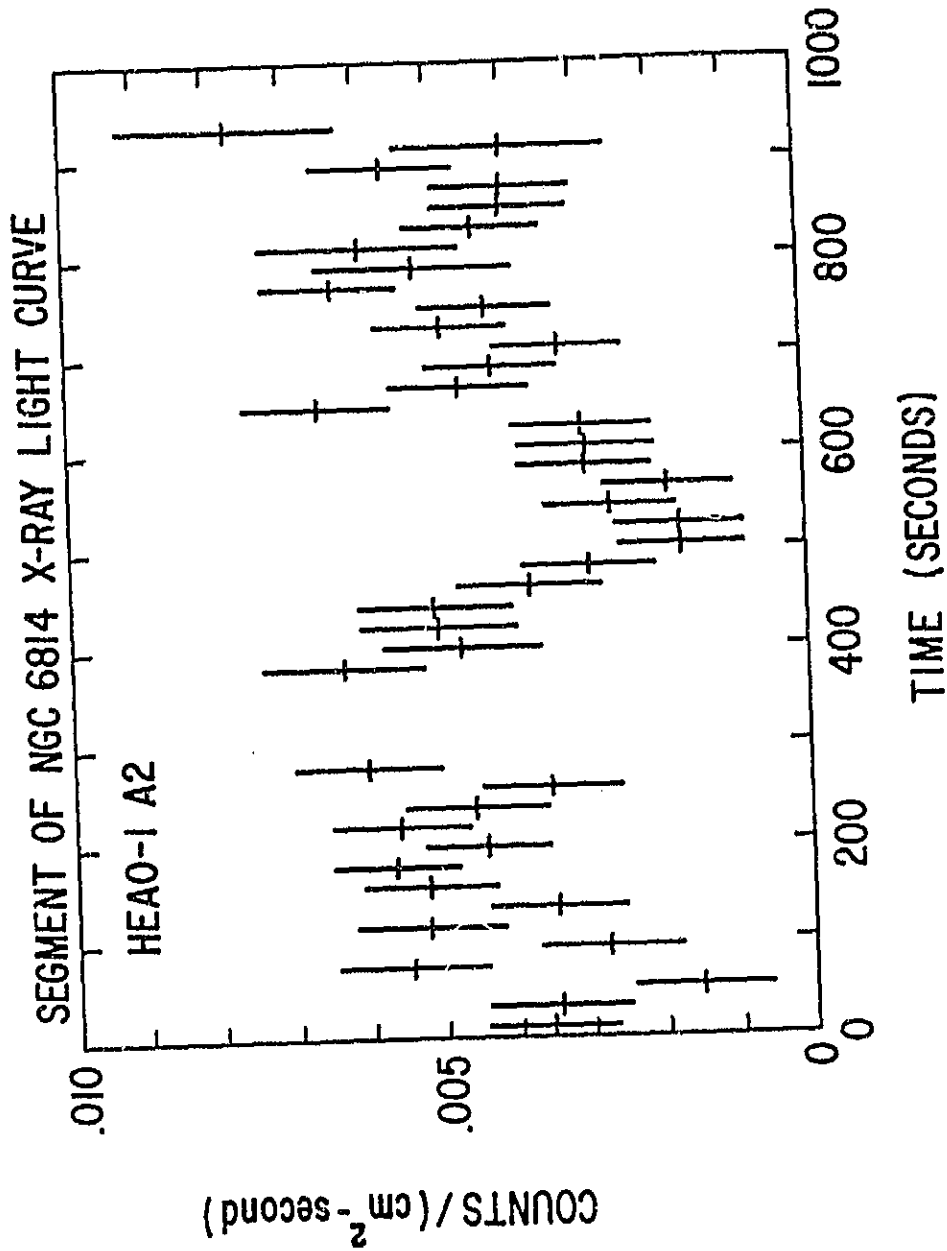


Figure 6.3

ORIGINAL PAGE IS
OF POOR QUALITY

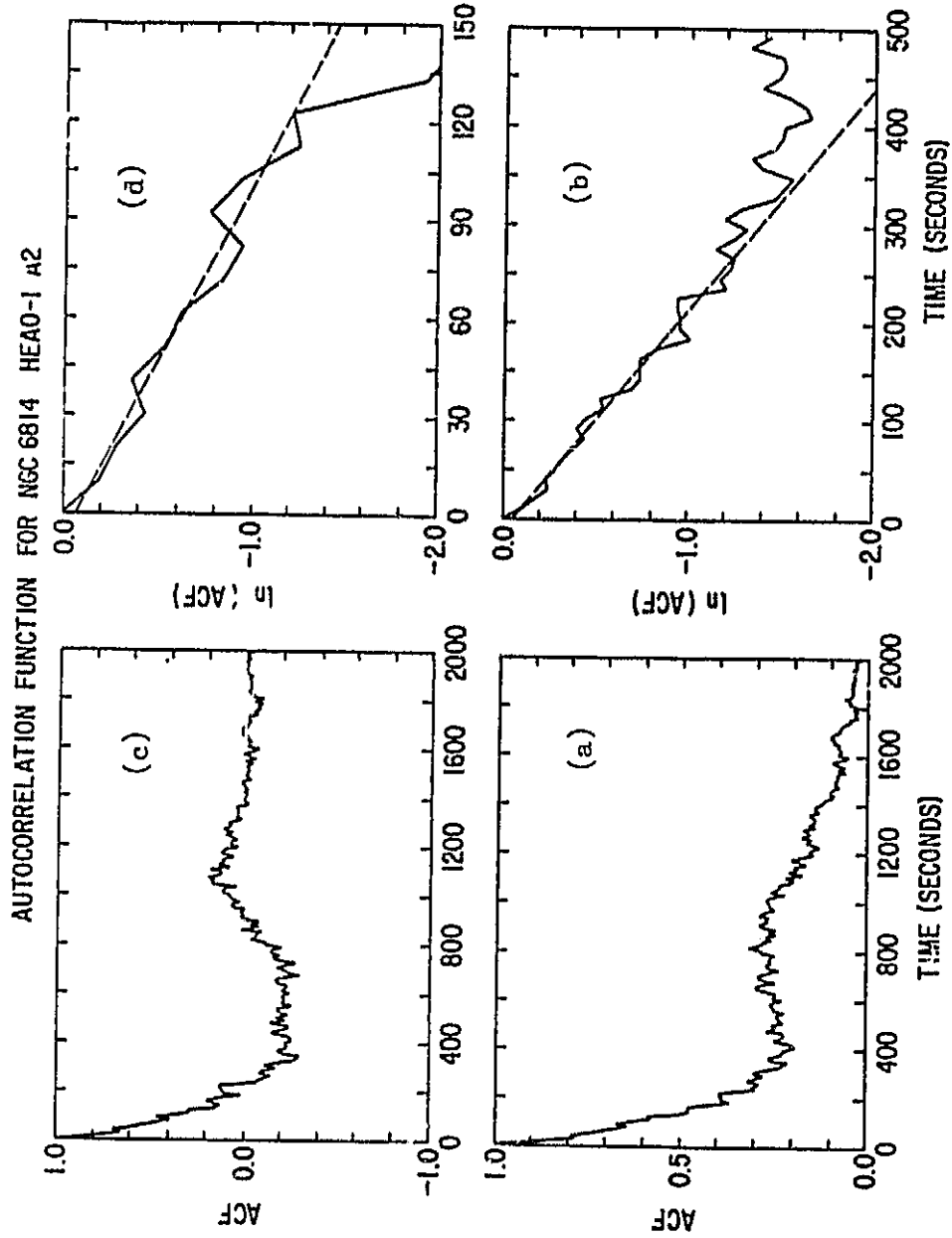


Figure 6.4

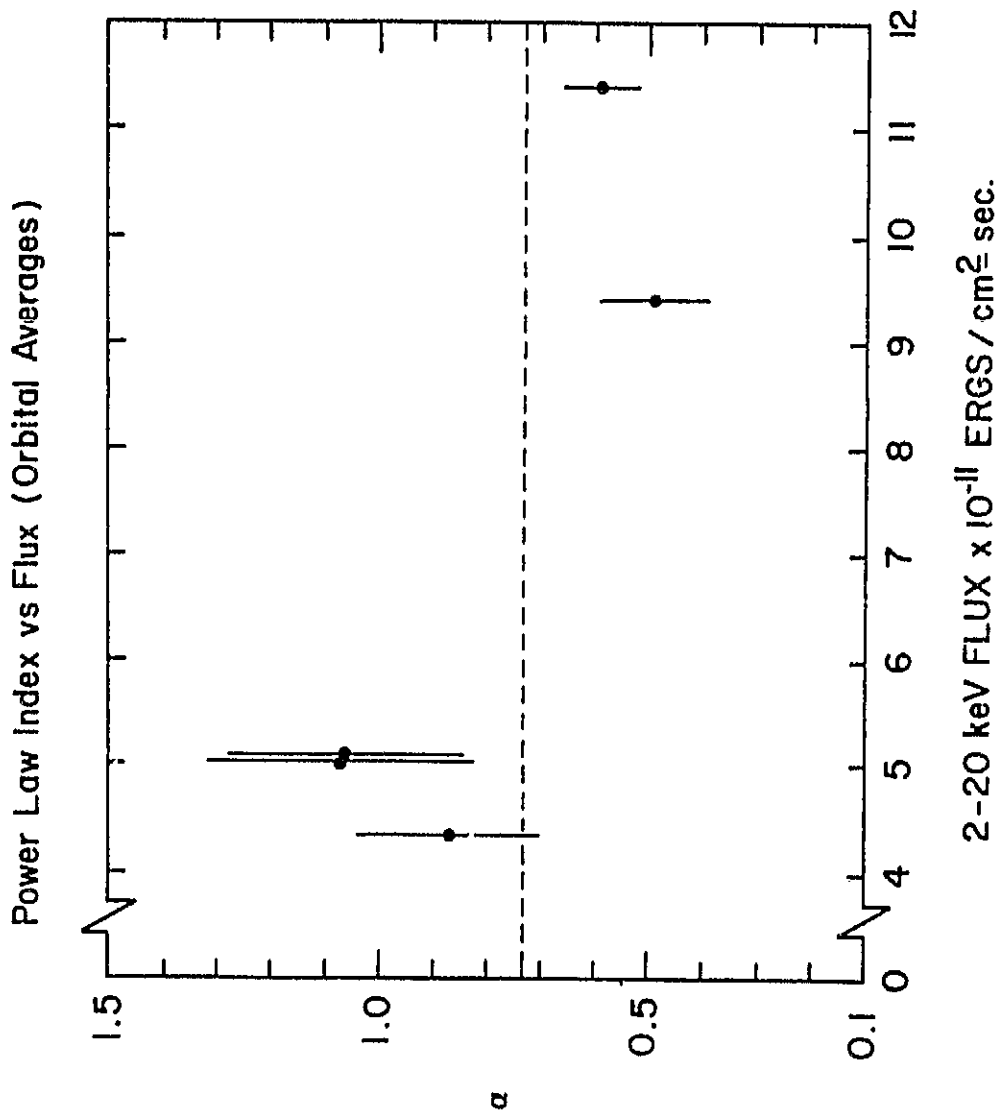


Figure 6.5

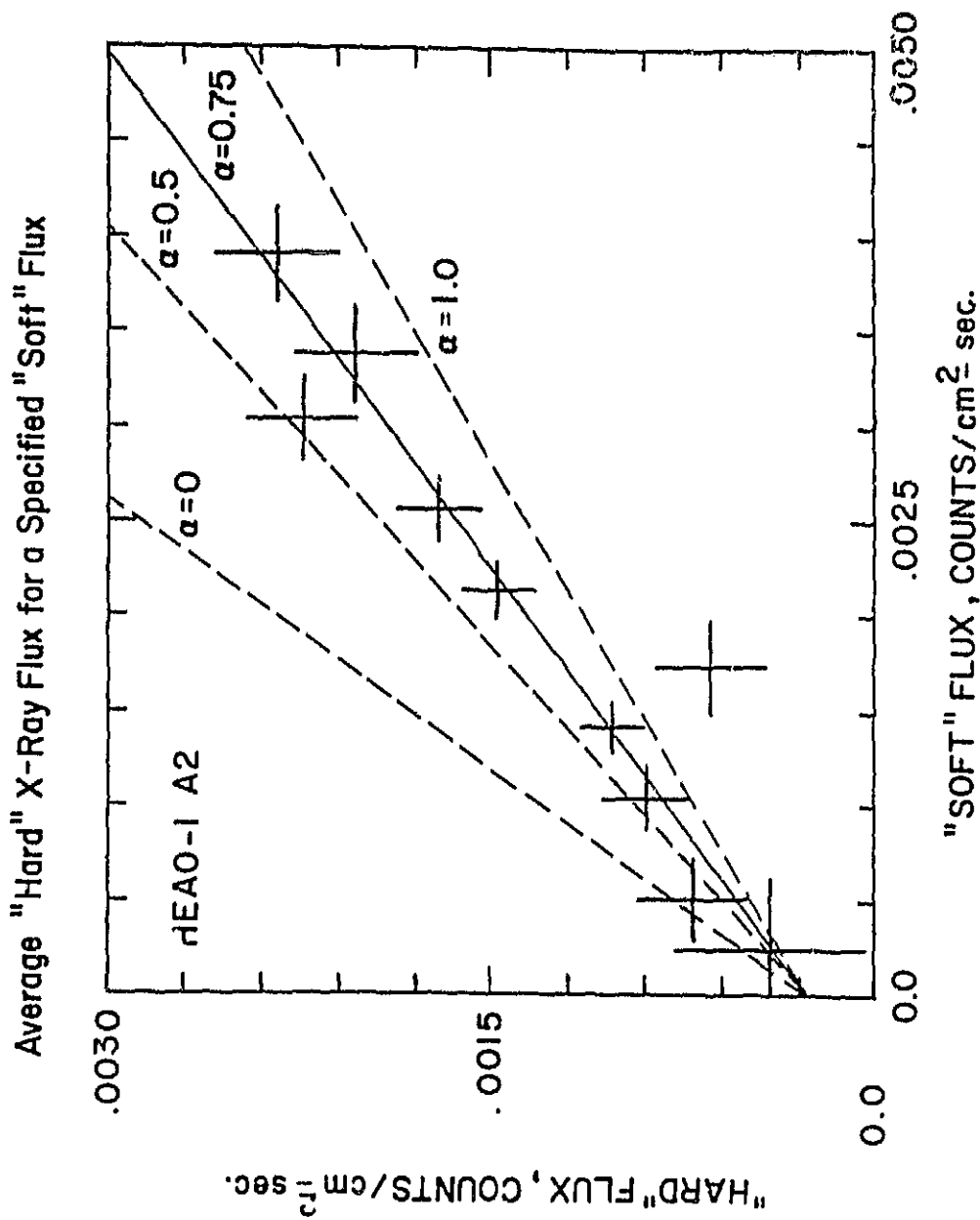


Figure 6.6

7. RECONCILIATION

7.1 Chapter Overview

In Chapter 5 we saw showed that, with one exception, the active galaxies observed by HEAO 1 did not show any evidence for variability on time scales shorter than one day. Chapter 6 was about the exception, NGC 6814, which shows factor of two changes on time scales as short as two minutes. In this chapter we consider other observations of rapid X-ray variability. NGC 4051 appears to be similar to NGC 6814 in several ways. These two objects are very low luminosity active galaxies but when compared with optical data, they are overluminous in X-rays. This could be caused by the X-rays being "beamed" at us or by the objects being new. New objects should have weak secondary emission due to time delays. Lack of variability on short time scales could be due to either stability or to a large source size. We consider both possibilities and consider the implications of the rapid variability of NGC 6814 on such models.

7.2 Comparison With Other Observations Of Variability

The large amplitude short term variability observed from NGC 6814 appears to be unique. Previous observations of rapid variability could be modelled as a single step function for Cen A (Delvaille, Epstein and Schnopper 1978), 3C 273 (Tananbaum 1979) and NGC 4051 (Marshall et al. 1983). The very large flares reported from NGC 4151 (Tananbaum et al. 1978) remain unconfirmed and are likely in error (see Appendix F). Variability from quasars OX 169 (Tananbaum et al. 1979) and QSO 1525+227 (Matilsky, Shrader and Tananbaum 1982) are more interesting. However, both observations are marred by the extremely low count rate, and would have

been improved with a longer run on source.

From the above we conclude that rapid variability is very rare. Even for an individual object only one observation of several shows variability. In addition, the variability observed is often quite different than what was seen from NGC 6814. It is interesting that the light curve that most resembles the X-ray light curve of NGC 6814 (in terms of amplitude and time scale) is the infrared observation of the BL Lac, OJ 287 by Wolstencroft, Gilmore, and Williams (1982). They saw variability in only one observation out of ~ 10 on OJ 287 and presumably a large number of observations of other sources.

If one considers longer time scales, the situation is quite different. In section 1.5 it was noted that Cen A and NGC 4151 both are often variable with a time scale of a few days. These two objects, which have similar luminosities to NGC 6814, vary on ~ 1000 times longer time scale.

7.3 Observations At Other Wavelengths

In this section we will consider NGC 6814 and see whether it has any unusual properties that might help us understand the observed rapid variability.

Rieke (1978) found that both NGC 6814 and NGC 4051 had low, but not unusually low, IR luminosities. When he compared his measurements with those from Stein and Weedman (1976), the two objects that differed the most were NGC 4051 and NGC 6814, although Rieke points out that Stein and Weedman's value for NGC 6814 was probably in error. The difference may be considered as weak evidence for IR variability. More recently, Glass (1979), reporting on IR observations of active southern galaxies, notes that from an IR point of view NGC 6814 (and NGC 3783) are only marginally

Seyfert-like.

Concerning optical correlations, Yee (1980) reports on the very strong correlation between the luminosity in H β and the "nonthermal" luminosity for quasars and both broad- and narrow-line objects. NGC 6814, NGC 4051 and NGC 3227 lie near each other on the correlation but are a factor of 30 weaker than the next strongest Seyfert I galaxy in Yee's sample. NGC 4151, which has a similar X-ray luminosity as NGC 6814, has over 30 times the H β luminosity. Lawrence and Elvis (1982) have shown that the X-ray flux correlates with various optical and IR parameters for most objects. However, compared to the sample as a whole, NGC 6814 and NGC 4051 are underluminous in [O III], 3.5 μ m, and 10 μ m flux relative to their X-ray luminosities. It is also interesting that, in the Lawrence and Elvis plots, NGC 6814 did not have an unusually low H β flux.

There are several ways that one can underproduce optical line emission. The primary energy source for the optical line emission is the absorption of UV photons. Therefore a lack of line emission could be due to either a lack of absorbing matter or a lack of UV photons. The X-ray spectrum of NGC 6814 (Mushotzky et al. 1980) shows absorption caused by $\sim 4 \times 10^{22}$ atoms/cm² along our line of sight. This is similar to the absorption observed in NGC 4151 which would imply that both nuclei have a similar amount of matter around them. As for a lack of UV photons, this would imply that an object like NGC 4151 has a source of UV photons (which NGC 6814 would lack) above the power law continuum. There is no evidence for an additional source of UV photons in NGC 4151 (Malakan and Sargent 1982). Also, it is possible that NGC 6814 has an anomalous ionization parameter.

Another way to decrease the X-ray flux relative to the line emission

is to assume that the observed X-ray flux is not typical. If the X-ray emitting plasma is moving with velocity $\beta = v/c$ then the integrated luminosity will be increased by a factor of δ^4 where δ , the relativistic Doppler factor, is given by

$$\delta^{-1} = \gamma(1 - \beta \cos \theta)$$

where $\gamma = 1/\sqrt{1-\beta^2}$ and θ is the angle between the direction of motion and the direction along the line of sight. In addition the observed time scale for variability will also decrease by a factor of δ . The decrease in the true X-ray luminosity, relative to the (inferred) observed luminosity, by a factor of 30 would require a $\delta = 2.3$ and of course the true time scale would be a factor of 2.3 longer.

A final method to decrease the line flux is to invoke a time delay as the X-ray flux is turned on. X-rays can proceed directly from the central source to the Earth. However, in order to produce the line emission, the ionizing photons must first propagate from the central source to the clouds before a photon from the line can be emitted which can propagate to the Earth. This results in a longer path length for the line emission than for the X-rays. Therefore variability from the lines will always appear to lag variability from the ionizing source and appear to be smeared in time and amplitude.

We note that the probability of seeing 1 object in about 40 in the process of turning on depends greatly on the totally unknown X-ray lifetime of these objects. Consider the following possibility. After the X-ray source turns on, it will take some time $\tau \sim R/c$ to illuminate the entire narrow-line region. This will be the turn-on time. The clouds quickly

heat up and accelerate to $v/c \sim 1/100$ and proceed to escape from the nuclear region. In section 7.3.3 it will be argued that thermal reradiation from these clouds could affect the observed X-rays. Thus the "on" time, which starts when the clouds are heated and ends when the clouds escape, will last ~ 100 times longer than the turn on time. Therefore it is not unlikely to see 1 object in a sample of ~ 40 in the process of turning on. Of course, if this is true, then it implies that an active nucleus has gone through many on-off cycles in the history of the galaxy.

The idea of recurrent activity from galaxies is not new. Oort (1977) gives evidence of nuclear activity for our galaxy 10^6 to 10^7 years ago. I will give two examples of models which "predict" this time scale. Van Bueren (1978) suggested that tidal disruption would fill the potential cusp around the central black hole with gas. As the cusp fills the radiation pressure would build up. After $10^6 - 10^7$ years the radiation pressure would exceed the gravitational pressure. Therefore Van Bueren predicts a long period of relative quiet followed by an explosion. Sanders (1981) considered the interaction of the central black hole with molecular clouds in the nuclear region. He calculates that a molecular cloud would collide with the hole once every $\sim 10^7$ years. Activity would last $\sim 10^5$ years and so Sanders predicts a $\sim 1\%$ duty cycle. In both these models one expects to see X-rays only during the short active phase.

If one turns on an X-ray source in an originally "normal" nucleus then one expects first to detect the effects on material closest to the nucleus. Since the broad-line region is often less than one pc in size, an external observer would see the entire region illuminated in only a few years. However, the narrow-line region, which is 100-1000 pc across, will only be partially illuminated for young objects. Thermal reradiation from

dust exterior to the nucleus should turn on with the narrow-line region. In this picture Seyfert 2 galaxies represent the class which is turning off. Thus a large fraction of the observed differences in Seyfert galaxies would represent different snapshots of a single process. However tempting such a model is, we note it does have problems. Dust near the nucleus will be at the highest temperature and will be observed to turn on first. This is contrary to observations in that NGC 6814 does have 10 μm emission (Rieke 1978), indicating a cool temperature for the dust, and NGC 1068 (a Seyfert 2) has an IR spectrum requiring a dust temperature of ~ 1000 K (Jones et al. 1977).

7.3.1 Stability Related to the Eddington Limit

Cowie, Ostriker and Stark (1978) and more recently Krolik and London (1983) considered the long term stability of accretion. If the luminosity is $\lesssim 1\%$ of the Eddington limit stable flows can develop. This would explain the observed stability for our objects if they are $\lesssim .01 L_{\text{EDD}}$. They assumed that the central object was imbedded in a homogenous gas and so the shortest time scale obtained was related to the sound travel time across the sonic radius. Therefore they did not consider the extremely short time scale observed for NGC 6814. This model does predict that NGC 6814 should be highly variable on a time scale of ~ 1 year. This is in agreement with Halpern (1982) who reported that the 2-10 keV flux from NGC 6814 was down by a factor of 10 one year after the HEAO-1 observation.

7.3.2 Increased Number Of Shots

In the Guilbert, Ross, and Fabian (1982) model a cloud is heated via some unknown mechanism and then allowed to cool via inverse Comptonization. Since the cooling times are very short, the observed X-ray spectrum is a time average. Their calculated "averaged" spectrum is in

good agreement with observations of the X-ray spectra of active galaxies. However, if the X-ray source is powered by discrete events, these events should give rise to low-amplitude variability. To illustrate we apply the shot noise model. In this model λ events per time interval each rise to amplitude h and then exponentially decay away with time scale τ . Thus using $I = \lambda h \tau$ and $\sigma_I^2 = \lambda h^2 \tau / 2$ we construct

$$\sigma_I / I = (2 / \lambda \tau)^{1/2}.$$

We set $N = \lambda \tau$, which represents the number of "simultaneous" events taking place. If we assume that τ is longer than the smallest bin size we used (see Sutherland, Weisskopf, and Kahn 1978, Appendix A, to see how σ_I^2 is a function of bin size) and that λ is greater than one shot per day, then we can use σ_I / I from Table 5.1. For NGC 6814, $N \sim 10$, which says that at any one time on the average, 10 clouds dominate most of the X-ray flux. A more typical value of σ_I / I near 10% implies that $N \sim 200$, and for Cen A, N is greater than 1000. Since Cen A, NGC 4151, and NGC 6814 all have roughly the same luminosity, accounting for the lack of rapid variability in Cen A and NGC 4151 by increasing the number of shots only works if the shots become much more numerous, and as a result, each event becomes much less luminous.

One way to reconcile the Guilbert, Ross, and Fabian (1982) model with the lack of variability is to assume that the heating and cooling are taking place in a continuous matter.

7.3.3 Growth Of New Source Of Soft Photons

In the inverse Compton reflection model (Lightman and Rybicki 1980), low-energy (soft) photons enter a region of energetic electrons. The soft

photons inverse Compton scatter from the electrons to emerge from the cloud as X-rays. In this section, we will examine the inverse Compton reflection process and find a constraint on the temperature of the soft-photon source. We will make no assumptions about the electron population, i.e., the distribution can be either thermal or nonthermal. We will assume that the X-ray emitting plasma is quite small and stable. By stable we mean that any variability seen is due to variations in the soft-photon source and not due to changes in the plasma itself. Tennant et al. (1981), using the results of Lightman and Rybicki (1979), pointed out that the lack of spectral change during the intensity variations observed in NGC 6814 is consistent with this interpretation. Thus the lack of rapid variability in most sources could be explained by the growth of another "stronger", but more constant, source of soft photons. If the X-ray source is slowly heating up its environment, then thermal reradiation could be the new, constant, strong source of soft photons. This is consistent with the observed deficient IR flux for the rapidly varying galaxies.

We will now find the minimum temperature that a thermal source can have and still provide enough photons (for Comptonization) to generate the observed spectrum. If the soft photons are at a temperature of kT , then the observed power law will extend from $\sim 3 kT$ cut to energies determined by the temperature of the scattering cloud. For the case of NGC 6814 the total number of photons radiated in the Comptonized spectrum is at least

$$N_C = 4.7 \times 10^{-3} 4\pi d^2 \int_{3 kT}^{10 \text{ keV}} E^{-1.7} dE,$$

which corresponds to 2.1×10^{52} photons/sec $(kT/1 \text{ eV})^{-0.7}$ at a distance d of 21 Mpc. The number of blackbody photons impinging onto the X-ray region

is given by

$$N_{\text{BB}} < 2.7 \times 10^{49} r_{100}^2 \left(\frac{kT}{1 \text{ eV}}\right)^3 \text{ photons/sec,}$$

where r_{100} is the radius of the X-ray emitting region in units of 100 lt-sec. N_{BB} is maximum when the dilution factor is equal to unity. Since for Compton scattering, photon number is conserved, we set $N_{\text{C}} = N_{\text{BB}}$ and find that

$$kT > 6.0 r_{100}^{-1/2} \text{ eV.}$$

If $r_{100} < 1$, then we find the thermal source must have $kT > 6.0$ eV (70,000 K). Dust grains would quickly vaporize at this temperature. This leads us to conclude that thermal radiation from dust cannot provide enough photons to generate the observed spectrum for a small X-ray source. This problem is serious for NGC 6814, where the "hot spots" which provide the soft photons must be small and few in number in order to account for the rapid, large-amplitude variability seen. If these spots reside outside the X-ray region, then the dilution factor must be very small, and hence $kT \gg 6.0$ eV.

7.4.1 Large Source Size

To summarize the results of the last section, if the source of soft photons is thermal in nature and if some of the optical and/or IR emission comes from the X-ray plasma directly, then the X-ray cloud must have $r_{100} \gg 1$. Since there appears to be some correlation between 3.5 μm IR emission and X-ray flux for most active galaxies (Lawrence and Elvis 1982) and since a large source size is consistent with the absence of rapid X-ray

variability reported here, we will consider the possibility of large X-ray regions. In order for 1000 K blackbody photons to be the soft-photon source, we find that $r_{100} > 2700$ (≈ 3 lt-days). This size is consistent with previous observations of variability (Marshall, Warwick, and Pounds 1981). An X-ray plasma this large could be generated in one of two ways in the black hole accretion picture. Either the central object is large, hence very massive, or else the X-rays come from a large region not directly related to the central object.

7.4.2 Two Components

In this section I assume that X-rays are produced in two components; a small variable component that would dominate in NGC 6814 and large more constant component that would dominate for the remaining objects. Let us assume that the total power produced by a galactic nucleus comes out in two forms--the immediate production of X-rays L_f and some initially unobserved power P . The latter could be in the form of relativistic electrons, as mentioned above, or in γ -rays, as in the Penrose photoproduction model (Leiter 1980). The quantity P will slowly fill a reservoir with energetic electrons. When steady state is reached, the luminosity of the reservoir will be $\langle P \rangle$. Therefore, the total X-ray luminosity L_x will be

$$L_x = L_f + \alpha \langle P \rangle = L_f + r \langle L_f \rangle,$$

where α is the fraction of the reservoir's luminosity which comes out as X-rays and r is $\alpha \langle P \rangle / \langle L_f \rangle$. Below we will assume r is constant and that $\alpha \sim 1$.

Since only L_f will show rapid variability, let us consider what happens to σ_I/I when one adds a variable source to a source of constant

intensity I_0 . If we assume that the intensities of the variable component are uniformly distributed between 0 and ΔI , then

$$\sigma_I/I = \Delta I [3^{1/2} (2I_0 + \Delta I)]$$

for the sum of both components. We will now assume that the reservoir does not vary on the time scales we have sampled and also that the X-rays produced near the central object are highly variable. If we set $I_0 = r \langle L_j \rangle$ (the luminosity of the reservoir) and $\Delta I = 2 \langle L_j \rangle$ (the range of luminosities for immediate X-ray production), then

$$\sigma_I/I = \frac{1}{3^{1/2} (1 + r)}$$

We define F to be the fraction of the total X-ray flux coming from the compact-variable region, which is given by $1/(1 + r) = 3^{1/2} \sigma_I/I = F$.

We can check the consistency of this model by assuming that $F = 75\%$ and that the average flux is 4 for NGC 6814. Thus, if the assumption of a uniform distribution of intensities is correct, we would expect to see the source vary from ~ 1 to ~ 7 . The NGC 6814 flux shown in Figure 6.1 varies from ~ 2 to ~ 7 , which is in rough agreement with our model.

Since our upper limits for σ_I/I typically lie in the range of 10%, we find that F is typically less than 17%. For NGC 4151, which has $\sigma_I/I \lesssim 6\%$, we find that $F \lesssim 10\%$. Thus the constant component would have to grow by a factor of 10 (relative to the variable component) in order for σ_I/I to decline from the NGC 6814 value to the level observed for NGC 4151. One possibility is that NGC 6814 has not filled its reservoir and thus has not come to steady state. This is unlikely since it implies

that when steady state is reached, the luminosity will be 10 times what it is now. As shown in Tennant et al. (1981), such a high total luminosity, if it were variable on the same time scale, would clearly violate the Fabian and Rees relation (1979). However, it is unclear as to whether the Fabian and Rees relation applies in this case since we are talking about a steady state condition. If the X-rays from the variable component pass through the reservoir, electron scattering could reduce the amplitude of variability. If the electrons have the correct power-law distribution, scattering will not greatly alter the spectrum. One could also argue that NGC 6814 does not have a reservoir for some unknown reason or that the X-ray production efficiency α for the reservoir is low.

APPENDIX A

Weighting The Data

In this section we will consider the effects of basing the weights on the observed number of counts rather than the expected number. We will assume that the observed count rate has a Poisson distribution with a mean of μ . In order to consider analytic results, we will assume that μ is small. Since μ is the mean number of counts per bin, it is always possible (subject to experimental considerations) to generate data with small μ by binning the data into a large number of bins.

First, we will need to determine the appropriate weight for a bin that contains no counts. To do this consider dividing the data into such a large number of bins that each bin contains either zero or one count. For this case

$$\langle x \rangle_w = \frac{0 \cdot w_0 f_0 + 1 \cdot w_1 f_1}{w_0 f_0 + w_1 f_1} \quad (\text{A1})$$

where f_n is the fraction of the total number of bins that contain n counts and w_n is the corresponding weight.

We know that, on the average, f_n is the probability of getting n counts. Since μ is small, we can expand $P_p(x; \mu)$ to first order to obtain

$$f_0 \cong P_p(0; \mu) \cong 1 - \mu$$

$$f_1 \cong P_p(1; \mu) \cong \mu \quad (\text{A2})$$

$$f_n \cong P_p(n; \mu) \cong 0, \text{ if } n > 1$$

When we apply (A2) to (A1) we find that

$$\langle x \rangle_w = \frac{w_1 \mu}{w_0(1-\mu) + w_1 \mu} = \frac{w_1 \mu}{w_0 + \mu(w_1 - w_0)} \quad (\text{A3})$$

If we require $\langle x \rangle_w = \mu$ we find two solutions; either $\mu=1$ or $w_0 = w_1$.

Clearly $\mu=1$ does not apply to our case and so we find $w_0 = w_1$. Thus, if $w_n = 1/n$ we find that a good definition for w_0 is to let $w_0 = 1$.

Now assume that we have some bins with 2 counts in them but (effectively) no bins with 3 or more counts. Now we must expand P_p to second order which gives

$$\begin{aligned} P_p(0; \mu) &\approx 1 - \mu + \frac{\mu^2}{2} \\ P_p(1; \mu) &\approx \mu - \mu^2 \\ P_p(2; \mu) &\approx \frac{\mu^2}{2} \end{aligned}$$

The weighted average is given by

$$\langle x \rangle_w = \frac{0 \cdot w_0 f_0 + 1 \cdot w_1 f_1 + 2 \cdot w_2 f_2}{w_0 f_0 + w_1 f_1 + w_2 f_2}$$

where f_n is the fraction of the bins that contain n counts. Again, for a large number of bins, $f_n \approx P_p(n; \mu)$, and so

$$\langle x \rangle_w = \frac{w_1(\mu - \mu^2) + 2 w_2 (\mu^2/2)}{w_0(1 - \mu + \mu^2/2) + w_1(\mu - \mu^2) + w_2(\mu^2/2)}$$

Now we make use of the fact that $w_0 = w_1 \equiv w$, and obtain

$$\langle x \rangle_w = \frac{w\mu + \mu^2(w-w_2)}{(1 - \frac{\mu}{2})w + \frac{\mu}{2}w_2}$$

It is clear that $w_2 = w$ gives the correct result of $\langle x \rangle_w = \mu$. However, if the weights are based on the observed number of counts ($w_1 = w_0 = 1$ and $w_2 = 1/2$) then

$$\langle x \rangle_w = \mu (1 - \frac{\mu}{2}).$$

This shows that a bias exists when the weights are based on the observed number rather than the expected number of counts.

APPENDIX B

McIlwain's L Parameter

In this appendix I briefly describe what McIlwain's L parameter is and why it is useful.

In a pure dipole magnetic field the trapping of charged particles is relatively simple. Since the particles follow the field lines, a useful coordinate system is one that labels field lines. In such a system, a pure dipole field is described by

$$B = \frac{M}{R^3} \left(4 - \frac{3R}{L}\right)^{1/2}, \quad R = L \cos^2 \lambda \quad (\text{B.1})$$

where (R, λ) are the polar coordinates (radius and geomagnetic latitude) of the point in question, B is the magnetic field strength, and M is the dipole moment. The quantity L is constant along a field line and measures the distance from the origin of the field to the point at which the field line crosses the equatorial plane. Figure B.1, adapted from McIlwain's 1963 paper, illustrates this transformation.

The Earth's field is not a pure dipole. McIlwain (1963) proposed a coordinate system which preserves the simplicity of the (L, B) system described above. In effect, one maps the Earth's field into a pure dipole while preserving an adiabatic invariant. In the new coordinate system the observed particle flux should be a simple function of (L, B) . Figure B.2 from McIlwain's paper, illustrates where the trapped particles lie in the (L, B) system. In Figure B.3 I have illustrated the location of the HEAO-1 spacecraft in the (L, B) plane for a typical pointed observation. This figure shows that HEAO-1 is below the bulk of the radiation belt. Electron

events occur when a group of trapped particles loses some energy in the Earth's atmosphere and starts to follow lower field lines. These events tend to be of short duration, since electrons are not trapped at these lower altitudes. We have found that such events tend to be seen at high values of L although Appendix C mentions two events that were seen at lower values of L .

E. Boldt (private communication) has pointed out another effect. Primary cosmic rays leave tracks throughout the detector and so are eliminated by the anticoincidence logic. However, cosmic rays can produce secondaries which will not be eliminated. For example the cosmic ray could knock out a K-shell electron in the walls of the detector. When the atom recombines it is possible for it to emit an X-ray into the detector volume which would contribute to the background rate. It is also possible for the cosmic rays to produce γ -rays (via neutral pion production in the spacecraft). These γ -rays can produce low energy Compton electrons in the detector volume. If the electron deposits its energy in one cell then it will not trigger the anticoincidence logic. Thus we find that some fraction of the detector background should be related to the particle background measured by the anticoincidence rate.

McIlwain L is a good measure of cosmic ray flux (see Smart and Shea 1967). The reason is simple to understand. The Earth's magnetic field tends to keep charged particles out. Near the magnetic pole (high L) cosmic rays from some directions can follow a field line down to the Earth's surface. Near the equator (low L) cosmic rays must cross field lines no matter what direction they come from. Therefore low energy cosmic rays are excluded from these regions of low L . Since the cosmic

ray spectrum falls rapidly with energy, excluding the low energy particles results in a total particle flux decrease. Thus high values of L correspond to higher cosmic ray flux and hence increased contamination.

FIGURE CAPTIONS

Figure B.1 -- The mapping of the geomagnetic coordinates R and λ onto the B, L plane according to (B.1).

Figure B.2 -- Contours of trapped particle flux in the B, L plane (McIlwain 1963).

Figure B.3 -- The location of HEAO-1 detector is plotted on the B, L plane every 40.96 sec.

ORIGINAL PAGE IS
OF POOR QUALITY

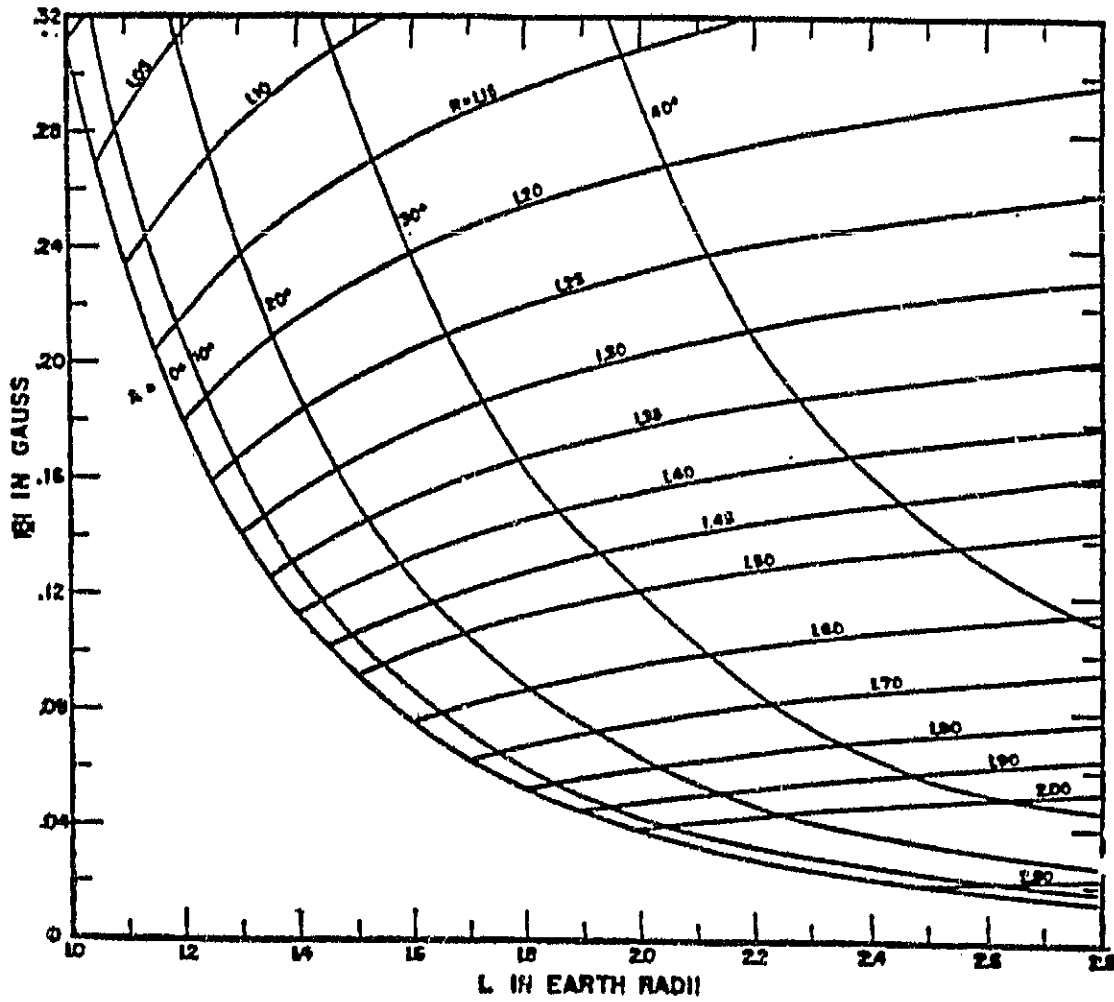


Figure B.1

ORIGINAL PAGE IS
OF POOR QUALITY

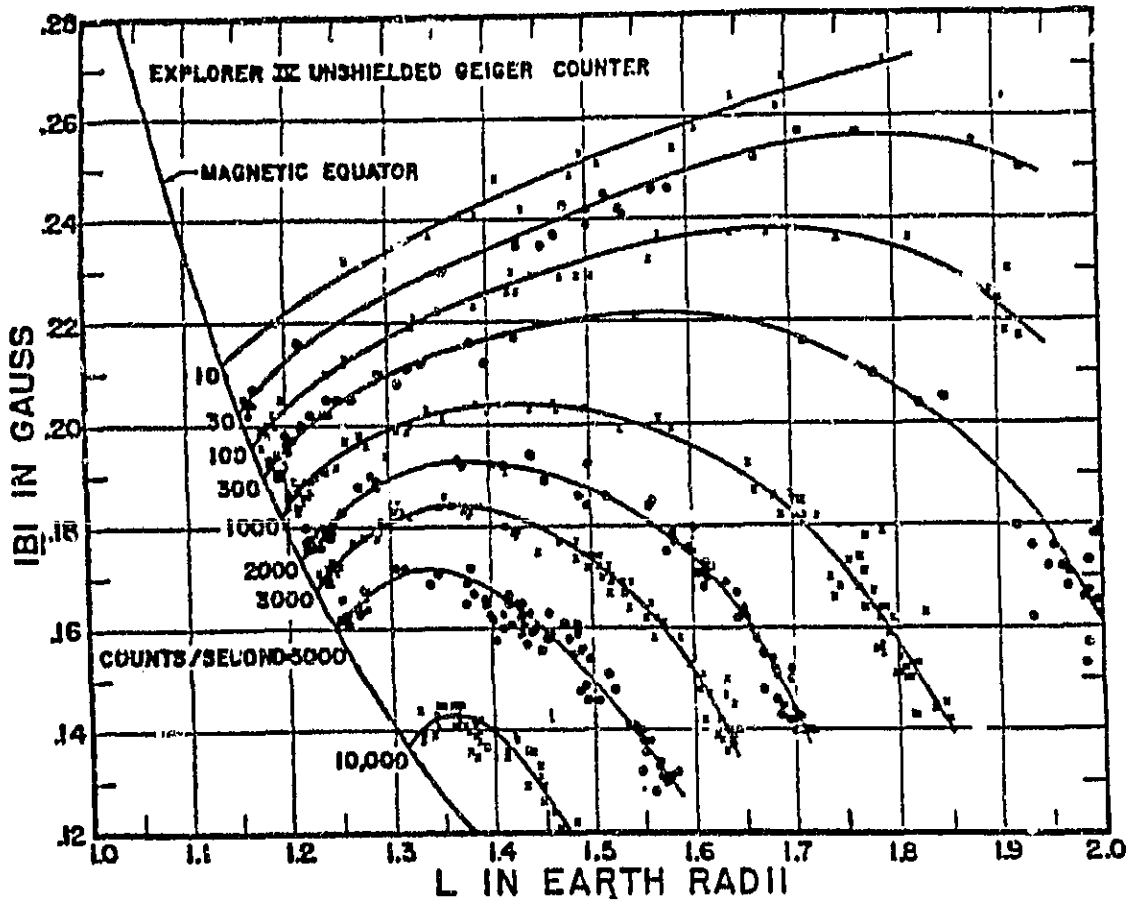


Figure B.2

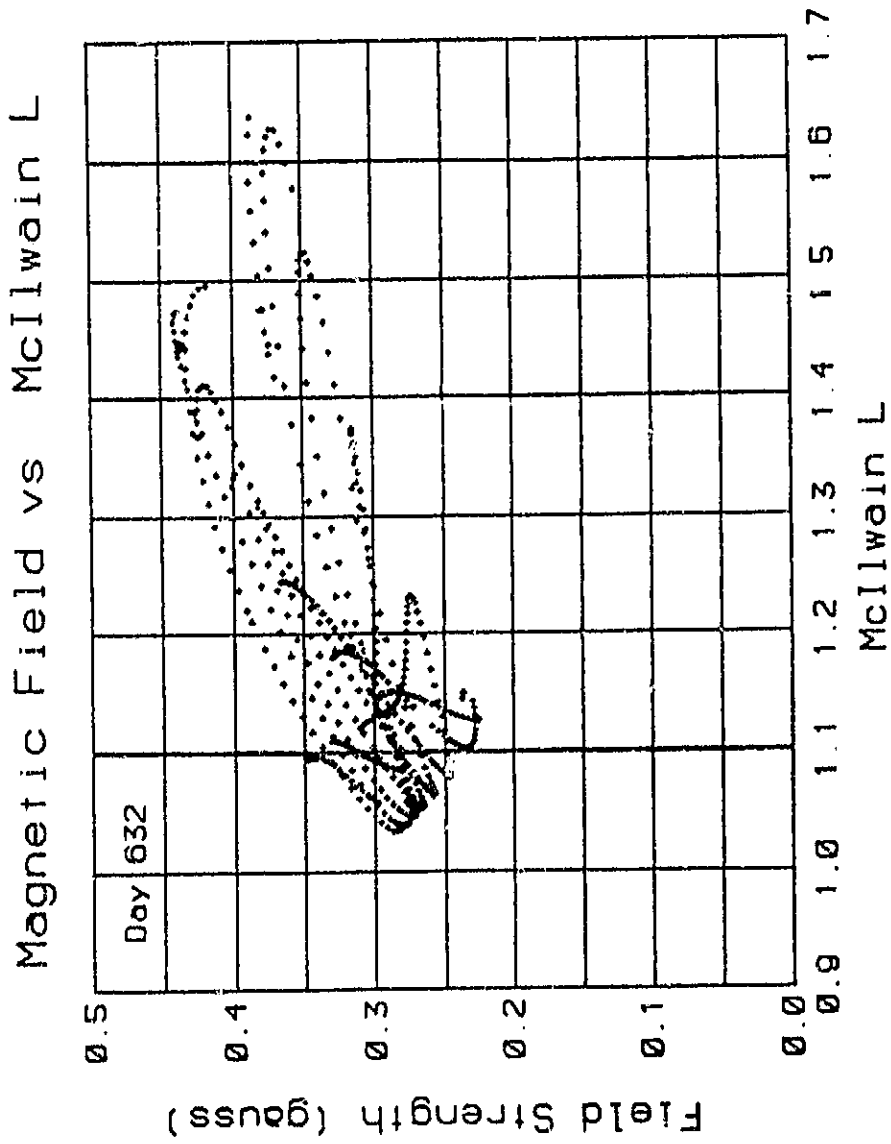


Figure B.3

APPENDIX C

The Rejects

In this appendix I discuss the instances of apparent variability which were not actually associated with the target sources.

When searching for source variability, I examined the rates for all minus-y points, and used χ^2 to test whether the rates were constant. If a source was flagged as being in the field of view then any detected variability was assumed to be due to the source. No attempt was made to determine if the source actually caused the variability or not. The rates were also examined by eye. Two flares were originally discovered using this method (see section 4.6).

The first flare was observed on July 11, 1978. The light curve is displayed in Figure C.1. The spectrum was unusual in that it rose with energy. We were also concerned that the two xenon detectors (HED2 and HED3) did not see the same flux. The offset xenon detector (HED1) did not see the event at all. When we later discovered that the flare was coincident in time with a solar flare, it became obvious that the counts were due to low energy γ -rays entering the detector from the side. Attenuation in the walls of the detector greatly reduced the flux of < 20 keV flare photons. HED3 was closest to the sun and was the detector with the largest count rate. HED1 was behind both HED2 and HED3 and so showed the smallest (i.e. no) response. Later in the day a second, larger solar flare occurred. The rate from this event is illustrated in Figure C.2. This gigantic flare took place while the spacecraft was scanning and so is presented here for its curiosity value.

The second minus-y flare was observed on December 29, 1978. Its

light curve is shown in Figure C.3. It is interesting in that it resembles the light curve for the first solar flare. The spectrum, though, is well fit by a simple (decreasing) power law that is typical of many X-ray sources. All three detectors which observed the source saw the same flux whereas the off source detector saw nothing. We believe that this event is a "nearby" galactic source (see Tennant and Swank 1983). Models of accreting neutron stars predict such events.

During the observations of active galaxies there were two events that we do not consider to be due to a galaxy. These events are illustrated in Figures C.4 and C.5. In both cases the offset detector saw the events. This is a strong indication that the flares were caused by electron contamination. Moreover, as shown in the bottom half of Figures C.4 and C.5, the propane veto rate was extremely high. The propane only weakly responds to X-rays but does respond to the passage of charged particles. This is also strong evidence that the events were particle induced. Low energy electrons would only have been detected in one (mostly the first) layer, and so could have produced these events.

The reason these events slip through our electron flag is quite simple. We calculate the number of electrons stopping in the detector based on the total anticoincidence rate. However, if the electrons are predominately stopped in the first layer, then they will not substantially increase the anticoincidence rate. Thus, for this case, we underestimate the number of electrons entering the detector. Examination of the PHA data for the events seen in Figures C.4 and C.5 shows that the contamination is mainly due to a copper fluorescence line. Therefore, the electrons are not strongly affecting our count rate directly but rather are knocking out K-shell electrons from the copper collimator. X-rays are emitted when the

copper atoms recombine. It is important to realize that flare-like events in our data are very rare. These were the only two events seen in the more than 150 hours of data examined. To be on the safe side, it is recommended that future work use an electron flag based on the first layer rate instead of the total anticoincidence rate.

FIGURE CAPTIONS

Figure C.1 -- Xenon total rate vs. time during a solar flare. Time 0 corresponds to 15980 sec.

Figure C.2 -- Total rate in the xenon detector vs. time during a major solar flare. The tic marks are not related to the size of the error bars.

Figure C.3 -- The sum of the xenon and argon detector rates vs. time during an X-ray flare.

Figure C.4 -- (top) The rate in the top layer of the xenon detector vs. time. An excess is seen around 77000 sec. (bottom) The rate in the propane layer in front of the xenon.

Figure C.5 -- Same as C.4 except this event occurred at 30000 sec on day 550.

ORIGINAL EACH IN
OF POOR QUALITY

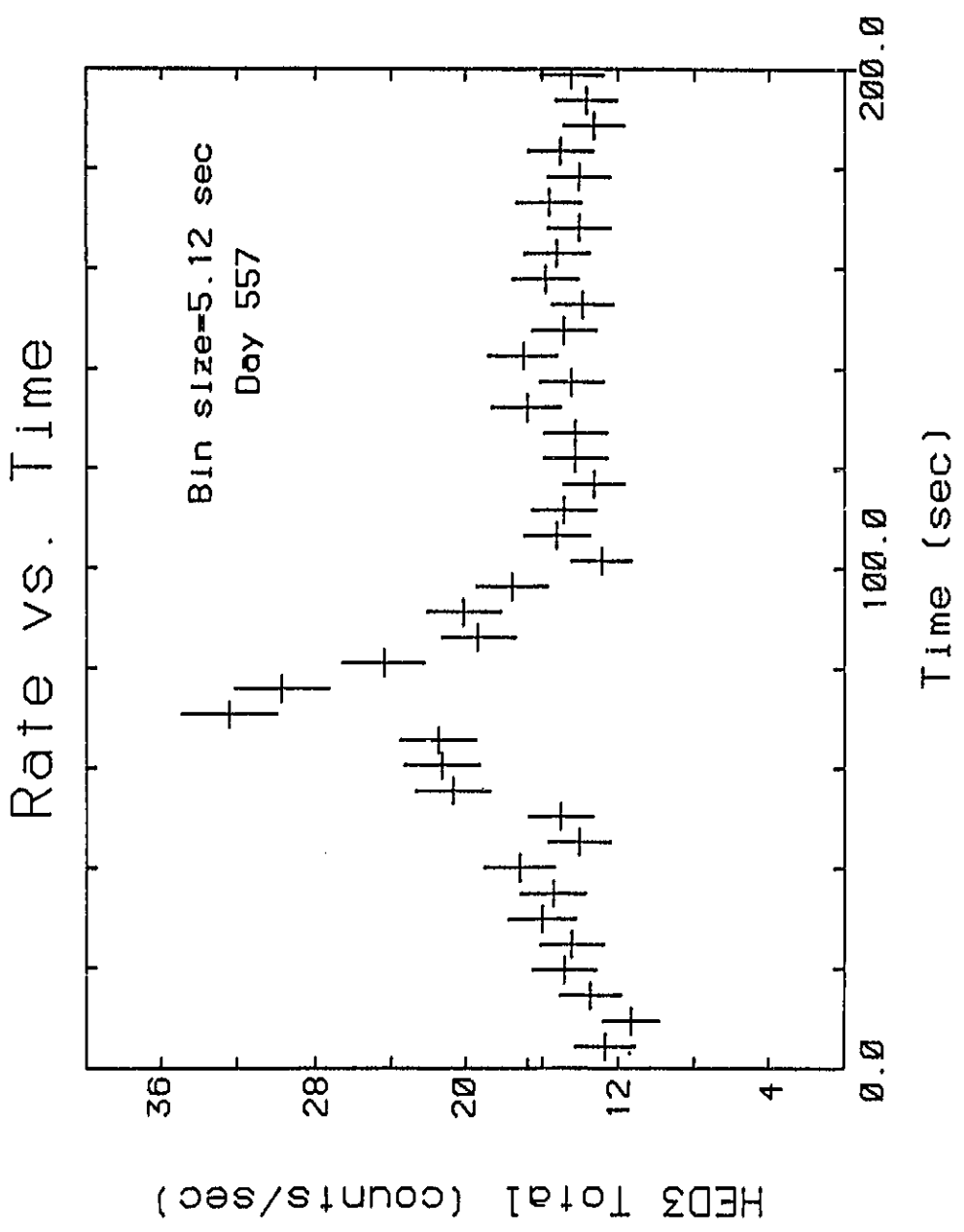


Figure C.1

ORIGINAL FILE IS
OF POOR QUALITY

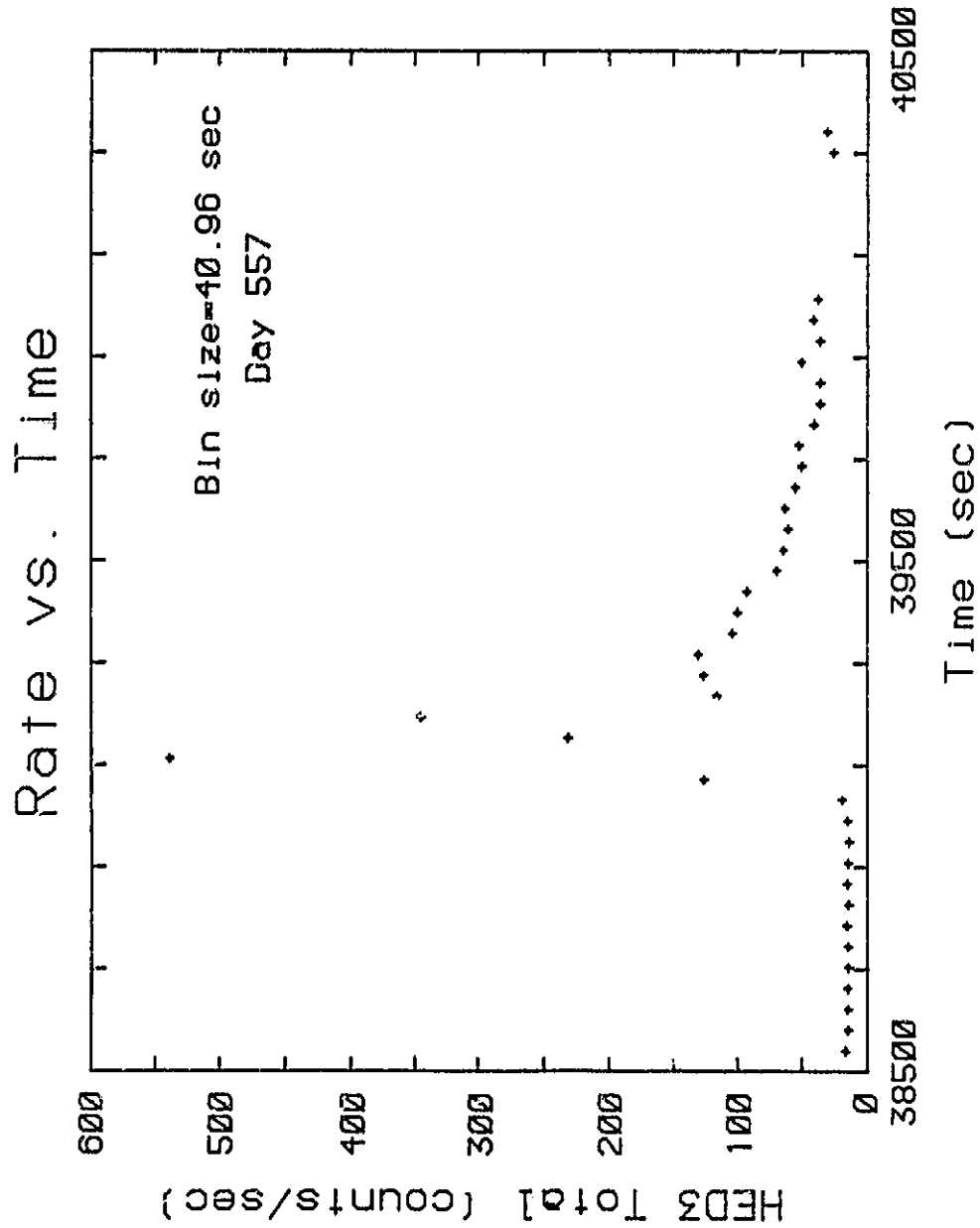


Figure C.2

ORIGINAL FACILITY
OF POOR QUALITY

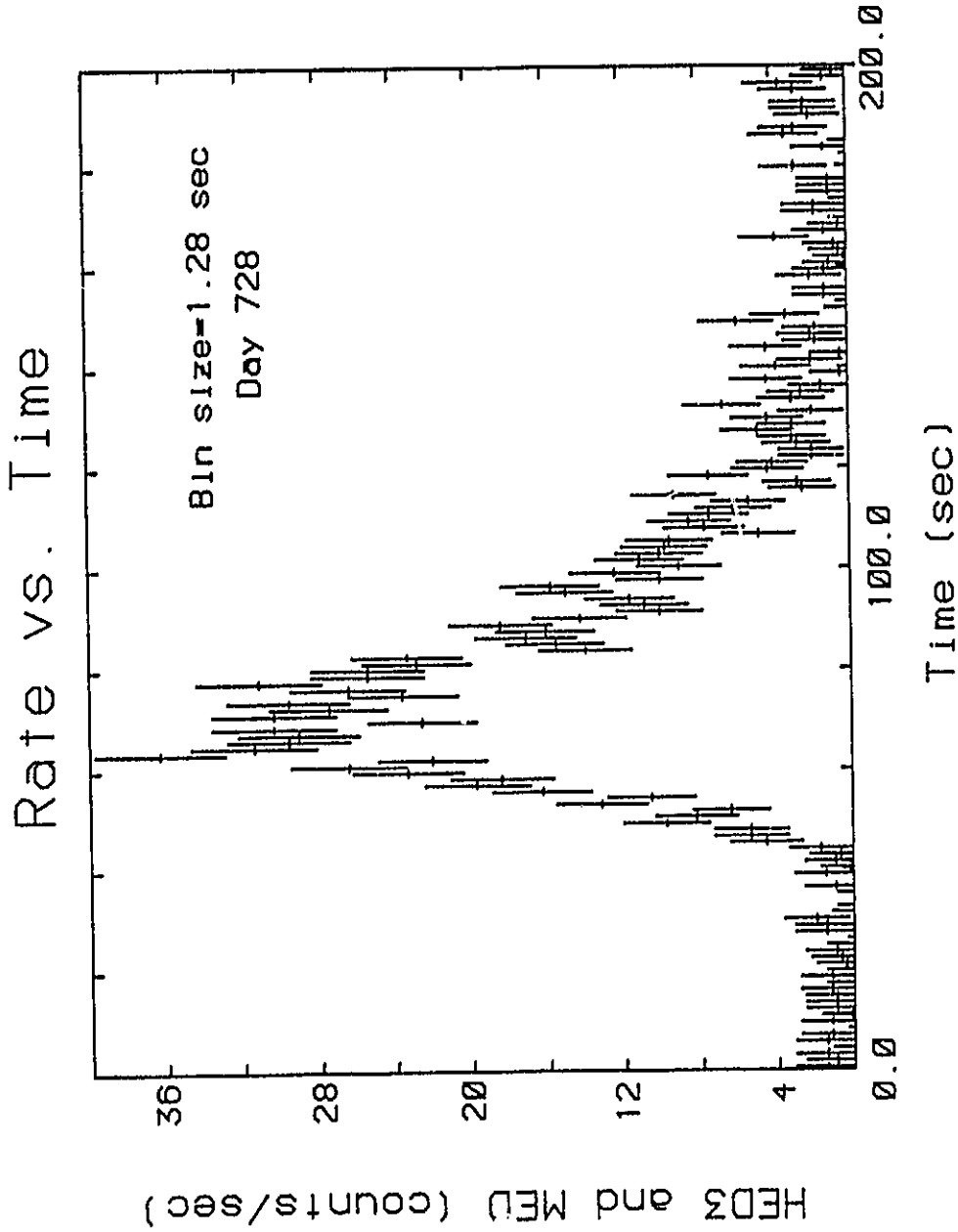


Figure C.3

ORIGINAL PAGE IS
OF POOR QUALITY

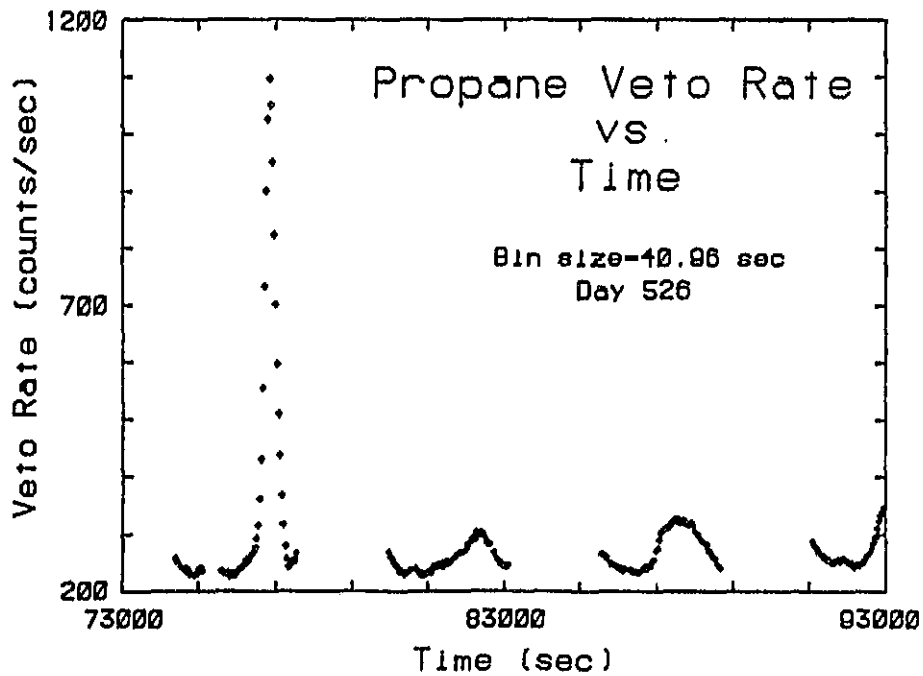
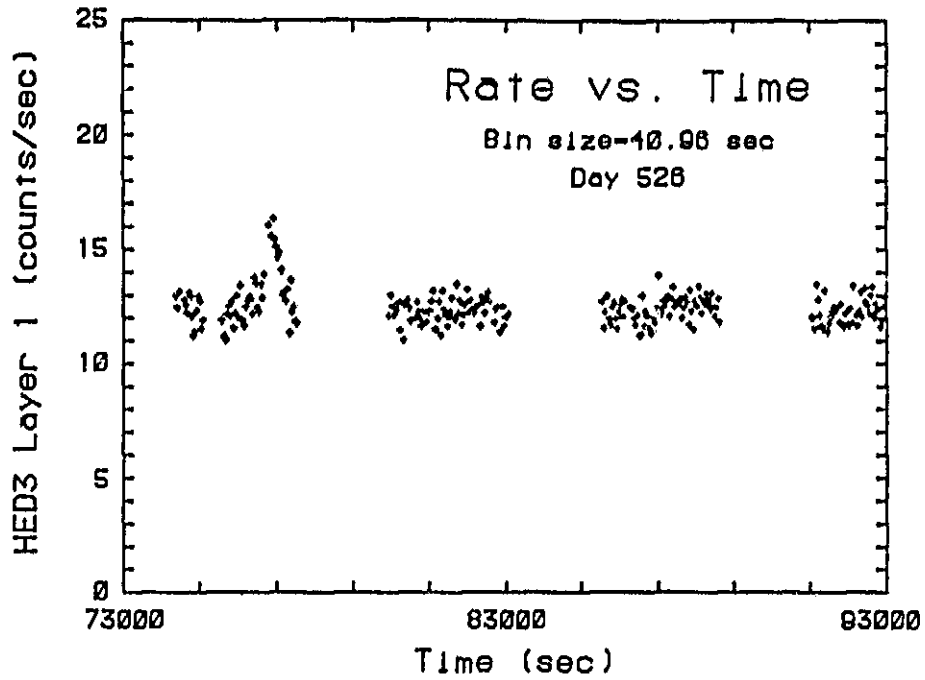


Figure C.4

ORIGINAL PAGE IS
OF POOR QUALITY

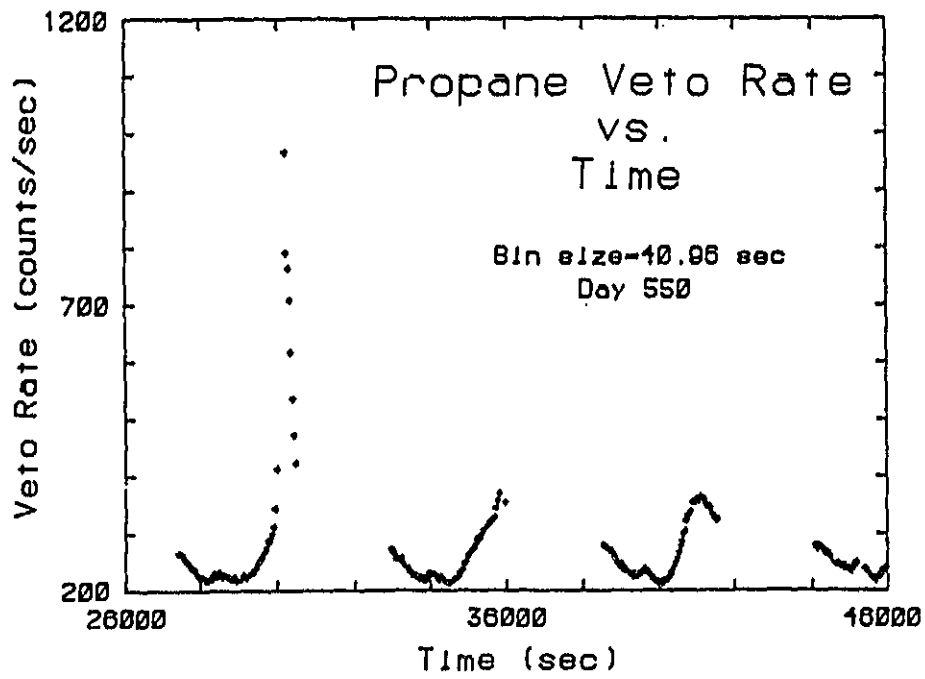
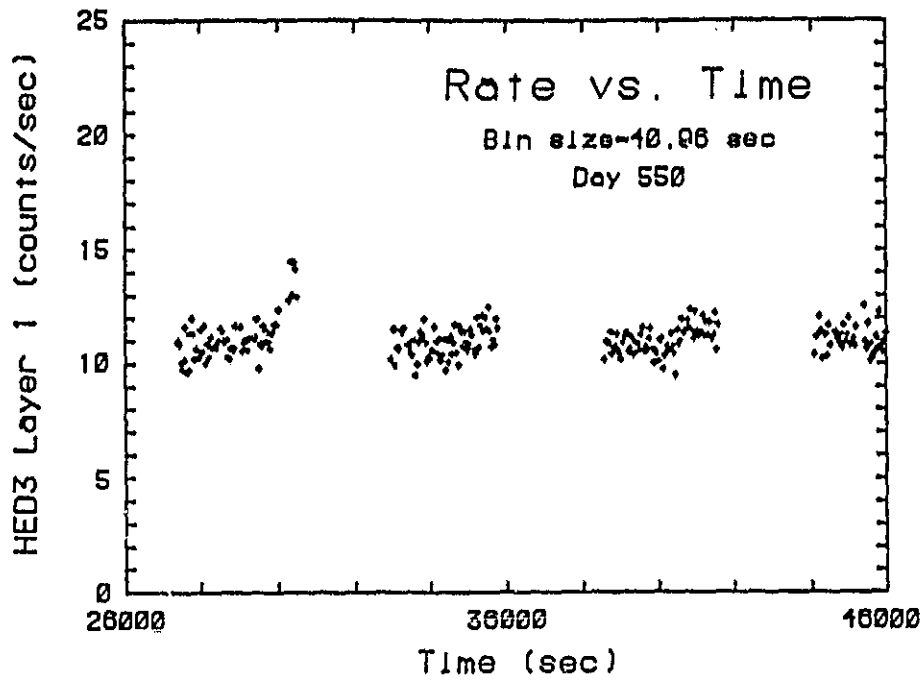


Figure C.5

APPENDIX D

Variable Soft X-ray Flux From the Pointed Observation at ESO 141-G55

In the top half of Figure D.1, I have plotted the argon detector count rate for photons with energy < 3 keV. Figure D.1 (bottom) is the corresponding plot for energies > 3 keV. It is important to realize that both plots contain data from exactly the same times and from the same detector. This data was from the same observation of ESO 141-G55 in which Mushotzky et al. (1980) reported a soft (< 3 keV) excess. Therefore taken at face value the figures indicate that this soft excess is showing variability on a time scale of only a few hours. From an astrophysical standpoint the luminosity from ESO 141-G55 is about 10 times greater than NGC 6814 and the inferred time scale is about 10 times longer.

The first impression that one obtains looking at Figure D.1 is that the variability is not due to any near-Earth effects since there is no strong orbital dependent signal in the data. There are several other reasons why it is unlikely that the soft excess is due to particles.

1. The particle flux and spectrum would have to be very unusual to give rise to counts in only the < 3 keV band.
2. Since the particles are not vetoed they must deposit most of their energy in the first layer. Figure D.2 shows the same soft enhancement in the second layer of the argon detector. Again one sees the variable signal in the low energy window, while the rate in the high energy window is roughly constant.
3. The xenon detector has a very weak response to events < 2.5 keV and so one cannot clearly see the time signature of the event. However, the total spectrum of the event is consistent with the xenon

detector seeing the same soft excess that the argon detector sees.

4. The xenon detector has a top layer propane veto that responds mostly to particles. The rates from this veto layer did not show the characteristic time signal seen in Figure D.1.

In summary, the signal that we see is consistent with both detectors responding to X-rays. Since the two detectors respond differently to particle events we conclude that it is impossible for particles to give rise to the observed signal.

However the variability is not from ESO 141-G55. During this observation the spacecraft spent some time pointing 6° away from the source. In Figure D.3 which has the same scale as Figure D.1, data is only included when the source is not in the detector's field of view. Again one should notice that only the < 3 keV rate is affected. The fact that the characteristic time signature is seen indicates that the soft X-rays are coming from an area extending over 6° on the sky. The fact that the rate varies indicates that the source must be close to the Earth. Thus the observation could be explained by some sort of high altitude air-glow.

In a quest for more data, I regenerated the data file without selecting on McIlwain L. The resulting light curve is displayed in Figure D.4. The high bins all show a clear orbital signature which one would expect if the effect is produced near the Earth. What is surprising is that the high rates occur when the source is coming out of Earth occultation but the rates are low going into Earth occult. Since ESO 141-G55 was in the morning sky, for the observation in April 1978, we find the detector was looking at the sunlit Earth going into Earth occultation. When the source came out of occultation not only was the detector looking at the dark Earth but the Sun was below the spacecraft's

horizon.

It is interesting that selecting data with low values of McIlwain L greatly decreased the soft excess. This is mostly due to chance. Both McIlwain L and the soft excess are related to the spacecraft's position about the Earth. Therefore, if the soft excess occurred at high values of L during one orbit, it would continue to appear at high L values during later orbits. The large peaks shown in Figure D.4 do not appear in the background. When Mushotzky et al. (1980) constructed the spectrum of ESO 141-G55 they did not select low values of McIlwain L. As a result, when they subtracted the off-source spectrum, the soft excess was still visible. When I reconstructed the on-source minus off-source spectrum using only data at low values of L, the soft excess was no longer seen. We conclude that there is no longer any evidence for a soft excess in the spectrum of ESO 141-G55.

An explanation that fits the data is that the soft X-rays are produced by a very high altitude air glow. Previous air glows that were detected with HEAO-1 were excited by solar UV radiation and so were strongest on the sunlit side of the Earth and rarely seen above 100 km. We routinely reject data if the lower 200 km of the Earth's atmosphere is anywhere in the detector's field of view. To my knowledge this is the first HEAO-1 observation of air glow that is both above 200 km and on the night side.

The only thing that I can think of that excites the upper atmosphere at night is trapped particles entering the atmosphere. Thus what we were observing was an aurora australis in the X-ray band. Since ESO 141-G55 is located rather far south in the sky, the spacecraft was looking in roughly the right direction in order to see an aurora. More importantly, the

geophysical magnetic indices show that the ESO 141-G55 observation occurred on the most disturbed day in April 1978. In fact the indices were only slightly higher in early May when there were extensive reports of auroral activity.

FIGURE CAPTIONS

Figure D.1 -- (top) The soft (< 3 keV) count rate in the argon detector is plotted vs. time during the observation of ESO 141-G55. An excess is seen with a peaking in the period 2 to 5 hours. For this and the remaining figures in this appendix, time 0 corresponds to 30,488 sec on day 466 (of 1977). (bottom) The corresponding hard flux for the argon detector. The excess is not visible but some variability, due to ESO 141-G55 not being area corrected, is seen.

Figure D.2 -- Same as figure D.1 except this time counts from the second layer of the detector are plotted. A weak excess is seen from 2 to 5 hours in the soft flux (top) but not in the hard (bottom).

Figure D.3 -- Same as figure D.1 except now data is plotted when ESO 141-G55 is not in the field of view. Again a flare is seen in the soft flux (top) but not the hard (bottom).

Figure D.4 -- Same as Figure D.1 except now data from all values of McIlwain L are included. One can now see an up to 6 ct/sec excess in the soft flux (top). The flares occurred when the detector came out of Earth occultation. Some of the noise seen in the hard flux (bottom) is due to the small increase in the background when McIlwain L is high.

ORIGINAL PAGE IS
OF POOR QUALITY

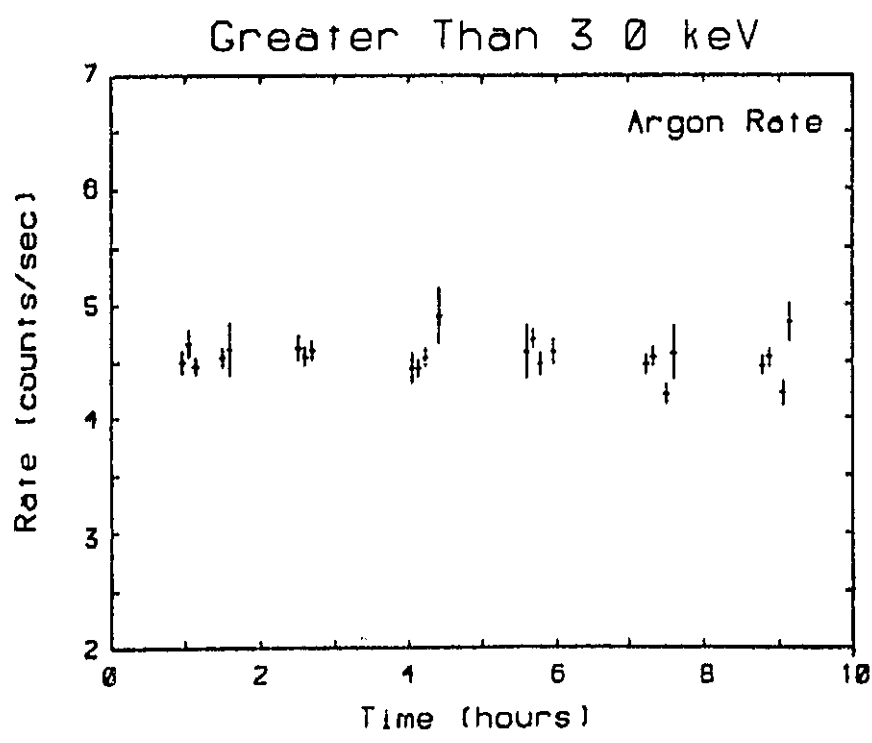
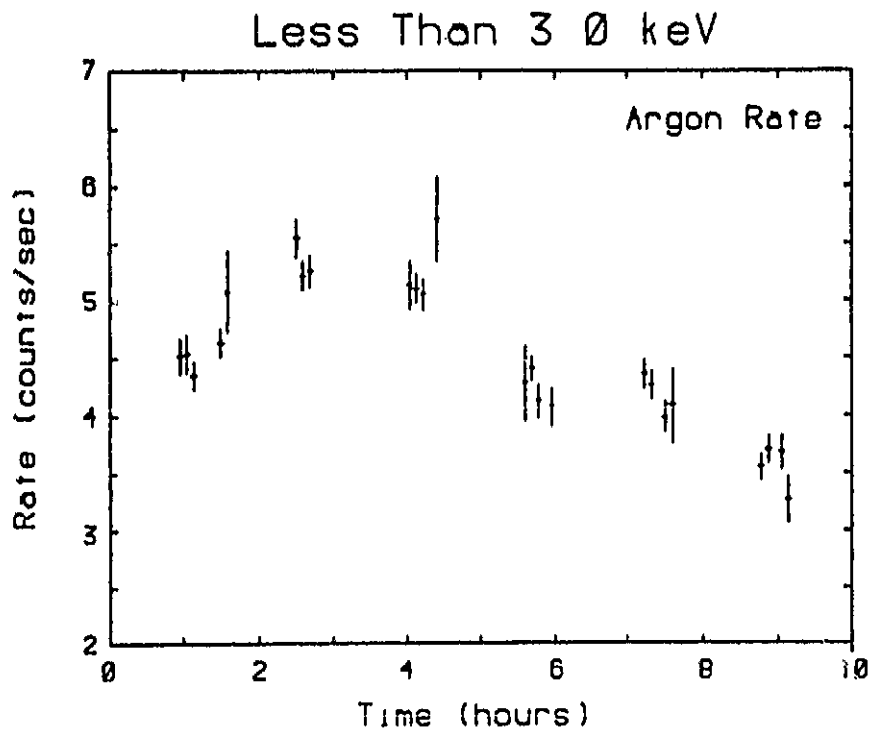


Figure D.1

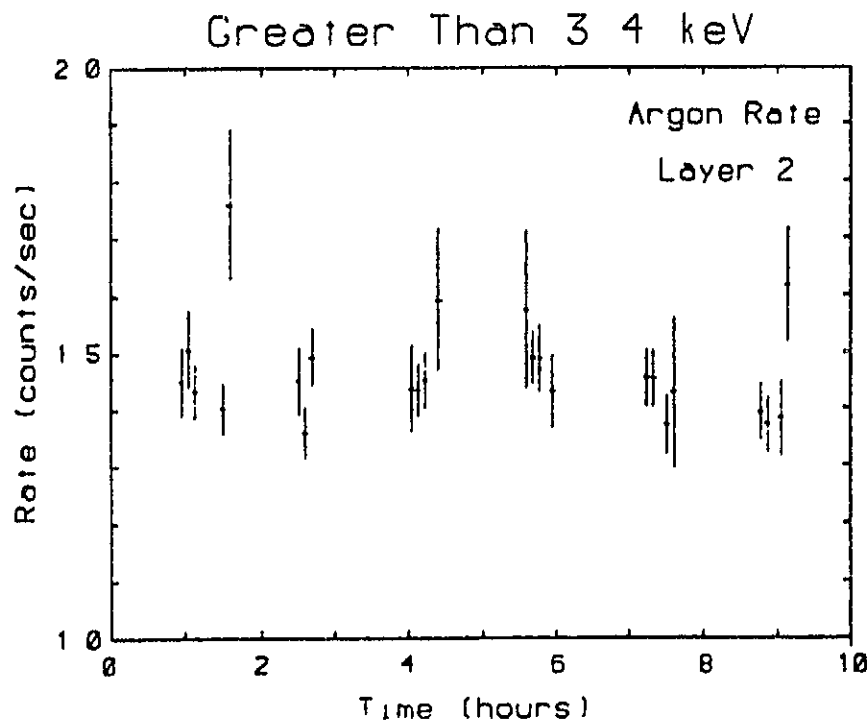
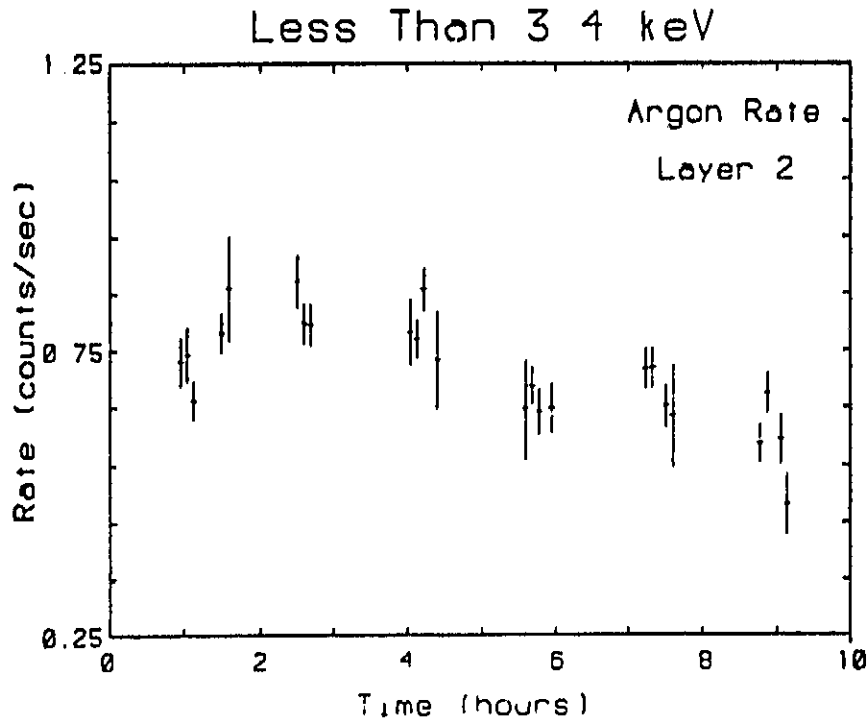


Figure D.2

ORIGINAL PAGE IS
OF POOR QUALITY

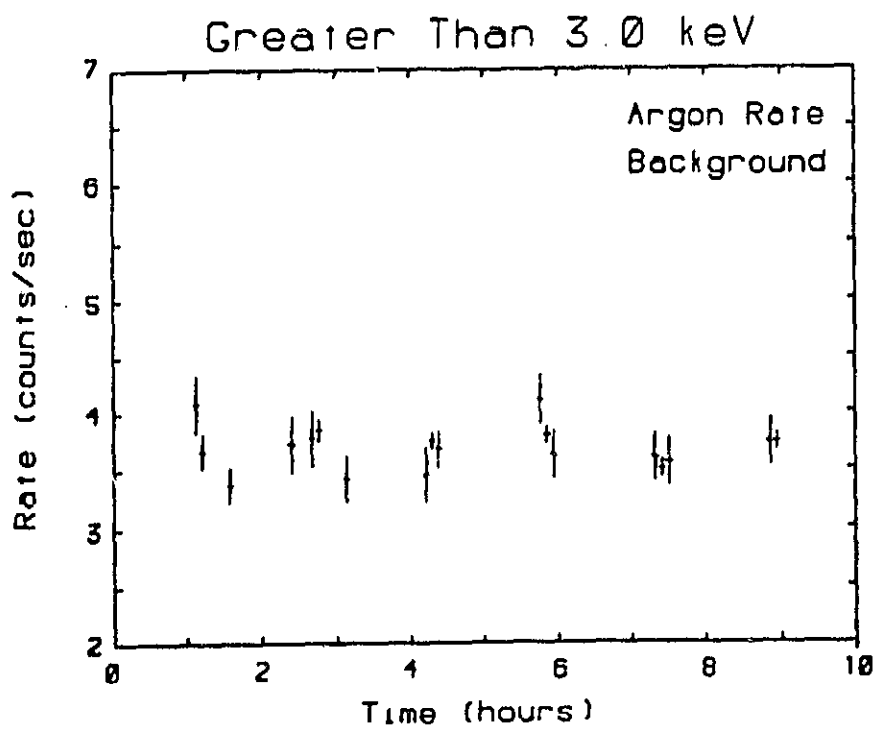
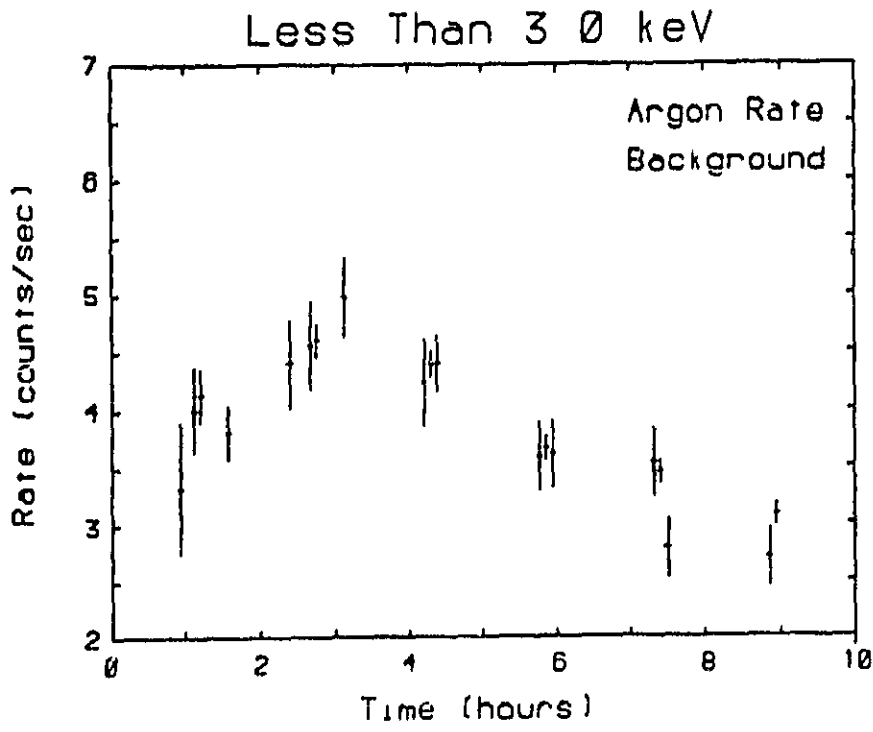


Figure D.3

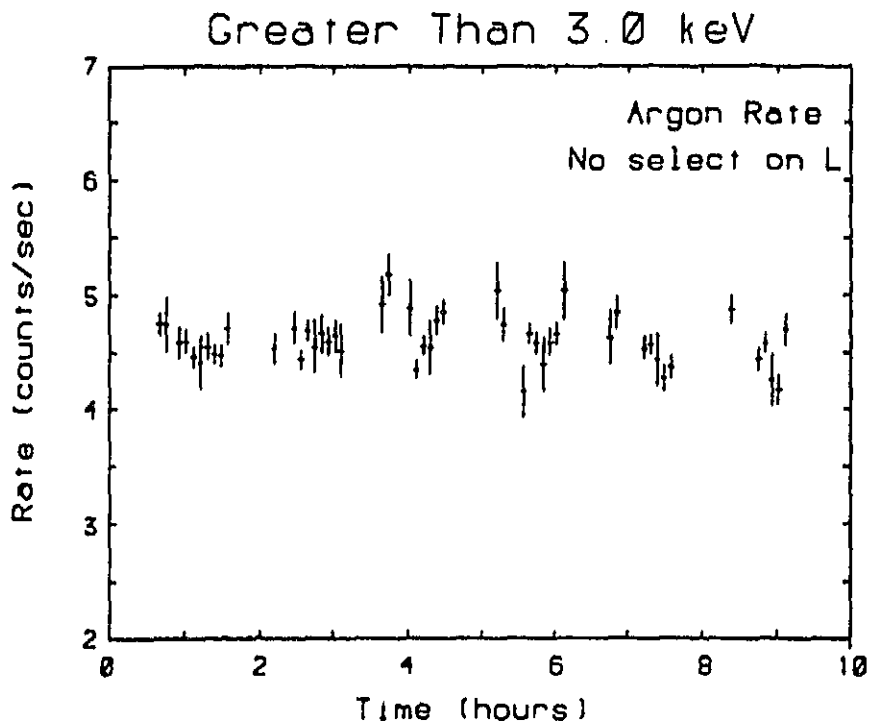
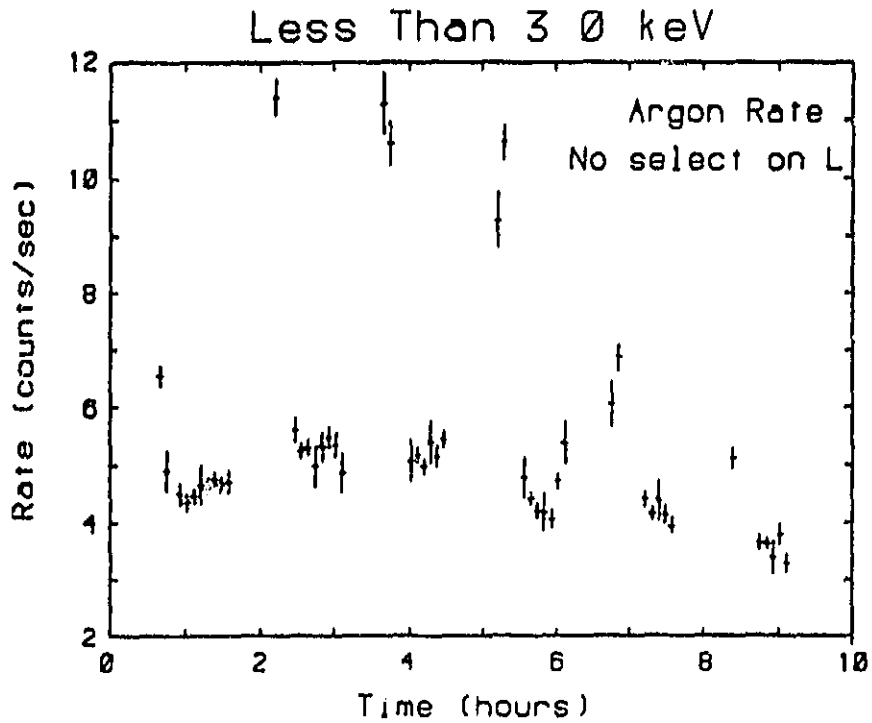


Figure D.4

APPENDIX E

The Future of Timing

The future of X-ray astrophysics requires detectors with larger area and reduced internal background. It is interesting that the next two major ($> 10^8$ \$) instruments optimize one or the other of the two basic requirements. The X-ray Timing Explorer (XTE) is designed to be an inexpensive ($\sim 10^8$ \$) large area experiment. To meet these requirements it is proposed that XTE be built with an $\sim 1 \text{ m}^2$ (10^4 cm^2) proportional counter array. On the other hand, AXAF (Advanced X-ray Astrophysics Facility) is designed to have very high resolution and thus a low background (per pixel). Due to the high cost of the telescope, the total collecting area is a more modest 2000 cm^2 . Although both instruments will be quite useful, I believe that the mythical ideal instrument would have properties somewhere between AXAF and XTE.

Consider an X-ray source with fluxes observed with a detector with collecting area A_c but a detector area of A_d and a background flux of b . If the source increases its flux by Δs then in time t the excess counts will be $\Delta s A_c t$. The total counts will be $s A_c t + b A_d t$ and so if one requires an $n\sigma$ detection then

$$\Delta s A_c t > n \sqrt{(s A_c + b A_d) t} \quad (\text{E.1})$$

Solving for t gives

$$t > \frac{n^2 (s + br)}{\Delta s^2 A_c} \quad (\text{E.2})$$

where $r = A_d/A_c$. For a proportional counter, $r = 1$, but for an imaging system A_d is the area of one pixel and r can be quite small. A simple form of Equation (E.2) was used by Gorenstein (1979).

For an imaging system with $r \ll 1$ the internal background, br , is effectively zero. Equation (E.2) reduces to

$$t_{im} > \frac{16s}{\Delta s^2 A_{im}} \quad (E.3)$$

where subscript im denotes the imaging case. Notice that larger areas are preferred. Since imaging experiments are more costly to build, they tend to have smaller collecting areas. The detector with the larger area will out perform a smaller detector, with no internal background, for all sources with $s > s_{min}$. It is easy to show that

$$s_{min} = br \frac{A_{im}}{A - A_{im}} \quad (E.4)$$

which is independent of Δs and n . Comparing XTE ($br \cong 5 \times 10^{-3}$) with AXAF, one finds that XTE is more sensitive to variability for all sources with flux $> 10^{-3}$ ct/cm²-sec or roughly 1×10^{-11} erg/cm²-sec which includes all sources considered in this thesis. Note: this has assumed sources with similar fluxes will give similar count rates for the two detectors. This is not entirely accurate since the two detectors have different band passes and spectral responses.

There is a practical minimum count rate due to the fact that an observatory needs to observe a large number of sources. In effect this means that typical observations should last a few hours. A good solid result requires a minimum number of photons, say 1000 (which can be divided

into 10 bins with a 10% statistical error per bin). For these numbers the minimum count rate is $\sim .1$ ct/sec. Note that a source flux of 10^{-3} ct/cm²-sec will give 10 ct/sec in the XTE detectors. This clearly shows that proportional counters are "background limited" for weak sources. It also shows that practical considerations only require that the background be reduced by a factor of 100. Further reductions in the background are needed only to study the very low flux sources. The small number of counts observed from these low flux sources will be almost useless for any serious work on variability or spectra.

In summary:

1. Improved timing results requires detectors with large area.
2. Low background is needed to study faint sources.
3. Instruments should be built and flown that fill the gap between XTE and AXAF. These instruments could be built along the lines of Goddard's Broad Band X-Ray Telescope (BBXRT) or the Harvard/SAO Large Area Modular Array of Reflectors (LAMAR).

APPENDIX F

The 730 Sec Flare From NGC 4151

Tananbaum et al. (1978) observed "significant flaring from NGC 4151 with as much as a factor of 10 increase (in X-ray flux) in a time as short as 730 sec." To date this observation has remained unconfirmed. In this section I reconsider the evidence for flaring and show that a smaller, slower change in source flux can account for the data.

The observation was made with Uhuru which did not point at the source but rather scanned over it. For every pass across NGC 4151, Tananbaum et al. included the central 1.73 sec of data "in an attempt to maximize the signal from the source while minimizing the background counts". Although it is quite likely that different scans resulted in slightly different exposures, the authors give no indication as to how different. In addition, by effectively ignoring all data between the scans, they have ignored any changes in the detector background which will greatly affect their calculated probability.

If we assume these effects are small then we can reproduce their numbers. For their Figure 1, they plotted 47 data bins with a mean rate of 19.3 ct per bin of which ~ 15.7 are background. One scan had a rate of 37 ct. Using Poisson statistics, the probability of getting 37 or more counts for a mean of 19.3 is $P_p(>37; \mu=19.3) = 2.1 \times 10^{-4}$ which agrees with 2×10^{-4} which they reported. However their 47 observations were made over a 24 hour period and we now know that the flux from NGC 4151 can double in as little as 12 hours (Mushotzky et al. 1978, Lawrence 1980). Therefore, the mean for the entire observation might not be an accurate estimate for the flux when the flare occurred.

Weisskopf and Sutherland (1978) pointed out calculations, such as made above, are very sensitive to the estimate of the mean. To see this assume that the flux from NGC 4151 had doubled. The true mean is now estimated to be 22.9 which corresponds to ~ 20% increase in the total rate. Again using Poisson statistics $P_p(>37; \mu=22.9) = 3.7 \times 10^{-3}$. Thus a 20% change in the mean, increases the probability that the flare was due to chance by a factor of 18. In addition, 3.7×10^{-3} is the probability that one bin is high. If we include the fact that 47 bins were examined the probability of seeing such a deviation drops to 6%. Finally, we ask whether a high mean is inconsistent with the downward fluctuations. The rate 730 sec before the flare was 16. The probabilities are given by

$$P_p(<16; \mu=19.3) = .27$$

$$P_p(<16; \mu=22.9) = .084$$

So although the probability of getting such a downward excursion has dropped by a factor of 3, such an excursion is expected for 1 bin in 12 by Poisson statistics alone.

In summary, reexamination of the Uhuru observation of NGC 4151 shows:

- 1) The observation is consistent with variability on a time scale of less than 1 day.
- 2) Slow changes in the mean can greatly increase the probability of seeing "flares".
- 3) Small changes in the background (or even the source exposure) would also increase the chances of seeing "flares".
- 4) In light of the above there is no strong evidence for 700 sec flares.

REFERENCES

- Bailey, T.A., Smith, A., and Turnes, M.J.L., 1978, Nucl. Instrum. Meth., 155, 177.
- Baity, W.A., Mushotzky, R.F., Worrall, D.M., Rothschild, R.E., Tennant, A.F., and Primini, F.A., 1983, submitted to Ap. J.
- Baity, W.A., et al., 1981, Ap. J., 244, 429.
- Barr, P., White, N.E., Sanford, P.W., and Ives, J.C., 1977, M.N.R.A.S., 181, 43p.
- Bevington, P.R., 1969, Data Reduction and Error Analysis for the Physical Sciences (New York: McGraw-Hill Book Company).
- Boldt, E.A., Holt, S.S., Rothschild, R., and Serlemitsos, P., 1975, Proc. Internat. Conf. on X-Rays in Space, 1, 69.
- Box, G.E.P., and Jenkins, G.M., 1976, Time Series Analysis: Forecasting and Control (San Francisco: Holden-Day).
- Cavaliere, A., and Morrison, P., 1980, Ap. J. (Letters), 238, L63.
- Cavallo, G., and Rees, M.J., 1978, M.N.R.A.S., 183, 359.
- Coe, M.J., Bowring, S.R., Hall, C.J., and Stephen, J.B., 1983, Astrophys. Let., 23, 17.
- Cooper, B.F.C., Price, R.M., and Cole, D.J., 1965, Austr. J. of Phys., 18, 589.
- Cowie, L.L., Ostriker, J.P., and Stark, A.A., 1978, Ap. J., 226, 1041.
- Delvaille, J.P., Epstein, A., and Schnopper, H.W., 1978, Ap. J. (Letters), 219, L81.
- Dower, R.G., Griffiths, R.E., Bradt, H.V., Doxsey, R.E., and Johnson, M.D., 1980, Ap. J., 235, 355.
- Efanov, V.A., Moiseev, I.G., Nesterov, N.S., and Shakhovskoy, N.M., 1977,

- Nature, 269, 493.
- Elvis, M., 1976, M.N.R.A.S., 177, 7p.
- Fabian, A.C., and Rees, M.J., 1979, in Proc. IAC/Cospar Symposium on X-ray Astronomy, ed. W.A. Baity and L.E. Peterson (London: Pergamon Press), p. 381.
- Glass, I.S., 1979, M.N.R.A.S., 186, 29p.
- Gorenstein, P., 1979, in Compact Galactic X-ray Sources, ed. by F. Lamb and D. Pines, Univ. of Illinois at Urbana-Champaign, p. 279.
- Gorenstein, P., and Mickiewicz, S., 1968, Rev. Sci. Instrum., 39, 816.
- Greenstein, J.L., and Matthews, T.A., 1963, Nature, 197, 1041.
- Guilbert, P.W., Ross, R.R., and Fabian, A.C., 1982, M.N.R.A.S., 199, 763.
- Halpern, J.P., 1982, Ph.D. Thesis, Harvard.
- Jenkins, G.M., and Watts, D.C., 1968, Spectral Analysis and Its Applications (San Francisco: Holden-Day).
- Jones, T.W., Leung, C.M., Gould, R.J., and Stein, W.A., 1977, Ap. J., 212, 52.
- Khachikian, E. Ye., and Weedman, D.W., 1971, Astrofizika, 7, 389.
- Khachikian, E. Ye., and Weedman, D.W., 1974, Ap. J., 192, 581.
- Kikuchi, S., Tabara, H., Mikami, Y., Kawano, N., Kawajira, N., Ojima, T., Tomino, K., Daishido, T., and Kono, M., 1973, Publ. Astron. Soc. Jap., 25, 555.
- Krolik, J.K., and London, R.A., 1983, Ap. J., 267, 18.
- Lawrence, A., 1980, M.N.R.A.S., 192, 83.
- Lawrence, A., and Elvis, M.S., 1982, Ap. J., 256, 410.
- Lawrence, A., Giles, A.B., McHardy, I.M., and Cooke, B.A., 1981, M.N.R.A.S., 195, 149.
- Lawrence, A., Pye, P.J., and Elvis, M., 1977, M.N.R.A.S., 181, 93p.

- Leifer, D., 1980, Astr. Ap., 89, 370.
- Lightman, A.P., 1982, Ap. J., 253, 842.
- Lightman, A.P., Giacconi, R., and Tananbaum, H., 1978, Ap. J., 224, 375.
- Lightman, A.P., and Rybicki, G.B., 1979, Ap. J., 232, 882.
- Lynden-Bell, D., 1969, Nature, 223, 690.
- Lyutyi, V.M., 1977, Astr. Zh., 54, 1153.
- Malkan, M.A., and Sargent, W.L.W., 1982, Ap. J., 254, 22.
- Marshall, F.E., Boldt, E.A., Holt, S.S., Mushotzky, R.F., Pravdo, S.H.,
Rothschild, R.E., and Serlemitsos, P.J., 1979, Ap. J. Suppl, 40,
657.
- Marshall, F.E., Holt, S.S., Mushotzky, R.F., and Becker, R.H., 1983, Ap. J.
(Letters), 269, L31.
- Marshall, F.J., and Clark, G.W., 1981, Ap. J., 245, 840.
- Marshall, N., Warwick, R.S., and Pounds, K.A., 1981, M.N.R.A.S., 194, 987.
- Mason, I.M., and Culhane, J.L., 1983, IEEE Tran. Nuc. Sci., 30, 485.
- Matilsky, T., Shrader, C., and Tananbaum, H., 1982, Ap. J. (Letters), 258,
L1.
- McIlwain, C.E., 1961, J. Geophys. Res., 66, 3681.
- Mushotzky, R.F., 1983, to appear in 11th Texas Symposium on Relativistic
Astrophysics.
- Mushotzky, R.F., Holt, S.S., and Serlemitsos, P.J., 1978, Ap. J. (Letters),
225, L115.
- Mushotzky, R.F., Marshall, F.E., Boldt, E.A., Holt, S.S., and Serlemitsos,
P.J., 1980, Ap. J., 235, 361.
- Oort, J.H., 1977, Ann. Rev. Astron. Astrophys., 15, 295.
- Osterbrock, D.E., 1978, Physica Scripta, 17, 285.

- Osterbrock, D.E., 1981, in Active Galactic Nuclei, ed. C. Hazard and S. Mitton (Cambridge: Cambridge), pp 25-50.
- Pounds, K.A., 1979, Proc. Roy. Soc. London, A, 366, 375.
- Rees, M.I., Begelman, M.C., and Blandford, R.D., 1981, in 10th Texas Symposium on Relativistic Astrophysics, ed. R. Ramaty and F.E. Jones (New York: New York Academy of Sciences), p. 254.
- Rieke, G.H., 1978, Ap. J., 226, 550.
- Rothschild, R., et al., 1979, Space Sci. Instrumentation, 4, 265.
- Sanders, R.H., 1981, Nature, 294, 427.
- Scargle, J.D., 1981, Ap. J. Supp. Series, 45, 1.
- Schmidt, M., 1963, Nature, 197, 1040.
- Shapiro, S.L., Lightman, A.P., and Eardley, D.M., 1976, Ap. J., 204, 187.
- Smart, D.F., and Sheo, M.A., 1967, J.G.R., 72, 3447.
- Stein, W.A., and Weedman, D.W., 1976, Ap. J., 205, 44.
- Tananbaum, H., 1980, in X-Ray Astronomy, ed. R. Giacconi and G. Setti (Dordrecht: Reidel).
- Tananbaum, H., et al., 1979, Ap. J. (Letters), 234, L9.
- Tananbaum, H., Peters, G., Forman, W., Giacconi, R., Jones, C., and Avni, Y., 1978, Ap. J., 223, 74.
- Tennant, A.F., Mushotzky, R.F., Boldt, E.A., and Swank, J.H., 1981, Ap. J., 251, 15.
- Tennant, A.F., and Mushotzky, R.F., 1983, Ap. J., 264, 92.
- Tennant, A.F., and Swank, J.H., 1983, in preparation.
- Thorne, K.S., 1974, Ap. J., 191, 507.
- Van Bueren, H.G., 1978, Astron. Astrophys., 70, 707.
- Weedman, D.A., 1977, in Ann. Rev. of Astron. Astrophys, pp 69-95.

Weisskopf, M.C., Kahn, S.M., and Sutherland, P.G., 1975, Ap. J. (Letters), 199, L147.

Weisskopf, M.C., and Sutherland, P.G., 1978, Ap. J., 221, 228.

Wilson, A.S., Pooley, G.G., Willis, A.G., and Clements, E.D., 1980, Ap. J. (Letters), 237, L61.

Wilson, A.S., and Willis, A.G., 1980, Ap. J., 240, 429.

Winkler, P.E., and White, A.E., 1975, Ap. J. (Letters), 199, L139.

Wolstencroft, R.D., Gilmore, G., and Williams, P.J., 1982, M.N.R.A.S., 201, 479.

Yee, H.K.C., 1980, Ap. J., 241, 894.